

**STUDY OF THE AUSTENITE DECOMPOSITION AND FORMATION OF
PROEUTECTOID CEMENTITE IN HYPER-EUTECTOID STEELS**

by

Raymundo Ordóñez Olivares

B.Sc. in Metallurgy, Instituto Politécnico Nacional, 1997

Master of Science in Materials Science, Instituto Politécnico Nacional, 2000

Submitted to the Graduate Faculty of
the Swanson School of Engineering in partial fulfillment
of the requirements for the degree of
Doctor of Philosophy in Materials Science and Engineering

University of Pittsburgh

2011

UNIVERSITY OF PITTSBURGH
SWANSON SCHOOL OF ENGINEERING

This dissertation was presented

by

Raymundo Ordóñez Olivares

It was defended on

August 11, 2011

and approved by

Calixto I. Garcia, Ph.D., Research Professor, Department of Mechanical Engineering and
Materials Science

Luis E. Vallejo, Ph.D., Professor, Department of Civil and Environmental Engineering

Scott X. Mao, Ph.D., William Kepler Whiteford Professor, Department of Mechanical
Engineering and Materials Science

Dissertation Director: Anthony J. DeArdo, Ph.D., William Kepler Whiteford Professor,
Department of Mechanical Engineering and Materials Science

Copyright © by Raymundo Ordóñez Olivares

2011

**STUDY OF THE AUSTENITE DECOMPOSITION AND FORMATION OF PROEUTECTOID
CEMENTITE IN HYPEREUTECTOID STEELS**

Raymundo Ordóñez Olivares, Ph.D.

University of Pittsburgh, 2011

Eutectoid and hypereutectoid steels are extensively used for different engineering applications, because they offer a useful combination of strength and ductility as well as good corrosion resistance, wear resistance and machinability. In these steels, the major microstructural microconstituent is pearlite. However, depending on the chemical composition of the austenite prior to transformation and the thermal path during the decomposition of austenite, i.e., rate of cooling to the transformation temperature, the formation of proeutectoid cementite along the prior-austenite grain boundaries might take place. The presence of proeutectoid cementite along the austenite grain boundaries has a deleterious effect on the final mechanical properties of these fully pearlitic steels. Thermomechanical processing studies on hypereutectoid steels have shown that the composition and microstructural conditions of austenite prior to transformation to a fully pearlitic microstructure has a strong effect on reducing the formation of proeutectoid cementite along the austenite grain boundaries as well as the refinement of the interlamellar spacing. A study of the effect of different microstructural features and precipitation behavior on the mechanical properties and wear behavior is presented.

TABLE OF CONTENTS

ACKNOWLEDGMENTS	XVIII
1.0 INTRODUCTION.....	1
2.0 BACKGROUND	4
2.1 RAIL STEELS	4
2.2 PEARLITE MICROSTRUCTURE	7
2.3 PEARLITE NUCLEATION.....	10
2.4 PEARLITE GROWTH	13
2.4.1 Effect of Alloying Elements on Pearlite Growth.....	16
2.5 KINETICS OF PEARLITE FORMATION.....	18
2.5.1 Effect of Alloying Elements on the Eutectoid Composition and Temperature.....	19
2.5.2 Interlamellar Spacing.....	21
2.6 CEMENTITE	22
2.6.1 Proeutectoid Cementite.....	24
2.6.2 Orientation Relationship between Austenite and Cementite	27
2.7 THE EFFECT OF PRIOR AUSTENITE GRAIN SIZE ON THE SIZE OF THE PEARLITE NODULES.....	29

2.8	ROLE OF MICROSTRUCTURE ON THE MECHANICAL PROPERTIES	30
	
2.9	WEAR - MICROSTRUCTURE AND MECHANICAL PROPERTIES	
	RELATIONSHIP	37
2.10	DEFORMATION OF PEARLITE.....	38
3.0	STATEMENT OF OBJECTIVES.....	40
4.0	EXPERIMENTAL PROCEDURE.....	41
4.1	ALLOY DESIGN	42
4.2	MATERIAL PROCESSING	44
4.3	OPTICAL MICROSCOPY.....	46
4.4	ELECTRON MICROSCOPY TECHNIQUES.....	47
4.5	MECHANICAL TESTING.....	48
4.6	WEAR TEST.....	49
4.7	ISOTHERMAL TRANSFORMATION STUDIES	52
5.0	RESULTS	53
5.1	MICROSTRUCTURAL ASSESSMENT OF COMMERCIAL RAIL STEELS.	53
5.1.1	Yield strength and its relationship with microstructural features.....	58
	5.1.1.1 Yield Strength vs Interlamellar Spacing.....	58
	5.1.1.2 Yield Strength vs Pearlite Colony and Prior Austenite Grain Size..	59
5.1.2	Non-Metallic Inclusions	61
5.1.3	Proeutectoid Cementite.....	63
5.2	THERMOMECHANICAL EXPERIMENTS.....	65
5.2.1	Rsteel1.....	66

5.2.2	Rsteel2.....	70
5.2.3	Rsteel3.....	74
5.3	MECHANICAL PROPERTIES.....	80
5.3.1	Hardness Testing	80
5.3.2	Tensile Testing	82
5.3.3	Fracture Toughness.....	85
5.4	WEAR TESTING	86
5.5	ISOTHERMAL TRANSFORMATION STUDIES.....	92
6.0	DISCUSSION	101
6.1	MICROSTRUCTURAL ASSESSMENT	101
6.2	THERMOMECHANICAL EXPERIMENTS.....	108
6.2.1	Rsteel1.....	109
6.2.2	Rsteel2.....	113
6.2.3	Rsteel3.....	117
6.3	MECHANICAL PROPERTIES.....	119
6.3.1	Hardness	119
6.3.2	Tensile Testing	120
6.3.3	Fracture Toughness.....	123
6.4	WEAR TESTING	124
6.5	ISOTHERMAL TRANSFORMATION STUDIES.....	128
7.0	CONCLUSIONS	130
	APPENDIX A	131
	APPENDIX B	139

BIBLIOGRAPHY..... 143

LIST OF TABLES

Table 4.1 Chemical composition in weight % and (atomic %)	43
Table 5.1 Values of interlamellar spacing, pearlite colony size and prior austenite grain size from the commercial steels	57
Table 5.2 Summary of the values of volume fraction of non-metallic inclusions and the measured proeutectoid cementite in commercial steels.....	63
Table 5.3 Prior austenite grain size and reheating temperatures used in each steel	65
Table 5.4 Thermomechanical processing details, hardness and microstructures generated.....	68
Table 5.5 Thermomechanical processing details, hardness and microstructure generated	72
Table 5.6 Thermomechanical processing details, hardness and microstructure generated for Rsteel3	76
Table 5.7 Hardness values and interlamellar spacing of the developed steels	81
Table 5.8 Tensile test values of rail steels developed by this research.....	83
Table 5.9 K_Q / K_{IC} test results.....	85
Table 5.10 Average of the depth and width values of wear test of each steel	87

LIST OF FIGURES

Figure 2.1 Pin-ring wear rate versus hardness data for pearlitic and bainitic steels.....	6
Figure 2.2 Schematic representation of different microstructural components of a fully pearlitic steel	7
Figure 2.3 Typical pearlitic microstructure	8
Figure 2.4 Partial of iron – iron carbide phase diagram	9
Figure 2.5 Micrograph of a pearlite nodule advancing into the austenite grain	10
Figure 2.6 Nucleation and growth of pearlite	11
Figure 2.7 Degenerated pearlite microstructure.....	12
Figure 2.8 Schematic branching mechanism for the growth of pearlite	13
Figure 2.9 A pearlite growth model.....	15
Figure 2.10 Comparison of growth rate curves of pearlite in nickel and manganese steels as a function of temperature.....	16
Figure 2.11 a) Variation of nucleation rate and growth rate of pearlite with temperature, b) Isothermal transformation curve for plain carbon steels	18
Figure 2.12 Effect of alloying elements on g phase field: a) Titanium, b) Chromium.....	20
Figure 2.13 Effect of alloying elements on a) Eutectoid reaction temperature and b) Eutectoid carbon content.....	21
Figure 2.14 Hardness test measurements for Fe-C alloys.....	23

Figure 2.15 Tensile elongation data as a function of volume fraction of cementite.....	24
Figure 2.16 Optical micrograph showing proeutectoid cementite network on prior austenite grain boundaries	25
Figure 2.17 SEM micrographs of deep etched samples. a) Proeutectoid cementite grain film with dendritic feature. b) Fernlike cementite precipitated covering grain boundaries	26
Figure 2.18 Schematic representation of austenite grains	28
Figure 2.19 Effect of prior-austenite grain size on the nodule size for hyper-eutectoid steels.....	30
Figure 2.20 Yield strength as a function of the pearlite interlamellar spacing for eutectoid and hypoeutectoid steels	32
Figure 2.21 Pearlite interlamellar spacing versus austenitizing temperature for UHCS	34
Figure 2.22 Interrelation between the strength and interlamellar spacing.....	35
Figure 2.23 Hardness as a function of pearlite interlamellar spacing for various rail steels	35
Figure 2.24 a) Dependency of prior austenite grain size on the transition temperature b) Charpy transition curves as a function of prior austenite grain size.....	36
Figure 2.25 a) Wear resistance as a function of hardness for various rail steels tested at contact pressures of 1220 N/mm ² and 700 N/mm ² , b) Wear rate as a function of pearlite interlamellar spacing for various rail steels tested at contact pressure of 1220 N/mm ² and 900N/mm ²	38
Figure 2.26 Shear cracking of pearlite, a) Cracking of cementite plate; b) Shear zone developing in the ferrite causing cracking of neighboring plates, c) Void formation and d) void coalescence	39
Figure 4.1 Rail profile, indicating sampling locations.....	41
Figure 4.2 Schematic of a standard compression specimen	45

Figure 4.3 Schematic representations of the thermomechanical experiments	46
Figure 4.4 Wear test machine	50
Figure 4.5 a) Sampling from the rolled material b) Configuration and dimensions of disk and pin c) Schematic representation of wear testing	50
Figure 4.6 Schematic representations of isothermal transformation studies	52
Figure 5.1 SEM micrographs showing the interlamellar spacing of some of the commercial steels a) Steel A, b) Steel B), c) Steel K, d) Steel L, e) Steel D, and e) Steel I	54
Figure 5.2 SEM micrographs showing the pearlite colony of some of the commercial steels a) Steel E, b) Steel D), c) Steel K, d) Steel M, e) Steel A, and e) Steel B	55
Figure 5.3 Optical micrographs showing the austenite grain boundaries of some of the commercial steels. a) Steel A, b) Steel D), c) Steel E, d) Steel B, e) Steel M, and e) Steel C.....	56
Figure 5.4 Yield strength variations with respect to interlamellar spacing from different commercial steels.....	58
Figure 5.5 Pearlite colony size vs yield strength calculated from equation 5.1.....	60
Figure 5.6 Relationship between the prior austenite grain size and the yield strength of commercial steels.....	60
Figure 5.7 Optical micrographs of non-metallic inclusions of commercial steels a) Steel F, c) Steel E, and e) Steel A, SEM micrograph from the same area b) Steel F) , d)Steel E and e)Steel A.....	62
Figure 5.8 Scanning electron micrographs of some commercial steels. Arrows show the presence of the proeutectoid phase a) Steel D and b) Steel M.....	64

Figure 5.9 TTT diagram calculated by the JMatPro 4.0 program from the chemical composition on the Rsteel 1.....	67
Figure 5.10 Results of hardness and microstructure of rail steel 1.....	68
Figure 5.11 Scanning electron micrograph of Rsteel1 developed throughout the thermomechanical experiment number 8. Fully pearlitic microstructure is shown.....	69
Figure 5.12 TTT diagram calculated on JMatPro program from Rsteel2 chemical composition	70
Figure 5.13 Results of hardness and microstructure of Rsteel2.....	72
Figure 5.14 Scanning electron micrograph of Rsteel2 developed throughout the thermomechanical experiment number 3.....	73
Figure 5.15 TTT diagram calculated by the JMatPro program from the chemical composition of the Rsteel3.....	74
Figure 5.16 Results of hardness and microstructure of Rsteel3.....	77
Figure 5.17 Scanning electron micrograph of Rsteel3 developed throughout the thermomechanical experiment number 9.....	78
Figure 5.18 Hardness and interlamellar spacing values of thermomechanical experiments	79
Figure 5.19 Hardness dependence on interlamellar spacing.....	79
Figure 5.20 Relationship of hardness and interlamellar spacing of developed steels	81
Figure 5.21 Stress vs Strain curves of the developed steels (Rsteel1, Rsteel2 and Rsteel3).....	83
Figure 5.22 Comparison of yield strength between developed steels vs yield strength of some commercial steels.....	84
Figure 5.23 Comparison of elongation between developed steels vs elongation of commercial steels.....	84

Figure 5.24 Schematic representations of the locations where the groove height and depth were measured	86
Figure 5.25 a) Micrographs of the surface of the wear test disk before performing the test. b) Three dimensional representation of the surface of the wear test disk before performing the test	88
Figure 5.26 a) Micrograph from the top of the disk, showing a groove generated during wear testing after 10000 cycles in Rsteel1, b) Three dimensional representation of the groove generated.....	88
Figure 5.27 a) Micrograph from the top of the disk, showing a groove generated during wear testing after 10000 cycles in Rsteel2, b) Three dimensional representation of the groove generated.....	89
Figure 5.28 a) Micrograph from the top of the disk, showing a groove generated during wear testing after 10000 cycles in Rsteel3, b) Three dimensional representation of the groove generated.....	89
Figure 5.29 Schematic representation of the material relocation process during wear testing.....	90
Figure 5.30 a) Depth of generated groove with respect to the number of cycles of the developed steels b) Depth of generated groove with respect to the log number of cycles of the developed steels	91
Figure 5.31 Wear measurements in terms of area displaced of the developed steels.....	92
Figure 5.32 Fraction of pearlite transformed as a function of time for different temperatures of commercial steel D	93
Figure 5.33 Fraction of pearlite transformed as a function of time for different temperatures of Rsteel2.....	94

Figure 5.34 Temperature transformation time diagram (TTT) of commercial steel D	95
Figure 5.35 TTT diagram of commercial steel D and the micrographs at different times and temperatures	96
Figure 5.36 Temperature transformation time diagram (TTT) of developed steel Rsteel2.....	98
Figure 5.37 TTT diagram of Rsteel2 and the micrographs at different times and temperatures..	99
Figure 5.38 Prior austenite grain boundary of Rsteel 2 without proeutectoid cementite	100
Figure 6.1 Typical appearance of the pearlite (P) and proeutectoid cementite (PC).....	101
Figure 6.2 Relationship between 0.2% offset yield strength and interlamellar spacing of pearlite in eutectoid carbon steels	102
Figure 6.3 Interlamellar spacing of different commercial steels	102
Figure 6.4 Effect of sulfide volume fraction on longitudinal and transverse total ductility at fracture	104
Figure 6.5 Rolling contact fatigue No. cycles versus volume fraction of oxides	106
Figure 6.6 Relationship between the 80% resource of rail and oxygen content in rail steels	106
Figure 6.7 Relation between contact fatigue limit and prior austenite grain size.....	107
Figure 6.8 Relationship between wear versus wear factor	108
Figure 6.9 Coarse pearlite generated through TMP5.....	110
Figure 6.10 Bright field TEM micrographs from TMP 7 of Rsteel1	111
Figure 6.11 Chemical analysis spectrum from one precipitate observed in the sample of TMP experiment 7.....	111
Figure 6.12 Bright field TEM micrographs from TMP 8 of Rsteel1	112
Figure 6.13 EDX spectrum from one precipitate observed in the sample of TMP experiment 8	112

Figure 6.14 a) Bright field TEM micrographs from TMP 4 of Rsteel2, b) EDX spectrum from the encircled precipitate	114
Figure 6.15 a) Bright field TEM micrographs from TMP 4 of Rsteel2, b) EDX spectrum from the encircled precipitate	115
Figure 6.16 Bright field TEM micrographs from TMP 3 of Rsteel2.....	116
Figure 6.17 a) Bright field TEM micrographs from TMP 9 of Rsteel3 b) EDX spectrum from the encircle precipitate	118
Figure 6.18 Data for yield strength of eutectoid and ultrahigh carbon steels are plotted against the inverse square root of pearlite interlamellar spacing	120
Figure 6.19 Comparison of results from ultra-high steels [118] and the developed steel	123
Figure 6.20 Three dimensional representation of the groove generated.....	125
Figure 6.21 Schematic representation of wear processes suggested.....	126

LIST OF EQUATIONS

Equation 2.1	8
Equation 2.2	14
Equation 2.3	15
Equation 2.4	19
Equation 2.5	22
Ecuation 2.6	31
Equation 2.7	32
Equation 2.8	32
Equation 4.1	51
Equation 4.2	51
Equation 5.1	59
Equation 6.1	121
Equation 6.2	121

ACKNOWLEDGMENTS

My appreciation and thanks for the accomplishment of this study are directed to Dr A.J. DeArdo and Dr. C.I. Garcia for their years of patience and guidance of this thesis. Without them this would not have been possible. I would also like to thank all BAMPRI and graduate students for their friendship, support and their enriching talks during my years at the University of Pittsburgh.

Special thanks to Dr. K. Goldman, for all his time spent on the proof-reading, as well as for making corrections to all my drafts.

Gratitude is expressed to my friends Francisco C. Robles Hernandez and Andreas Kurlovits for their friendship and support during these years.

I want to express all my gratitude to my wife, Yesica, for her constant proof of love, I want to thank my relatives and friends in Mexico for their invaluable support and encouragement.

Finally, I would like also to thank my parents, without whom this would have not been possible. I dedicate this work to my father who was the best man I have ever met.

1.0 INTRODUCTION

For more than 150 years, the steel rails have been the core of the world rail systems. Just in US and Canada, the total amount of installed railway track is about 40 million tons [1]. The main rail functions are to transmit the wheel forces to the track bed and guide the vehicle throughout the route. Like many metallic components that are exposed to cyclic loading, the rails are susceptible to metal fatigue and this can contribute to its partial and/or complete failure [2]. Since the introduction of railways, rail steels have been challenged by the continuous increase of wheel loads on the rails with increasing tonnage of traffic and rail life. The future demands on train traffic will involve heavier axle loads, higher train speed and the increase of traffic density. All these demands increase the risk of rail damages or even catastrophic rail failures. Steel producers trying to satisfy the demands of the railroad industry are constantly attempting to make great improvements and to control mechanical properties of rail steels. Most modern rail steels are fully pearlitic in their microstructure and carbon-manganese in composition [3,4]. These steels are commonly hyper-eutectoid in composition and exhibit good wear as well as fatigue resistance [5, 6].

The current market and technical demands require an increase of the efficiency of railroad systems, mainly (among other measures) higher axle load on rails. The increase in axle loads can contribute to a series of defects such as excessive wear, fatigue and, ultimately,

fracture of the steel rails [7]. It is well known that raising carbon content and refining the pearlite interlamellar spacing increases the hardness and strength of pearlitic steels. This has been shown to improve the wear and fatigue resistance [6]. Therefore, it is necessary to increase the hardness and strength of rail steels. Traditional methods to extend the rail life include alloying and heat treatment. Both strengthening and heat treatment improve the wear resistance while strengthening alone provides an additional advantage of enhancement in fatigue resistance [6,8].

Rail steels must fulfill at least five major property requirements: resistance to plastic deformation (corrugation), wear resistance, fatigue (rolling contact fatigue), residual stresses and weldability [4]. Although there has been a large amount of research trying to develop rail steels with different microstructure, i.e., bainitic and/or martensitic (tempered martensite) [2,9,10]. At the present time, the pearlitic steels still are the most common type of steel used to fabricate rails. However, there still remain several technical challenges, for example, the effect of pearlite colony size on mechanical properties, the shape and volume fraction of nonmetallic inclusions and their effect on rolling contact fatigue, prior austenite grain size and its effect on toughness, wear and rolling contact fatigue. The interlamellar spacing, which is a function solely of transformation temperature for a given composition, has been the most studied microstructured feature.

Several studies have been conducted in order to improve the performance of rail steels [4, 8-14]. However, limited attention has been paid to the influence of the proeutectoid phase on the performance of rails. It has been shown that the presence of proeutectoid cementite in austenite grain boundaries is a source of embrittlement in high carbon steels [15]. In addition, despite the numerous studies, it appears that the microstructure of pearlitic steels has not been fully optimized for this type of application.

It is well known, that refining the prior austenite grain size is beneficial in low carbon steels by promoting an increase of yield strength and a reduction in brittle transition temperature. For low-carbon steels, the ferrite grain size controls the strength and toughness. In the case of high carbon steels (of eutectoid or hyper-eutectoid composition), early studies have indicated that prior austenite grain size may not have a large effect on the Charpy transition temperature [13]. Other studies suggested that prior austenite grain size only has an effect at lower temperatures [16-18]. There is a lack of understanding of the development and performance of these steels regarding both the effect of austenite composition and grain size prior to transformation and the effect of cooling rate on the transformation temperature.

The main issue addressed in this research, therefore, was to develop understanding and guidelines for the optimization of fully pearlitic microstructures in terms of: a) Interlamellar spacing; b) Pearlite colony size; c) Control of the proeutectoid cementite formation; and d) The role of the prior austenite grain size on the kinetics of proeutectoid cementite.

An additional goal of this thesis was to contribute to the understanding of the complex subject of pearlitic rail steels, as well as to develop new processing strategies / routes that are more economically feasible than the current processing schemes and enhance the mechanical properties through modern alloying and microstructural design.

2.0 BACKGROUND

2.1 RAIL STEELS

The first metal used to manufacture rails (tramways) was cast iron. This material is brittle and, therefore, is not able to distribute the loads through plastic deformation. Due to these characteristics, it was not surprising to find rail failures everywhere. The steel rail became a practical choice by the second half of the 19th century. Bessemer, open hearth and other steel making processes had made relatively high production tonnages of steel possible. Consequently, longer rails were commonly hot rolled [11].

The performance of the rail steel, in particular its strength and ductility, was much better than the cast iron rail. This opened the doors for the fast development of railways throughout the world. Currently, steel has completely replaced the use of cast iron for rails. However, the steel rails still have many short-comings that lead to their failure.

Railway companies have increased freight transport weight in order to improve the transportation efficiency. Heavy haul railways attempted to extend the rail life. In recent years, the wheel load has been increased by 20%; these improvements were based on a technology to form fine pearlitic microstructure [16]. It is remarkable that previous improvements in rail life have not been achieved by modifying the chemical composition and microstructure of the rails [2]. Even though the manufacturers have performed many improvements in steel cleanliness and control of mechanical properties, most of the modern rails have pearlitic microstructures and

basically, carbon-manganese compositions and a pearlitic microstructure similar to those manufactured in the early 1900's [2].

Different approaches have been endeavored in order to improve the mechanical properties of rail. Modification of chemical composition, change of type of microstructure and even an increase in the number of manufacturing processes (quenching process) to refine the microstructure at select locations on the rail have been some of the principal attempts.

Work to develop bainitic steel rails with better mechanical properties (yield and tensile strength) and wear resistance has been undertaken by different researchers [2,9,19-21]. K. Sawley and J. Kristan [2] developed various bainitic steels, which were produced in an induction furnace in an argon atmosphere. After soaking for 2hr at 1288C (1561K) the ingots were rolled to 200mm X 76mm bars. Finishing rolling temperatures were between 940 and 954C (1213 to 1227K). No reported details on manufacture of these bainitic steel are available, but it is believed that no heat treatment was carried out.

The wear resistance and toughness of bainitic rail containing chromium and molybdenum have been assessed [22]. The rail head microstructure consisted of a mixture of 70% bainite and 30% pearlite but exhibited poor toughness; the wear on the gauge face where there is rolling sliding contact, was also worse. The bainitic steels reached higher tensile and fatigue strengths and performed well in service. However, several problems during welding have been registered. Service trials subsequently revealed that the bainitic steels wore faster than conventional pearlitic rails, when comparisons were made at the same hardness [23].

Studies with low carbon bainitic steel using laboratory tests indicated a wear rate some ten times faster than pearlite of the same hardness [24] Even mixed microstructures of bainite

and pearlite are found to be less wear resistant when compared with fully pearlitic steels Fig. 2.1 [25].

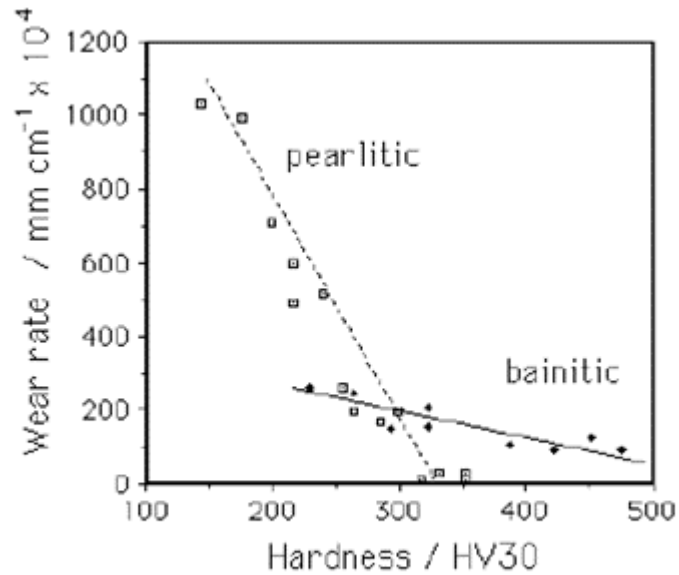


Figure 2.1 Pin-ring wear rate versus hardness data for pearlitic and bainitic steels

Nevertheless, studies from a number of researchers indicated that bainitic steel is not suitable for railway applications where rolling-sliding wear limits life [25]. There are still several efforts trying to use bainitic steel in railway applications [19,26-28].

Even though the newest bainitic steel developed for railways application have demonstrated similar or higher yield strength, hardness and ultimate strength than pearlitic steels (used for this application), a more thoughtful evaluation of properties in dynamic conditions is required.

2.2 PEARLITE MICROSTRUCTURE

The current rail steels are high carbon steels, commonly hyper-eutectoid steels, and they have a fully pearlitic microstructure. Pearlite is a two-phase lamellar product (or microconstituent) of eutectoid decomposition which can form in steels and in several non ferrous alloys (like Ti-Al and Ag-Ga) during transformation under isothermal, continuous-cooling, or forced cooling below the eutectoid temperature due to the cooperative and synchronized growth of two microconstituents from the austenite[17,18, 29]. The pearlite forms nodules and each nodule is made up of multiple colonies; each colony has parallel lamellae which have a different orientation with respect to the lamellae of neighboring colonies. Figure 2.2 [30] shows a schematic representation of microstructural components of a pearlitic steel. Figure 2.3 shows the micrograph of a pearlitic steel.

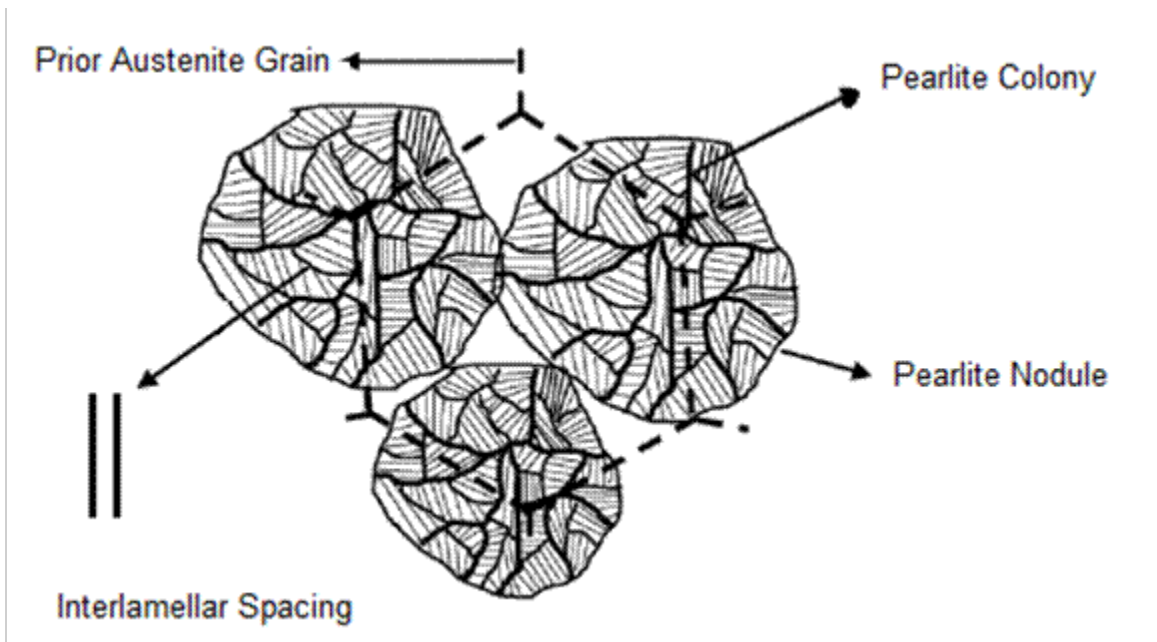


Figure 2.2 Schematic representation of different microstructural components of a fully pearlitic steel

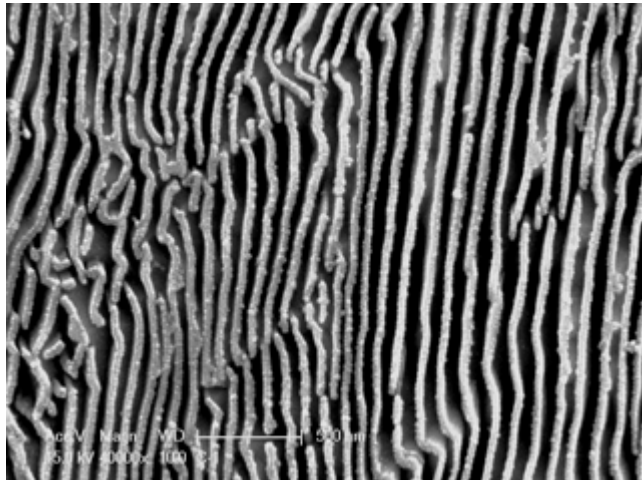
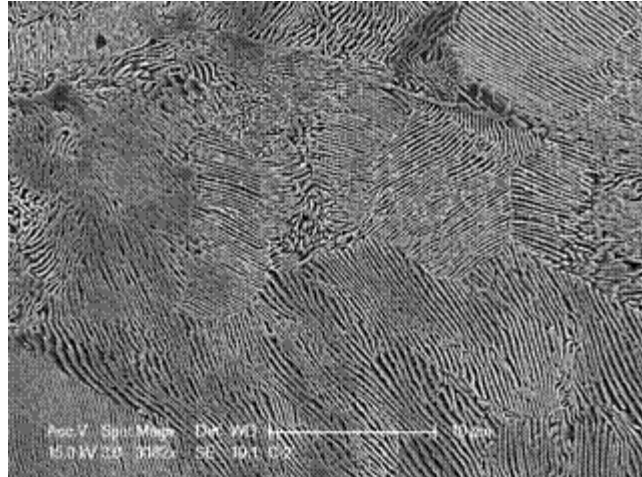


Figure 2.3 Typical pearlitic microstructure

When austenite containing approximately 0.8%wt C is cooled down to a reaction temperature below the A_1 (Figure 2.4) temperature, it becomes simultaneously supersaturated with respect to ferrite and cementite; then an eutectoid transformation results as shown in Equation 2.1



Pearlite nodules nucleate on γ grain boundaries and grow with a roughly constant radial velocity into the surrounding austenite grains. Under a small degree of undercooling below A_1 , the number of nucleated nodules are small, and they can grow as hemispheres or spheres, not interfering with each other. At larger undercooling, the nucleation rate is much higher and site saturation occurs; that is, all boundaries become saturated with nodules which grow together forming layers of pearlite. Figure 2.5 shows the pearlite nodule advancing into the austenite grain with hemispherical growth front [30a].

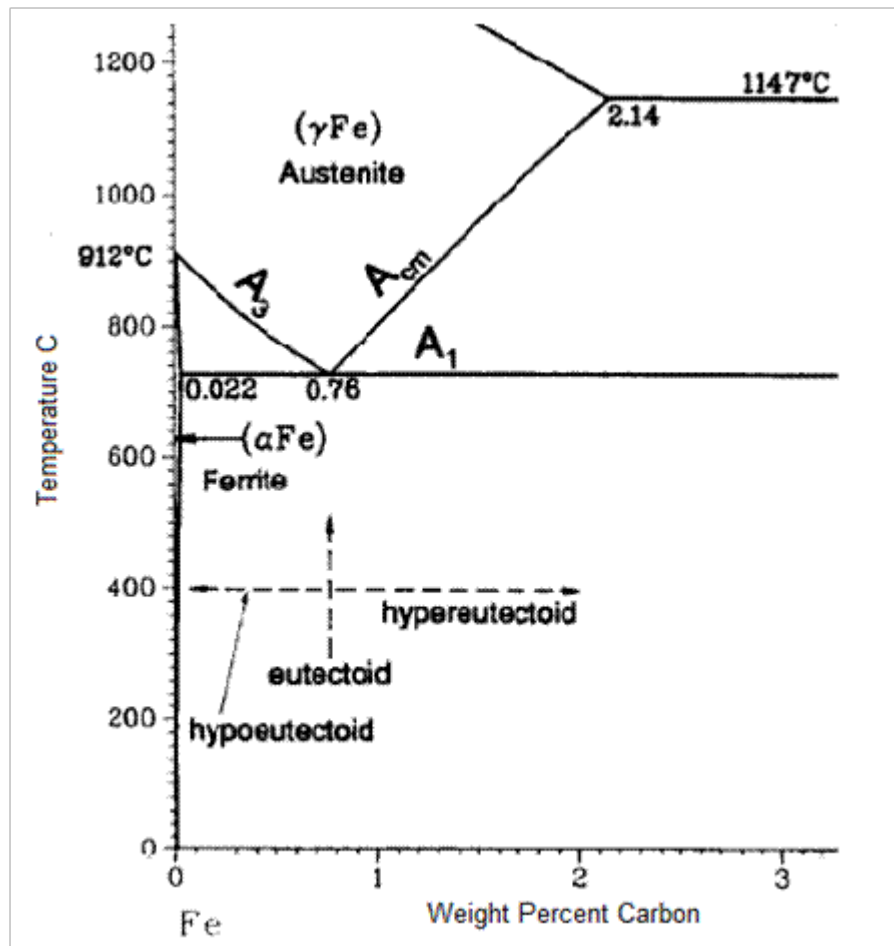


Figure 2.4 Partial of iron – iron carbide phase diagram

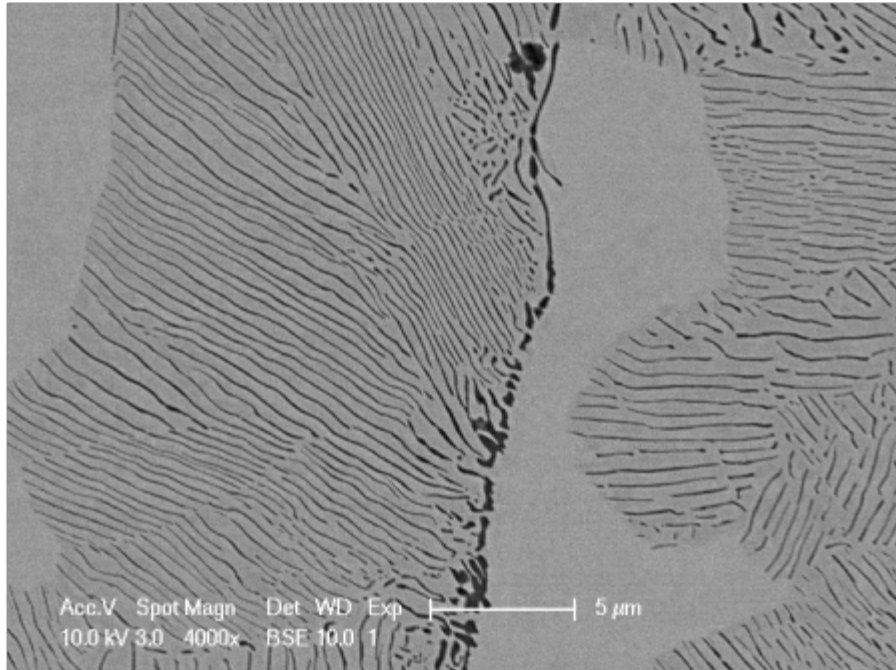


Figure 2.5 Micrograph of a pearlite nodule advancing into the austenite grain

2.3 PEARLITE NUCLEATION

The first step in the formation of pearlite is the nucleation of ferrite or cementite on austenite grain boundaries. Which one nucleates first depends on the composition, grain boundary structure and reaction temperature [31]. In hyper-eutectoid steel, cementite will usually nucleate first; in hypoeutectoid steel, the ferrite will nucleate first. Considering hyper-eutectoid steel, the cementite will nucleate first. The cementite will try to minimize the energy required for nucleation by forming an orientation relationship to one of the austenite grains, γ_1 . Therefore, the nucleus will have a semicoherent interface with γ_2 . The austenite surrounding the cementite nucleus will become depleted of carbon which decreases the driving force for ferrite nucleation.

The ferrite nucleates adjacent to the cementite nucleus with a special relationship to γ_1 . This process can be repeated causing the colony to spread sideways along the grain boundary. After nucleation of ferrite and cementite, the colony can grow edgewise by the movement of incoherent interfaces; that is, pearlite grows into the austenite grain with no relationship between them. The carbon rejected from the growing ferrite diffuses through the austenite in front of the cementite [33]. Figure 2.6 illustrates the pearlite nucleation and growth.

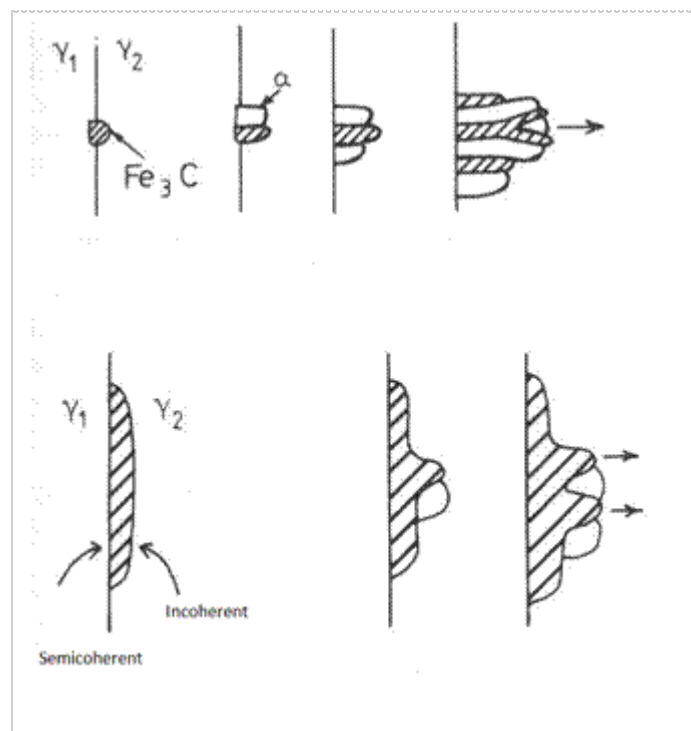


Figure 2.6 Nucleation and growth of pearlite

It has been observed that the formation of pearlite requires the establishment of the cooperative growth of ferrite and cementite. This cooperative mechanism gradually develops with time and finally the pearlite forms. In some hyper-eutectoid steels, a low degree of cooperation between ferrite and cementite resulted in non-lamellar growth of ferrite and cementite, thereby producing the so called degenerated pearlite structure. Partially coherent

interfaces strongly reduce the cooperation. When the two faces form in a noncooperative way, it is called a divorced eutectoid transformation (DET), in which the divorced cementite particles grow directly from the austenite along the cellular γ/α reaction front, without enclosure in ferrite shells [33]. The DET mode occurs at lower undercoolings compared with the pearlite mode observed at higher undercoolings [34,35]. An example of the degenerate pearlite microstructure is shown in Figure 2.7 [35a].

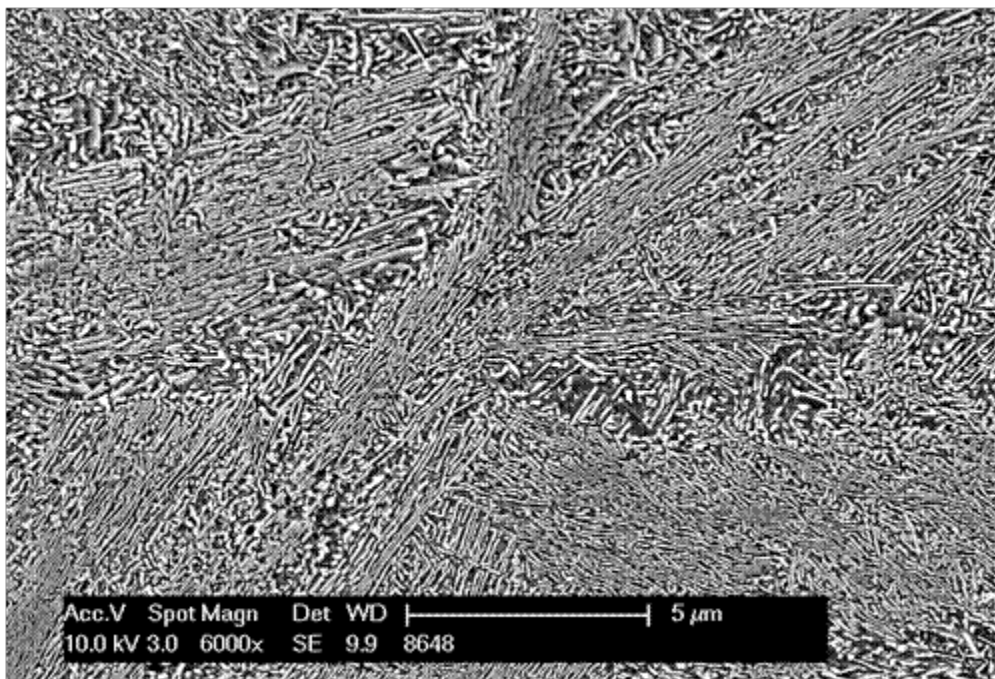


Figure 2.7 Degenerated pearlite microstructure

Another mechanism of the growth of pearlite is the branching mechanism. In this mechanism, all the cementite lamellae were branches from one single lamellae or nucleus of cementite which had grown from the cementite network, and all the ferrite lamellae also joined together to form a continuous crystal. It is, thus, considered that the pearlite unit is regarded as a

bicrystal comprising two interwoven crystals of ferrite and cementite [36]. During further growth, more branching occurs until the interlamellar spacing characteristic of the transformation is reached. Figure 2.8 illustrates, schematically, the branching mechanism [31].

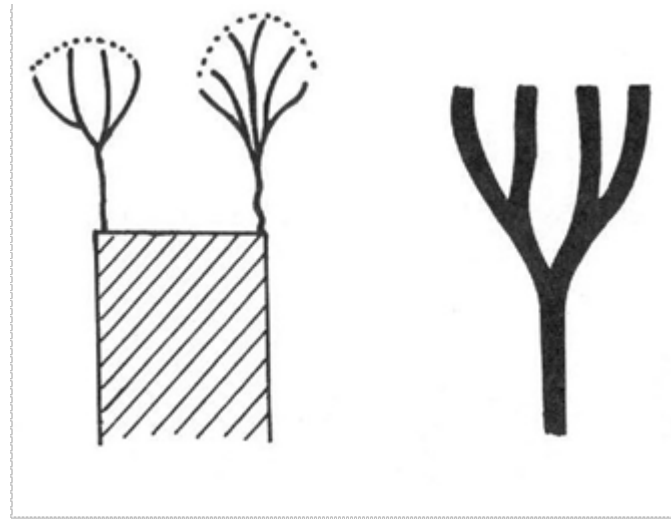


Figure 2.8 Schematic branching mechanism for the growth of pearlite

2.4 PEARLITE GROWTH

There are two principal but different theories proposed for the growth of pearlite. The Zener-Hillert theory assumes the volume diffusion of carbon in the austenite, ahead of the advancing pearlite, is the rate-controlling mechanism [37-39]. Another theory (Hillert theory), assumes that grain boundary diffusion of the carbon atoms is the rate-controlling mechanism [32].

In the most accepted theories of pearlite growth, the important parameters are the pearlite growth rate (G), and its interlamellar, spacing (S). This last one is to be assumed constant for a given temperature. During pearlite growth, the redistribution of carbon may occur in front of the

reaction front by volume diffusion through austenite and/or by diffusion along the pearlite – austenite interface [14, 35].

The Zener [36]–Hillert [40] equation for pearlite growth, G , is based on two important assumptions: 1) The austenite (supersaturated by carbon) is in local equilibrium with the constituents phases (ferrite and cementite) at the reaction front, and 2) Volume diffusion of carbon in austenite is rate controlling. The equation, arising from the flux balance of solute required for the reaction and from an accounting made for the influence lamellar interfacial energy has on the driving force for the growth, is given by:

$$G = \frac{D_c^\gamma}{k} \frac{S^2}{\tau^{cm} \tau^\alpha} \left(\frac{C_c^{\gamma^\alpha} - C_c^{\gamma^{cm}}}{C_c^{cm} - C_c^\alpha} \right) \frac{1}{S} \left(1 - \frac{S_c}{S} \right) \quad (2.2)$$

where D_c^γ is the volume diffusivity of carbon in austenite; k is a geometrical parameter; $C_c^{\gamma^\alpha}$ and $C_c^{\gamma^{cm}}$ are the equilibrium carbon concentrations in austenite in front of the ferrite and cementite lamellae, respectively; C_c^α and C_c^{cm} are the respective equilibrium concentration of carbon within the ferrite phase and cementite phase; τ^{cm} and τ^α are, respectively, the thickness of cementite and ferrite lamellae; S_c is the critical interlamellar spacing for which the growth rate becomes zero because the entire driving force is consumed as interfacial energy; and S is the interlamellar spacing. Figure 2.9 is a schematic representation of a pearlite growth model [41].

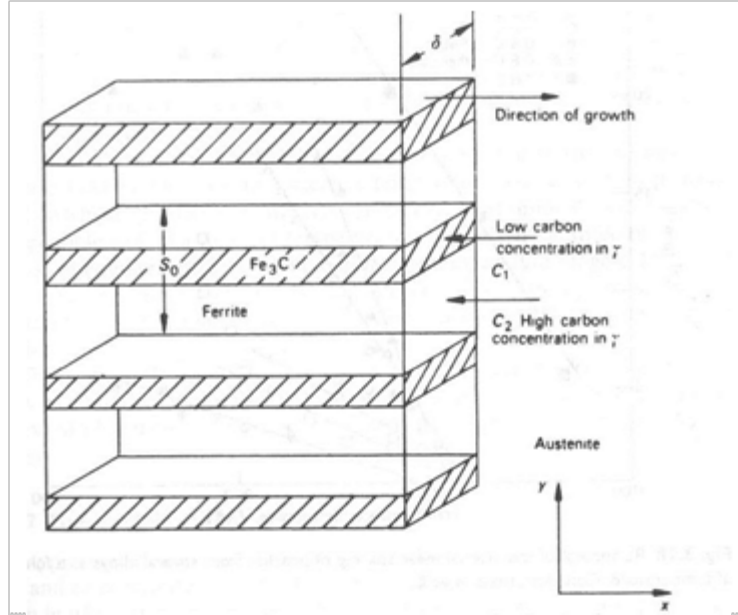


Figure 2.9 A pearlite growth model

Since equation (2) contains two unknown parameters, G and S , for a given ΔT , other solutions have been formulated. Boundary diffusion controlled pearlite growth has also been regarded by several authors [40-43]. All of them found similar results. The relationship due to Hillert [40] is:

$$G = 12KD_B\delta \frac{D_C^\gamma}{k} \frac{S^2}{\tau^{cm} \tau^\alpha} \left(\frac{C_c^{\gamma^\alpha} - C_c^{\gamma^{cm}}}{C_c^{cm} - C_c^\alpha} \right) \frac{1}{S} \left(1 - \frac{S_c}{S} \right) \quad (2.3)$$

where K is the boundary segregation coefficient, D_B is the boundary diffusion coefficient, τ^{cm} and τ^α are, respectively, the thickness of cementite and ferrite lamellae and δ is the boundary thickness. This equation assumes a major portion of solute redistribution by boundary diffusion and a smaller contribution by volume diffusion.

2.4.1 Effect of Alloying Elements on Pearlite Growth

The additions of small amounts of substitutional alloying elements such as Ni, Mn, Cr, Mo or Nb, result in a significant retardation of the pearlite reaction due to the change in the A_1 temperature and slow diffusion of alloy elements. It is well known that austenite stabilizers such as Mn and Ni reduce the A_1 temperature and, therefore, slow down the pearlite reaction because of the decrease of driving force of transformation at any given temperature below A_1 due to a reduction in concentration difference ($C_x^{\gamma\alpha}$ and $C_x^{\gamma\text{cm}}$) [44]. Figure 2.10 shows a comparison of pearlite growth rate in Mn and Ni steels [44].

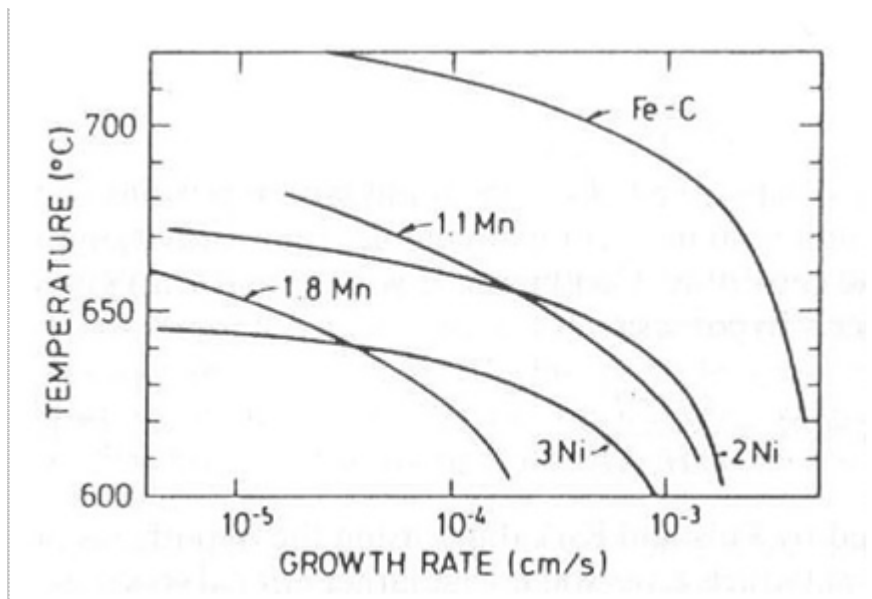


Figure 2.10 Comparison of growth rate curves of pearlite in nickel and manganese steels as a function of temperature

The carbide forming elements, like Si, Mo, Co, Cr, V and Ti, increase the A_1 temperature; in their presence, at lower temperatures, the transformation rates are usually lower than those in plain eutectoid steels. These alloying additions partition between ferrite and cementite over the entire range of pearlite formation. The drastic reduction in growth rate of pearlite at lower temperatures and the associated development of an austenite plateau in the TTT diagram have been attributed to the solute drag effect and partitioning of strong carbide formers [45]. Silicon is not an austenite-stabilizer element; in fact, it raises the ferrite austenite eutectoid temperature and significantly reduces the activity of carbon in ferrite [46]. In TRIP steels, the high Si content suppresses the formation of cementite during the bainitic transformation and it leads to an increase of stability and the amount of retained austenite [47]. In hyper-eutectoid steels, it is known that Si additions retard the precipitation of grain boundary cementite in hyper-eutectoid steels [48].

It is well known that during pearlite growth, the partitioning of alloying elements occurs at low supersaturation, favoring alloying element boundary diffusion controlled growth, while less partitioning occurs at high supersaturation. At high temperatures, strong solute partitioning occurs on low alloy pearlitic steels; with decreasing temperature, the partitioning becomes incomplete [45]. The substitutional alloying elements have low diffusivity, and, therefore, pearlite growth is controlled by the alloying element diffusion along the austenite-pearlite boundary

2.5 KINETICS OF PEARLITE FORMATION

The pearlite reaction is a typical nucleation and growth process [49]. That is, the rate of pearlite transformation depends on the nucleation of pearlite nodules, \dot{N} , and their growth rate, G . Different studies have shown that \dot{N} increases with time and during the decrease of temperature up to the knee temperature of the TTT curve for an eutectoid steel. Figure 2.11 shows the variation of nucleation and growth rate of pearlite with temperature [50]. The nucleation rate is a microstructure sensitive parameter because it is influenced by the prior austenite grain size, as well as other heterogeneities. Reducing the austenite grain size causes an increase in nucleation rate.

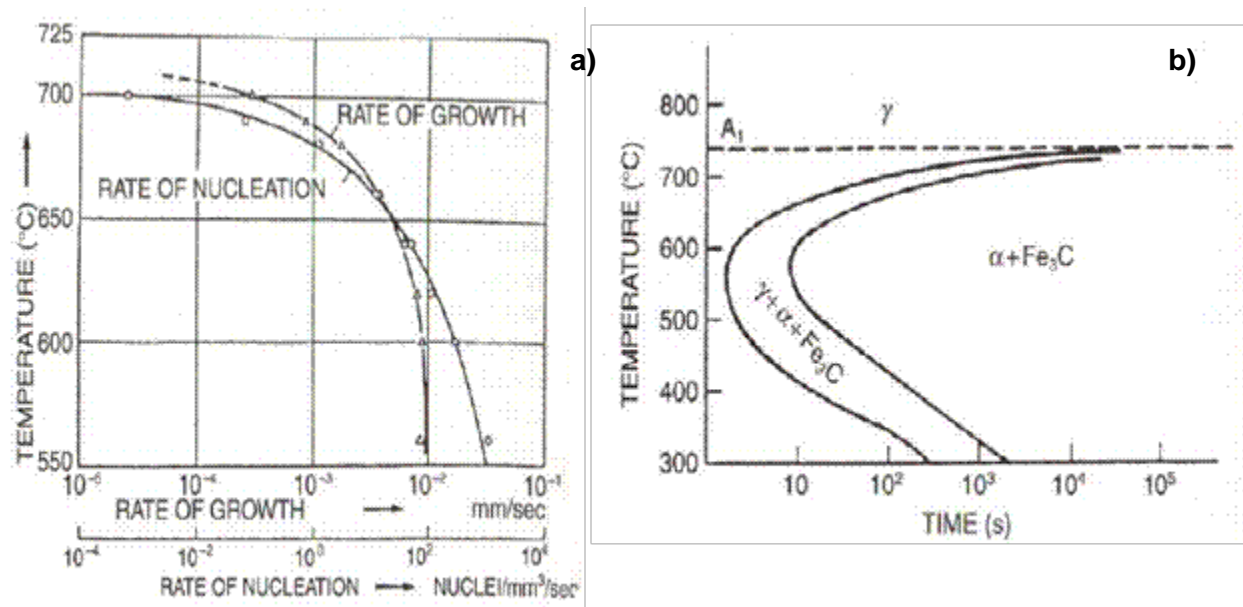


Figure 2.11 a) Variation of nucleation rate and growth rate of pearlite with temperature,
 b) Isothermal transformation curve for plain carbon steels

As \dot{N} and G increase with decreasing reaction temperature or increasing the degree of undercooling, ΔT , below the A_1 temperature, reaching the maximum \dot{N} and G at the nose of TTT curve, and decreasing subsequently at lower temperature. Even though G is microstructure insensitive, it is a strong function of both temperature and alloying elements. The pearlite nodules nucleate commonly on austenite grain boundaries, at temperatures below A_1 where the N/G ratio is not large. The reaction proceeds very slowly, therefore, the few nodules nucleate and grow without interfering with one another. Johnson and Mehl [51] found that the volume fraction of pearlite formed isothermally follows:

$$f(t) = 1 - e^{-\left[\frac{\pi N t^4 G^3}{s}\right]} \quad (2.4)$$

where $f(t)$ is the volume fraction of pearlite formed isothermally at a given time t , N is the nucleation rate, assumed to be constant; and G is growth rate, also assumed to be constant.

At a large degree of undercooling, the nucleation rate is much larger and many small nodules nucleate and site saturation occurs [52]. The transformation simply proceeds by the thickening of pearlite layers into the grains [52,53].

2.5.1 Effect of Alloying Elements on the Eutectoid Composition and Temperature

The ferrite and austenite stabilizers enlarge the respective phase field. Adding alloy elements to the iron-carbon alloy (steels) makes the location of transformation lines A_1 , A_3 , A_{cm} and the eutectoid composition change. An example of how the ferrite and austenite stabilizers change the

transformation lines is shown in Figure 2.12 [54]. From this figure is clear that only 1wt% of Ti is enough to practically eliminate the γ field; on the other hand, 20wt% of chromium is needed to reach the same result.

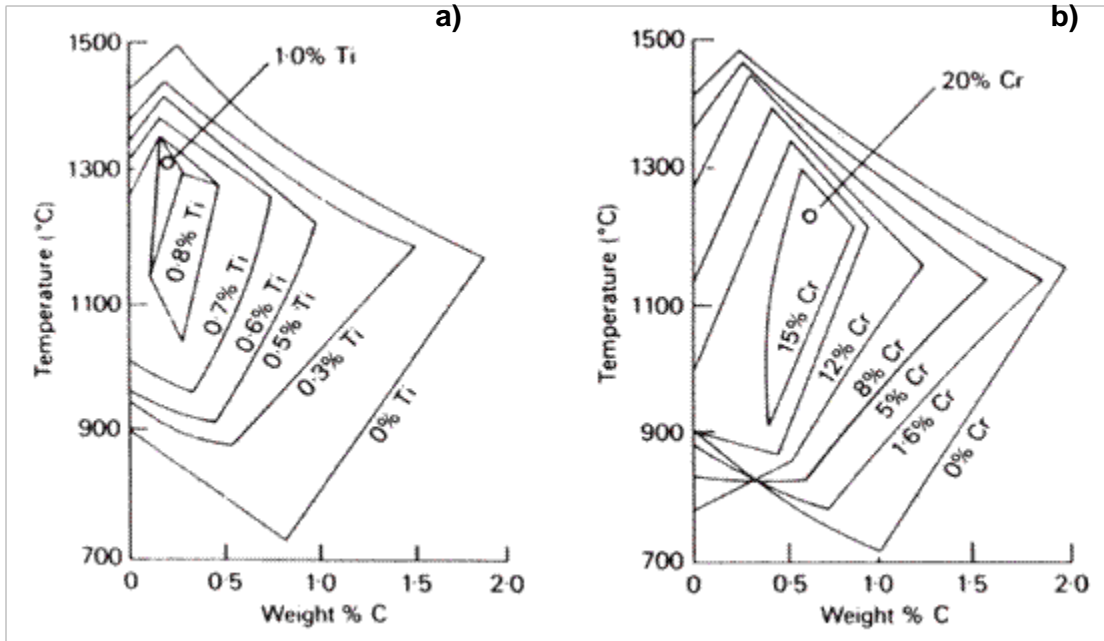


Figure 2.12 Effect of alloying elements on γ phase field: a) Titanium, b) Chromium

Bain [55] introduced diagrams in which can be seen the influence of increasing the amount of certain elements on the eutectoid carbon content and A_1 temperature. Figure 2.13a shows the influence on eutectoid temperature and 2.13b, shows the related influence on eutectoid carbon content [56,57]. The austenite stabilizers reduce the eutectoid temperature thereby widening the temperature range over which austenite is stable.

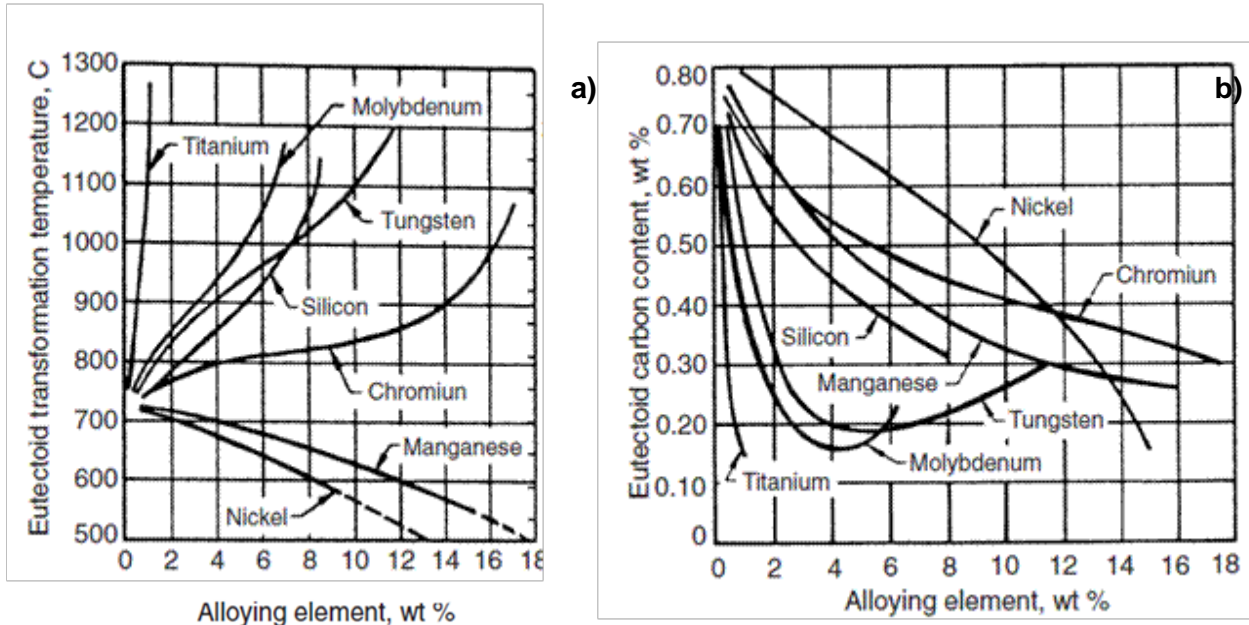


Figure 2.13 Effect of alloying elements on a) Eutectoid reaction temperature and b) Eutectoid carbon content

2.5.2 Interlamellar Spacing

The interlamellar spacing is a very important microstructural parameter of eutectoid steels controlling strain hardening and ductility. Fine pearlite is a desirable microstructure for pearlitic steels with an exponential strain hardening rate resulting in a final high tensile strength [58]. The reduction of interlamellar spacing generates a reduction of cementite thickness. The pearlitic constituent, having lower than the equilibrium carbon content, is called diluted pearlite. More diluted pearlite can be obtained by decreasing either the eutectoid carbon content by additions of alloying elements or by decreasing the transformation temperature which can lead to the formation of more than the equilibrium amount of pearlite in hypoeutectoid steels. Thus, a dilute pearlite can provide a good combination of strength and toughness [59].

In pearlitic steels, the relation between the volume fraction of pearlite, f_p , initial interlamellar spacing, S , and cementite thickness, t , can be expressed as indicate in equation 2.5 [60]. The increased interlamellar spacing leads a thicker cementite lamella.

$$t = 0.15 (\text{wt}\% \text{C}) S / f_p \quad (2.5)$$

2.6 CEMENTITE

Cementite, or iron carbide, contains 6.67% C (by weight) or 29 at % corresponding to the formula Fe_3C . Cementite is a metastable Fe-C intermetallic compound. In carbon alloy steels, some of carbide-forming elements, for example manganese and chromium, will replace some of the iron in cementite; therefore, the formula for cementite is often referred to as M_3C , where M represents the carbide forming elements present [61].

The cementite structure is orthorhombic with 12 iron atoms and 4 atoms of carbon in the unit cell. Its lattice dimensions have been measured by different approaches. Examples of these dimensions are: $a = 4.5155 \text{ \AA}$, $b = 5.0773 \text{ \AA}$ and $c = 6.7265 \text{ \AA}$ [62] or $a = 5.0896 \text{ \AA}$, $b = 6.7443 \text{ \AA}$, and $c = 4.5248 \text{ \AA}$ [63].

In cubic close-packed (FCC) iron, ($\gamma\text{-Fe}$), the volume per atoms is 11.47 \AA^3 , and in the body center structure ($\alpha\text{-Fe}$), it is 3 percent greater. The corresponding free volume per iron atom in cementite (Fe_3C) is 12.94 \AA^3 . This is 12 percent greater than the close packed volume. Cementite has a different crystal structure and is an ordered compound. Pearlite is composed of approximately 12 percent of cementite. The iron lattice in the cementite structure differs from the close packed structure by reason of the necessity to accommodate carbon atoms in the ratio

1:3[63]. It is ferromagnetic with a Curie temperature of 215C. In contrast to ferrite and austenite, cementite is hard (over VH 1300) and brittle. Cementite has a low tensile strength but high compressive strength [64].

This phase plays an important role on the mechanical properties of commercial steels. W. J. Kim and O. D. Sherby [65] measured the influence of the volume fraction of cementite on the hardness of hyper-eutectoid steels. Figure 2.14 shows how the hardness increases as the volume fraction of cementite increases. These results suggest that the strength of the cementite phase is higher than that of ferrite phase at low temperature [65].

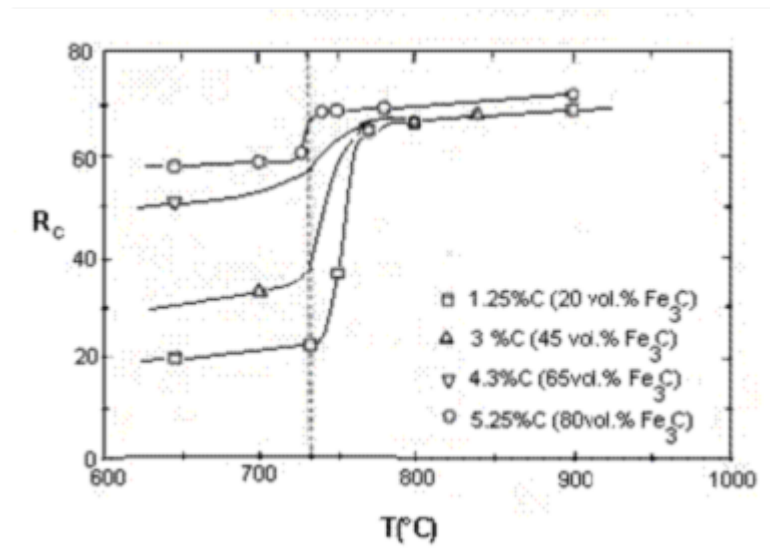


Figure 2.14 Hardness test measurements for Fe-C alloys

The effect of cementite volume fraction on superplasticity has been also estimated. In Figure 2.14 the tensile elongation data from ingot processed Fe-C alloys as a function of volume fraction of cementite at a given temperature and different strain rates, can be seen. It is clear in

Figure 2.15 that the elongation increases as the cementite volume fraction increases up to a value of 25%, having an optimum value at 27%. However, this property decreases from the optimum values to higher values of cementite volume fraction.

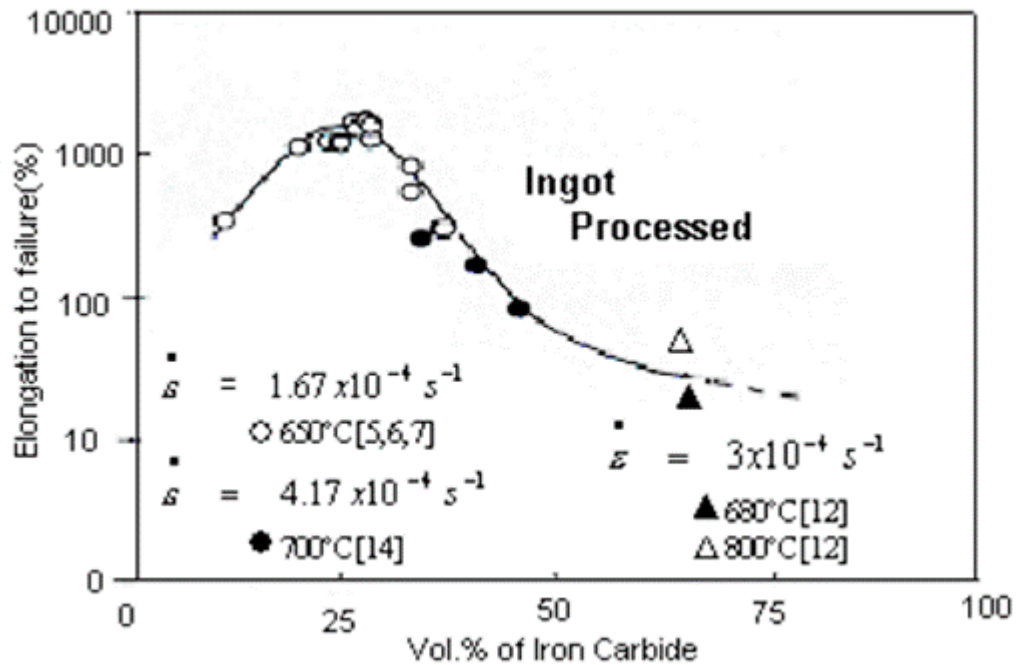


Figure 2.15 Tensile elongation data as a function of volume fraction of cementite

2.6.1 Proeutectoid Cementite

When steels with carbon content higher than the eutectoid composition (hyper-eutectoid steels), are heated above the transformation temperature, A_{cm} , for a time necessary to obtain an homogeneous austenite, and then it is continuously cooled through the transformation temperature, A_{rcm} , the first phase formed, is the proeutectoid cementite. This phase is formed along the austenite grain boundaries and in other defects (and in some cases in undiluted carbides) upon cooling between A_{rcm} and A_{r1} . Figure 2.16 shows an example of proeutectoid

cementite in eutectoid steels. The cementite has formed a thin network along the prior austenite grain boundaries and the balance of the microstructure is pearlite formed below A_{r1} . After longer transformation times, proeutectoid cementite may also precipitate intragranularly, usually in the form of Widmastatten plates [66].



Figure 2.16 Optical micrograph showing proeutectoid cementite network on prior austenite grain boundaries

In a better examination, M.V. Kral and G. Spanos [67] have shown that the proeutectoid cementite in the prior austenite grain boundaries reveals a fernlike or dendritic characteristic, as in shown in Figure 2.17.

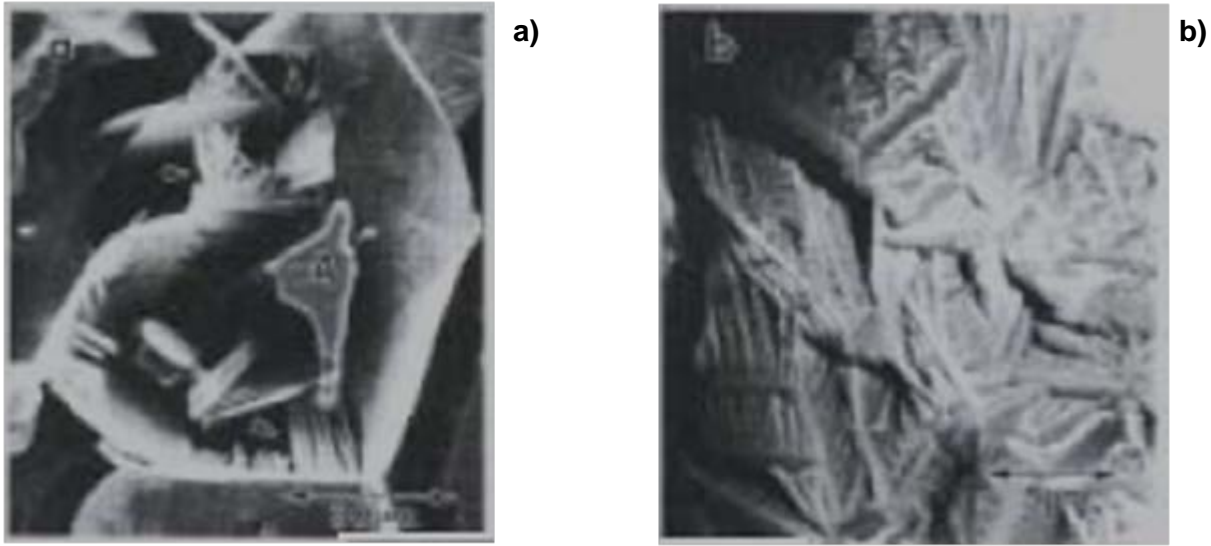


Figure 2.17 SEM micrographs of deep etched samples. a) Proeutectoid cementite grain film with dendritic feature. b) Fernlike cementite precipitated covering grain boundaries

The eutectoid and hyper-eutectoid steels are used in a number of important applications where high strength, wear resistance, ductility, toughness and low cost are important. The most important of these applications are the high strength wires and high strength rails. In wire rods, the precipitation of proeutectoid cementite along the grain boundaries deteriorates the drawability. In other applications, the presence of this phase on the grain boundaries has been identified as a source of embrittlement [15]. One of the mechanical properties affected by the presence of proeutectoid cementite is the toughness. Steels with the same grain size, pearlite content, cementite grain boundary network, and similar strength can vary in impact transition temperature. This has been related to the difference in thickness of the proeutectoid cementite networks [68]. Even though several investigations have been conducted on the effect of different alloying elements on the cementite precipitation, their influence on the type of precipitate and the nucleation sites is still not completely understood. An alloying element having a higher carbide

solubility than the ferrite is not likely to have a large effect on the growth rate of the carbide. However, it may control the structure of carbide precipitated. On the other hand, if the alloying element is essentially not soluble in the carbide, it can have a large effect on the rate of growth of the carbide [69].

2.6.2 Orientation Relationship between Austenite and Cementite

An understanding of the crystallography of any transformation is important since the properties of the interfaces depend on the relative disposition of crystals that they join. The development of morphology also depends on crystallography since this determines the orientation of the interface energy [70].

The frequency of occurrence of any particular orientation usually far exceeds the probability of obtaining it by simply taking two separate crystals and connecting them in an arbitrary way. This indicates that there are favored orientation relationships, perhaps because it is these which allow a best fit at the interface between the two crystals. This would reduce the interface energy and hence, the activation energy for nucleation. Embryos which happen to be oriented in this manner would find it relatively easy to grow into successful nuclei, giving rise to a non-random distribution [70].

A pearlite colony is two interpenetrating single crystals of ferrite and cementite, neither of which is orientation related to the austenite grain in which they are growing. However, there is always a well defined crystallographic orientation between the ferrite and cementite. At least two different relationships have been identified, they are [71]:

Pitsch /Petch relationship

$$(001)_c // (521)_\alpha \quad (010)_c \text{ 2.6}^\circ \text{ from } [113]_\alpha \quad (100)_c \text{ 2.6}^\circ \text{ from } [1\bar{3}1]_\alpha$$

Bagaryaski relationship

$$(100)_c // (0\bar{1}1)_\alpha \quad (010)_c // (0\bar{1}\bar{1})_\alpha \quad (001)_c // (211)_\alpha$$

When the cementite precipitates first in an eutectoid steel, the cementite will try to minimize the activation energy barrier to nucleation by forming with an orientation relationship to one of the austenite grains, γ_1 . The crystal structure of cementite is orthorhombic and the orientation relationship is close to:

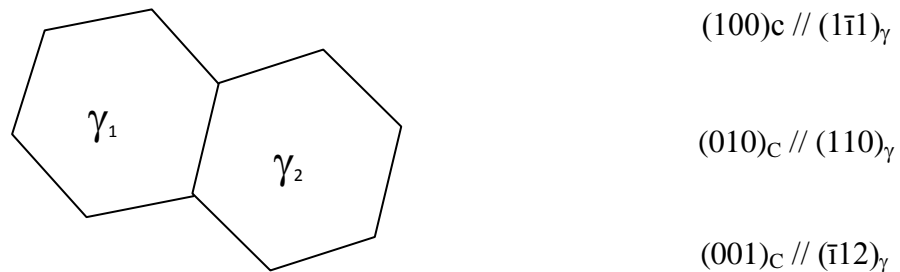


Figure 2.18 Schematic representation of austenite grains

Therefore, the nucleus will have a semicoherent, low mobility interface with γ_1 and an incoherent mobile interface with γ_2 . The austenite surrounding this nucleus will become exhausted of carbon which will increase the driving force for the precipitation of ferrite and a

ferrite nucleus will form adjacent to the cementite nucleus, also with an orientation relationship to γ_1 (the Kurdjumov –Sachs relationship) [32]. See Figure 2.18.

2.7 THE EFFECT OF PRIOR AUSTENITE GRAIN SIZE ON THE SIZE OF THE PEARLITE NODULES

The initiation of a pearlitic microstructure from austenite entails the formation of neighboring nuclei of ferrite and cementite on an austenite grain boundary. Supposing that initially, only one nucleus of cementite forms on this boundary, this region will be locally rich in carbon, which was obtained from the immediate surroundings. This then, reduces the carbon content on either side of the cementite nucleus and encourages the adjacent nucleation of ferrite. If this occurs and the cooperative process continues, adjacent nuclei of alternating ferrite and cementite are formed.

This sequence leads to the transformation of austenite to a lamellar product that has a specific spatial orientation in which the ferrite and cementite phases are parallel to each other within a colony region. In reality, for each colony of pearlite, the lamellae are mostly parallel and are frequently curved. However, different pearlite colonies have different lamellae orientations, and, as the transformation continues, neighboring colonies of lamellae join and continue to advance into the austenite, such that when the transformation occurs at low degrees of undercooling, the colony groups advance by a transformation front that is roughly spherical in shape, leading to the formation of a pearlite nodule.

Eventually, as the nodules continue to grow and they impinge on one another to complete the transformation. If the temperature at which the transformation is occurring is decreased, such that the undercooling allows the nucleation process to become so fast that all of the austenite grain boundaries are consumed very quickly during transformation, the pearlite nodules are then observed to be in contact along the prior-austenite boundaries as a continuous cementite network. In previous work, A.M. Elwazri et al. [72], have shown that the austenite grain size has a direct effect on the pearlite nodule; the larger is the austenite grain size the larger is the pearlite nodule, as shown in Figure 2.19.

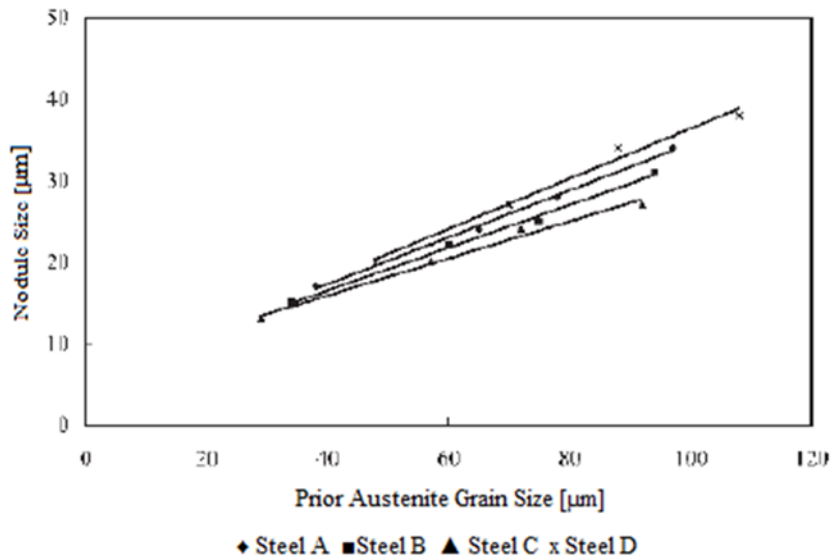


Figure 2.19 Effect of prior-austenite grain size on the nodule size for hyper-eutectoid steels

2.8 ROLE OF MICROSTRUCTURE ON THE MECHANICAL PROPERTIES

The relation of microstructure to the mechanical properties in carbon steels has been the subject of considerable research. It is well known, for example, that increasing the carbon content

increases steel's strength, but usually only at the expense of fracture toughness. More specifically, however, there is considerable debate as to how microstructure variations affect mechanical properties [73]. It is generally agreed that in high carbon, near-eutectoid steels, it is the pearlite rather than proeutectoid ferrite that controls strength, and refining the pearlite interlamellar spacing results in an increase in yield strength [73-75]. There have been conflicting results reported in the literature as to the effect of pearlite interlamellar spacing, pearlite colony size and prior austenitic grain size on the toughness of steels. This is because, in part, it is difficult to isolate the contribution of each of the microstructural variables.

In general, information [76-79] has been found that pearlite interlamellar spacing has an effect on the yield strength, following the Hall-Petch relationship:

$$\sigma_{yield\ strength} = \sigma_i + K_y \lambda^{-\frac{1}{2}} \quad (2.6)$$

where σ_i is the friction stress required for dislocation to move through the lattice; K_y is Hall-Petch slope and λ is the interlamellar spacing.

Values of σ_i and K_y obtained by Bouse et al. [77], for non-vanadium steels, are -342 MN/m² and 0.381 MN/m^{3/2}, respectively, and for the vanadium steels -313 MN/m² and 0.436 MN/m^{3/2}, respectively. Karlsson and Linden [80] (Figure 2.20) have summarized existing data for eutectoid steels and suggest a best mean value for K_y . Apparently, additions of manganese, silicon and vanadium all help to increase the Hall-Petch slope of the primarily pearlite microstructure.

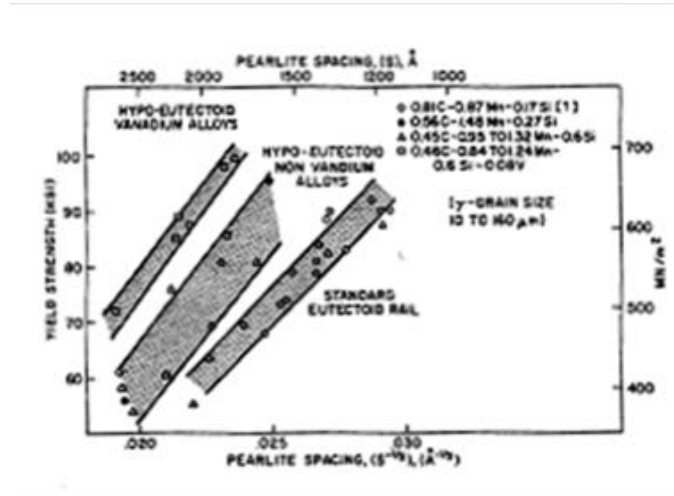


Figure 2.20 Yield strength as a function of the pearlite interlamellar spacing for eutectoid and hypoeutectoid steels

As the carbon content decreases, the alloy microstructure becomes a ferritic-pearlitic mixture, and the pearlite can become contained in isolated grains, often surrounded by ferrite grains. When this occurs, the dependence of strength in the pearlite spacing drops rapidly.

Eric M. Taleff [79], proposed a relationship of interlamellar spacing and pearlite colony size with the yield strength for ultra-high carbon steels, based on the Hall-Petch equation.

$$\sigma_{yield\ strength} = 310(\sqrt{2}\lambda)^{-\frac{1}{2}} + 460 P^{-\frac{1}{2}} \quad (2.7)$$

where λ is the interlamellar spacing; P is the pearlite colony size. The length is in units of μm and the stress in units of MPa.

J.M. Hyzak and I.M. Bernstein [73] found that yield stress had a strong relationship with the pearlite interlamellar spacing. See Equation 2.8.

$$\sigma_{yield\ strength} = 316\lambda^{-\frac{1}{2}} - 5.79 \times 10^{-2}P^{-\frac{1}{2}} - 4.17 \times 10^{-1}D_{\gamma}^{-\frac{1}{2}} + 7.58 \quad (2.8)$$

where λ is the interlamellar spacing; P is the pearlite colony size and D_γ is the prior austenite grain size.

Equation 2.7 shows that increases in yield strength correlate best with decreases in pearlite interlamellar spacing, and although the prior austenite grain size also has an effect on strength, the correlation is not as great. Indeed, further analysis indicates that pearlite spacing alone can account for 84% of the variation of the stress while prior austenite grain size accounts only for 3.7%. Variation in pearlite colony size has a minimal effect on strength [73-81].

Results from different sources [52,79] indicate that yield strength does increase, somehow, as the prior austenite grain size increases. This effect is attributable to the relationship between prior austenite grain size and interlamellar spacing. For a given isothermal transformation temperature, pearlite spacing decreases as the prior austenite grain size increases. An example of this effect is shown in Figure 2.21 for ultra-high carbon steels (UHCS).

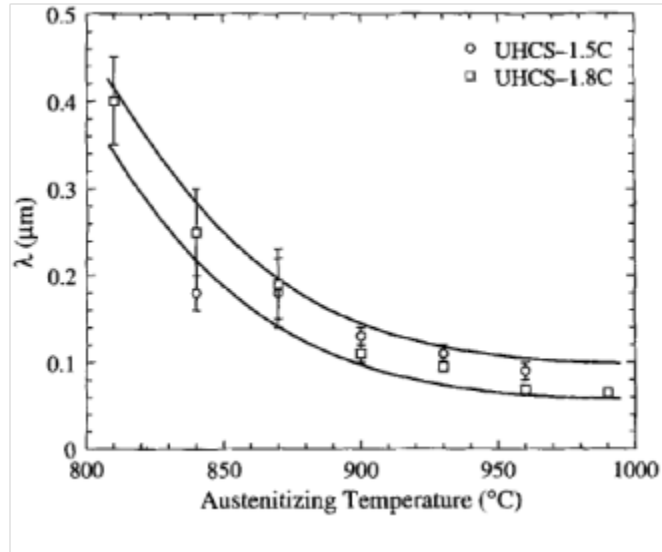


Figure 2.21 Pearlite interlamellar spacing versus austenitizing temperature for UHCS

A.M. Elwazri and P. Wanjara [82], working with hyper-eutectoid steels, showed a direct relationship between the yield and tensile strength with the interlamellar spacing. Figure 2.22 shows this relationship. Information from Gladman, et al. [74], Hyzak and Bernstein [73] and Taleff, et al. [79], on eutectoid steels and ultra-high carbon steel (1.5 – 1.8 %C) sustain the idea that strength varies linearly with the inverse square root of interlamellar spacing.

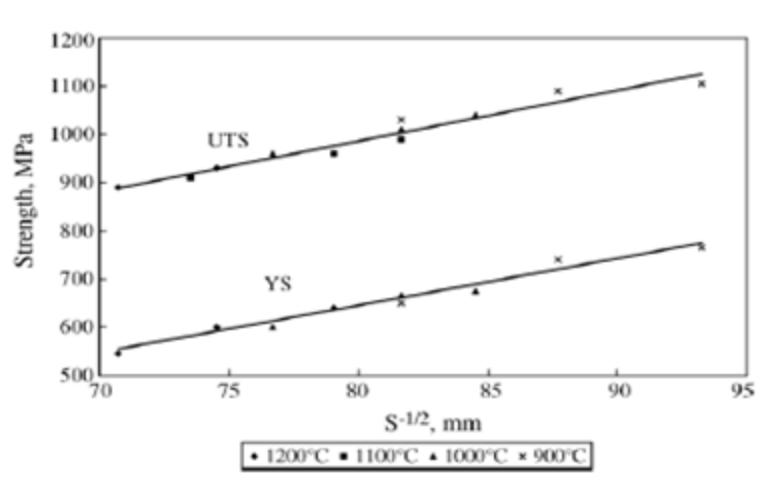


Figure 2.22 Interrelation between the strength and interlamellar spacing

Among the mechanical properties that are strongly affected by the interlamellar spacing, the hardness has a close relationship with this microstructural characteristic. Figure 2.23 shows how the hardness correlates with pearlite interlamellar spacing. This is from the work of Clayton and Danks [83].

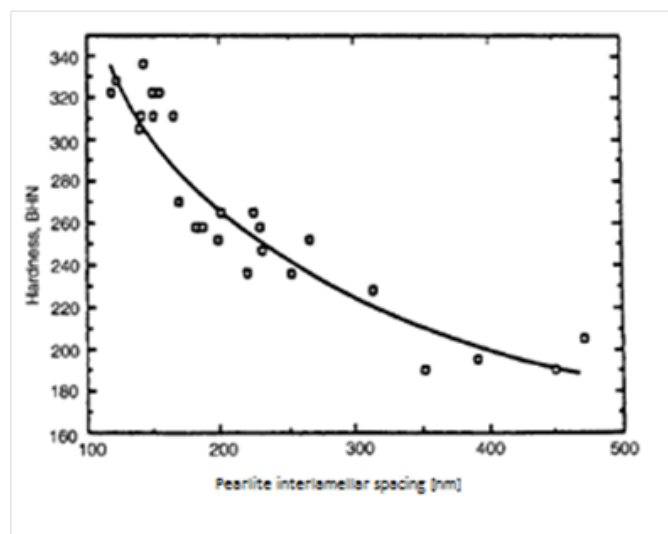


Figure 2.23 Hardness as a function of pearlite interlamellar spacing for various rail steels

Refining the prior austenite grain size is beneficial in low carbon steels by promoting an increased yield strength and a reduction in the Charpy transition temperature. For low-carbon steels, the ferrite grain size controls the strength and toughness. In the hypoeutectoid steels, prior austenite grain size has been found to exercise primary control over toughness. It has been observed [50, 73] that the finer prior austenite grain sizes reduce the transition temperature. Figure 24a) and b), indicates the dependency of austenite grain size on the transition temperature. Figure 24b) shows that the Charpy transition temperature is shifted down the temperature scale as the grain size is decreased, with the pearlite spacing maintained at a constant value.

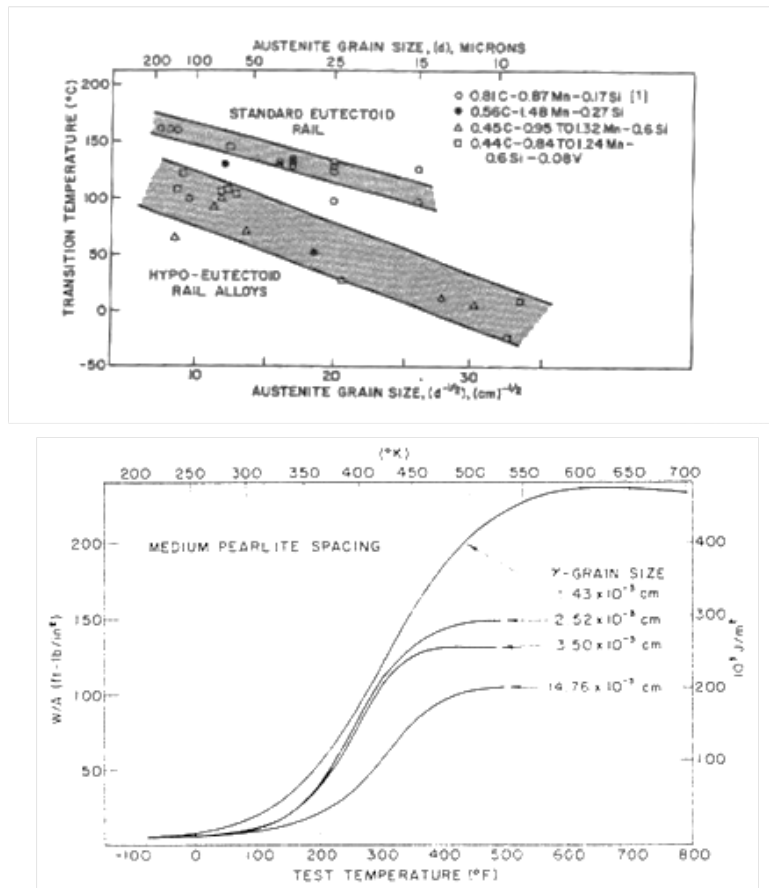


Figure 2.24 a) Dependency of prior austenite grain size on the transition temperature b) Charpy transition curves as a function of prior austenite grain size

2.9 WEAR - MICROSTRUCTURE AND MECHANICAL PROPERTIES RELATIONSHIP

It has been considered that the wear in rail steels has three different stages [83]. The first stage consists of severe plastic deformation in a thin surface layer of the rail, with a depth around 0.1mm. This is caused by the repeated heavy compressive and shear loading produced by the wheel. The second stage consists of the development of subsurface cracks in the severe deformation layer, commonly at the interface of the deformed layer and the undeformed microstructure. The third stage of wear is the propagation of cracks to the surface of the rail and the associative spalling off to small slivers or flakes from the rail. This sequence of deformation and fracture is repeated many times to produce substantial rail wear.

The classic view of wear has shown that improved rail wear resistance correlates with interlamellar spacing of pearlitic microstructures (Figure 2.25b), which formerly was related to the strength (Figure 2.22) and hardness (Figure 2.23). Decreasing the interlamellar spacing increases the value of these mechanical properties. Clayton and Danks [83] have shown in previous work that wear has a relationship with the hardness in eutectoid steels. Figure 25a shows the hardness correlation with wear resistance for rail steels. The higher the hardness of the steel, the lower is the wear of the rail. Consequently, the rail wear can be related as being directly proportional to the interlamellar spacing, as shown in Figure 25b [84].

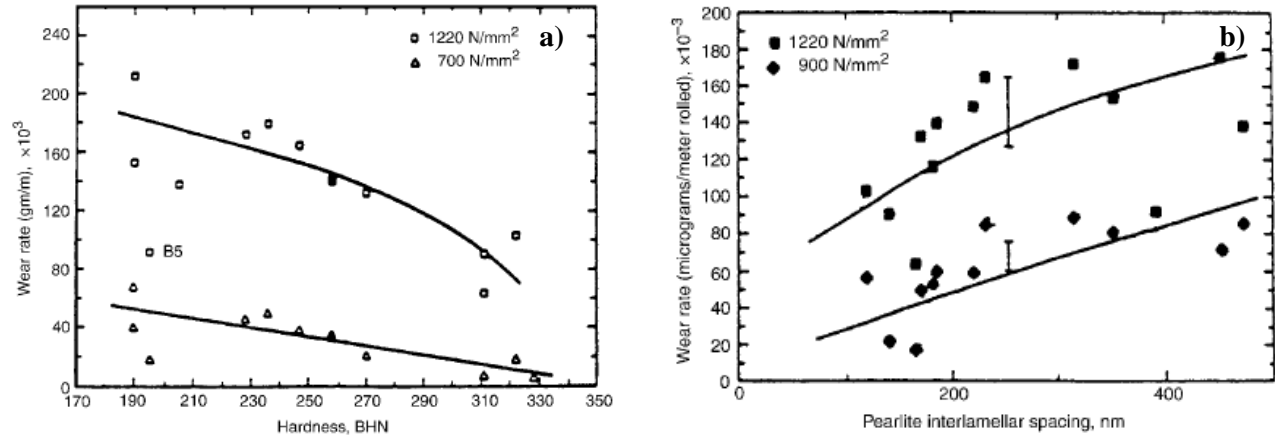


Figure 2.25 a) Wear resistance as a function of hardness for various rail steels tested at contact pressures of 1220 N/mm² and 700 N/mm², b) Wear rate as a function of pearlite interlamellar spacing for various rail steels tested at contact pressure of 1220 N/mm² and 900N/mm²

2.10 DEFORMATION OF PEARLITE

There are two remarkable deformation mechanisms in pearlite, homogeneous and inhomogeneous deformation [85]. The inhomogeneous deformation takes place when one highly stressed slip system in the ferrite is nearly parallel to the plane of the lamellae. Homogeneous deformation takes place when the slip distances of all operative slip systems in ferrite are approximately equal.

Coarse pearlite has low strength and initially deforms by dislocation generation at the ferrite/cementite interface. As the deformation continues, slip localizes into slip bands which create offset in the cementite [86]. These offsets act as stress concentrators, thus increasing the fiber-loading stresses in the lamellae. Fracture of the cementite ensues, creating an easy path for further deformation, increased shear in the neighboring ferrite along the slip band followed by

fracturing adjacent cementite lamellae [86]. Eventually, voids form in the ferrite at the fracture ends of the cementite lamellae. The local stresses are concurrently elevated by work hardening, even during void growth, eventually producing rapid brittle fracture in a tensile specimen when the local stresses reach the cleavage value [87]. All these processes are called the shear cracking process. Figure 2.26 shows the mechanism of pearlite deformation.

Fine pearlite, on the other hand, possesses higher strength and deforms in a more homogeneous manner. Slip is more homogeneous, but slip bands are more closely spaced. The finer cementite also behaves in a more ductile manner, as it may break by necking rather than failing in a brittle manner. Cleavage fracture intervenes in this ductile behavior, interrupting the void growth process. Even though, both (coarse and fine) microstructures fail by cleavage, the mode of fracture mode initiation apparently differs.

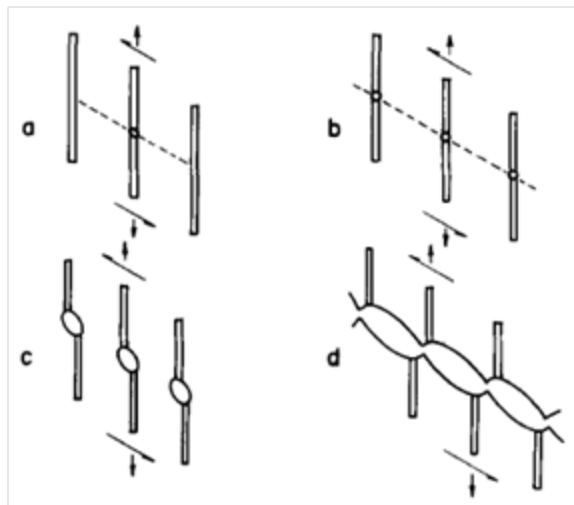


Figure 2.26 Shear cracking of pearlite, a) Cracking of cementite plate; b) Shear zone developing in the ferrite causing cracking of neighboring plates, c) Void formation and d) void coalescence

3.0 STATEMENT OF OBJECTIVES

The general objective of this investigation was to develop understanding and guidelines for the optimization of fully pearlitic microstructures in terms of:

A) Interlamellar spacing; B) Pearlite colony size; C) Control and elimination of the proeutectoid cementite formation; and D) The role of the prior austenite grain size on the kinetics of proeutectoid cementite. To achieve this objective, we analyzed thirteen commercial steels provided by the sponsor of this research.

An additional goal of this thesis was to contribute to the understanding of the complex subject of pearlitic rail steels, as well as to develop new processing strategies / routes that are more economically feasible than the current processing schemes and enhance the mechanical properties through modern alloying and microstructural design.

4.0 EXPERIMENTAL PROCEDURE

Before developing any alloy design, and in order to gather more information of the type of steel we were working with, a systematic microstructural assessment of thirteen commercial steels was conducted. The microstructural assessment was performed in terms of interlamellar spacing, pearlite colony size as well as prior austenite grain boundaries, determination of proeutectoid cementite and the assessment of the non-metallic inclusions. From each steel we cut samples from three different locations of the rail. Figure 4.1 shows the rail profile and the location from which the samples were taken.

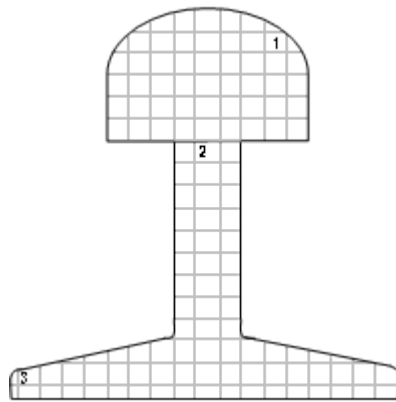


Figure 4.1 Rail profile, indicating sampling locations

With the information collected by the microstructural assessment, and with an extensive literature survey, we were able to design the chemical composition of the steels for this research.

4.1 ALLOY DESIGN

The composition of the steels used in this investigation in weight percent and atomic percent, are shown in Table 4.1. The three steel compositions are designated as Rsteel 1, Rsteel 2 and Rsteel 3. One of the primary objectives of this research is the control and elimination of proeutectoid cementite formation on austenite grain boundaries, therefore, the effect of substitutional solutes on the suppression of cementite formation became of primary interest. Silicon and vanadium were selected as important alloying elements. Silicon has a strong influence on the suppression of cementite. On the other hand, vanadium has been identified as a modifier of grain boundaries. Three different silicon contents and two different vanadium contents in the steels were selected to study their effect on the kinetics of proeutectoid cementite formation.

This study was also focused on studying the influences of different alloying elements on the transformation temperature which has a direct effect on the kinetics of pearlite transformation. The degree of undercooling controls the spacing between the lamellas of cementite. This undercooling gradient has to do with the transformation temperature. Moreover, the content of niobium was varied with the idea to study its influence on the dynamic properties of these steels; three different niobium contents were selected to examine its effect.

Table 4.1 Chemical composition in weight % and (atomic %)

Element	RSteel 1	RSteel 2	RSteel 3
C	0.728 (0.488)	0.797 (0.509)	0.846 (0.585)
Mn	1.012 (0.148)	1.245 (0.174)	1.156 (0.175)
P	0.0026 (0.0006)	0.0061 (0.0015)	0.0075 (0.002)
S	0.0021 (0.0005)	0.0024 (0.0006)	0.0023 (0.0006)
Si	0.821 (0.235)	0.7 (0.191)	0.494 (0.146)
Ni	0.088 (0.012)	0.091 (0.0119)	-
Cr	0.192 (0.029)	0.251 (0.037)	0.249 (0.039)
Mo	0.253 (0.021)	0.255 (0.020)	0.249 (0.022)
V	0.205 (0.0324)	0.177 (0.266)	-
Al	0.0452 (0.0135)	0.0324 (0.0092)	0.0425
Cu	0.094 (0.012)	0.091 (0.011)	0.081 (0.0106)
Nb	0.033 (0.0028)	0.0351 (0.0029)	0.0254 (0.0022)
N	0.0061 (0.0035)	0.0056 (0.0031)	0.0056 (0.0033)

These steels were melted under vacuum conditions and poured into 140 Kg ingots. One half of the ingots was hot rolled to plates of approximately 38.1mm in thickness using standard reheating and rolling conditions and air cooling to room temperature (ACRT).

4.2 MATERIAL PROCESSING

One ingot obtained from each steel was hot rolled to plates approximately 38.1mm in thickness using standard reheating and rolling conditions and ACRT. From these blocks, cylindrical compression specimens were machined. The schematic representation of a standard compression specimen is shown in the Figure 4.1, below. The dimension of a specimen is 12.7mm in diameter by 19.05mm h in height. Prior to the compression tests the specimens were nickel plated to minimize the oxidation of the test specimens during reheating. In addition, to prevent any barreling effects or reduce shear stresses caused by friction, single or double applications of glass based lubricant or a mixture of two types of glass based lubricant called DeltaGlaze® are used based on the hot deformation temperatures and other deformation parameters.

The temperature control is done by inserting a K-type thermocouple from Omega® at the mid-height of the specimen, see Figure 4.2. In addition, a second K-type thermocouple was used to record heating rates, cooling rates or transformation behavior. The cylindrical samples were homogenized at 1200C for 2hr. The hot compression tests were performed in a modified computer-controlled high temperature MTS Model 458 servo hydraulic machine. This system consists of a frame rated at 50 KN. The force is applied by an hydraulic piston at the bottom of the machine which moves upward to produce the deformation under compression. The hydraulic piston controlled by a servo-valve is rated dynamically at 500 KN. The load capacity of the machine is 222.5 KN. All deformations were carried out at a strain rate of 20 s^{-1} . The other deformation parameters, such as amount of deformation (ϵ),

the deformation temperature (T_{def}), and delay time (t) were varied in different ways to obtain the suitable conditions of microstructure and mechanical properties.

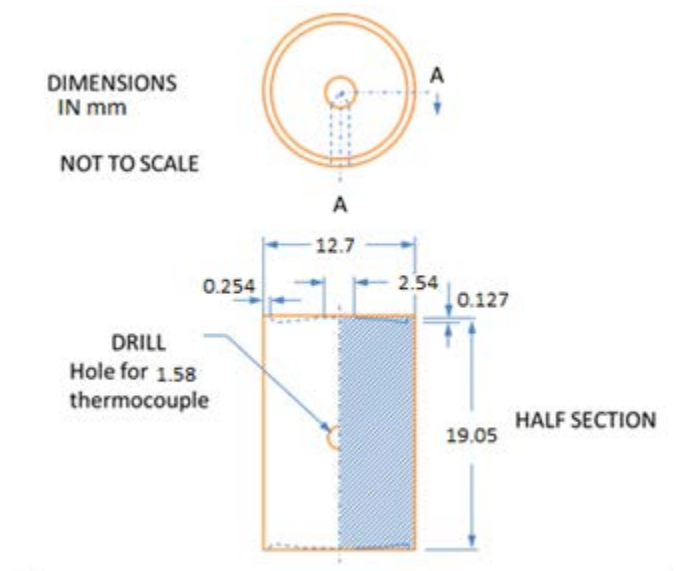


Figure 4.2 Schematic of a standard compression specimen

The schematic description of the hot deformation simulation in these experiments is illustrated in Figure 4.3.

The second ingot of each steel composition was hot rolled on a computer controlled laboratory scale rolling mill with the conditions obtained from the thermomechanical studies. In addition to the hot rolling simulations, this section also includes analysis of the subsequent heat treatments.

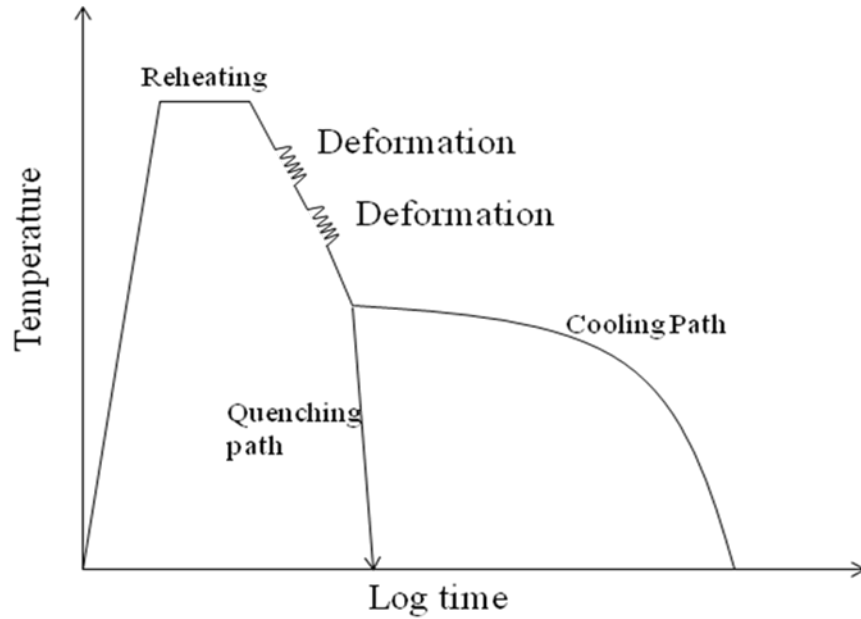


Figure 4.3 Schematic representations of the thermomechanical experiments

4.3 OPTICAL MICROSCOPY

Samples from thirteen current commercial steels and the specimens from the hot rolling experiments were mounted and ground with abrasive paper (320, 400, 800, 1200 and 2400) and polished using alumina (1 μ m and 0.05 μ m). In order to reveal the austenite grain boundaries, the samples were etched with two different chemical agents. First, at room temperature, they were immersed in a 5% HCl distilled water solution for 5seconds. Secondly, at 98 C, samples were immersed in picric acid saturated solution until the grain boundaries were revealed. The use of the HCl solution was intended to eliminate the sensitivity of some grain boundaries. The specimens were then studied under the optical microscope.

Quantitative metallography was performed using the computer controlled BioQuant image analyzer to determine the average prior austenite grain size. At least 150 grains were measured in every sample.

4.4 ELECTRON MICROSCOPY TECHNIQUES

For the analysis of interlamellar spacing as well as the pearlite colony size, the specimens were etched at room temperature using two etchants. First, they were immersed in a 5% HCl distilled water solution for 5 seconds. Then they were etched with a 3% nitric acid ethanol solution until the desired microstructure was revealed. The analysis of these microstructural features was performed in the scanning electron microscopy (SEM) JEOL operated at 10KeV. Quantitative metallography was performed using the computer controlled BioQuant image analyzer to determine the average pearlite colony size. At least 500 interlamellar spacings and 200 colony sizes were measured in every sample. All samples observed by this technique were coated with sputtered palladium.

Analysis of proeutectoid cementite kinetics was also performed in the scanning electron microscope. Samples for this study were first immersed in a 5% HCl distilled water solution for 5 seconds. Then the samples were immersed in 100 ml of saturated picric acid solution and three grams of diiodobenzene sodium sulfonate. The samples immersed in the solution at 98C and were placed in the ultrasonic equipment from 5 to 10 seconds until the proeutectoid cementite was revealed.

Electron back scattering diffraction, (EBSD), analysis was used to provide the information on the crystallographic relationship between the austenite grain boundary and the proeutectoid cementite formation. The samples used for EBSD analysis were cut, ground and polished as described in the optical microscopy section. In addition, the Vibromet 2 vibratory polisher was used for fine polishing. In this case, the polishing time on the Vibromet varied from 5 to 40 minutes. The standard operation procedure of EBSD observation was employed in this part of work. For every scattering process, 15KeV and spot size of 4 were applied. The frame number is always set at 8 and the hexagonal scan mode is used with the step size varying from 0.1 to 0.5 μ m determined by features of interest. The information collected was processed by using OIM data collector software.

4.5 MECHANICAL TESTING

Preliminary to the final mechanical tests, a series of hardness measurements were performed in order to obtain the best combination of microstructure and hardness in terms of chemical composition and volume fraction of proeutectoid cementite. The results of these tests helped to form the criteria under which the steels and treatments were chosen for the subsequent and final evaluation. The hardness testing evaluation of all specimens was performed in accordance with ASTM standard specifications.

With the criteria of hardness and microstructure, the suitable steels were selected and tensile samples were machined. All tensile tests were performed at room temperature using an Instron tensile machine with a cross head speed of 0.2 cm/min. An MTS 24.5mm gauge length extensometer was attached to the tensile samples. The extensometer is capable of measuring

deflection up to 50 % from the original length. The tensile test evaluation from samples hot rolled in a laboratory mill were performed in accordance with ASTM standard E-517 using the MTS 880 servohydraulic machine.

The samples which exhibited the highest yield strength and the largest elongation on the tensile test, were selected to perform the fracture toughness evaluation. The fracture toughness, parameters K_Q and/or K_{IC} , were evaluated in samples obtained from material hot rolled on a laboratory mill. These tests were conducted by a certified laboratory (Bodycote).

4.6 WEAR TEST

The wear test was carried out on the disk machine (Figure 4.4). A Pin-on-disc tribometer was used to perform the sliding wear testing. The tribometer consists of a spine rotational base where the disk is held and a pin contacts the disk with an established load. The pin-on-disk experiments were carried out in several numbers of cycles (50, 100, 1000, 5000 and 10000). The disk used was 65mm in diameter and 6mm thick. The pins used for this test were made from tool steel quenched and tempered with a hardness value of $68 \pm 1\text{HRC}$, the radius of the pin was 6.3mm, with a length of 20.7mm. Figure 4.5 shows the configuration and sizes of the samples as well as the wear testing representation.



Figure 4.4 Wear test machine

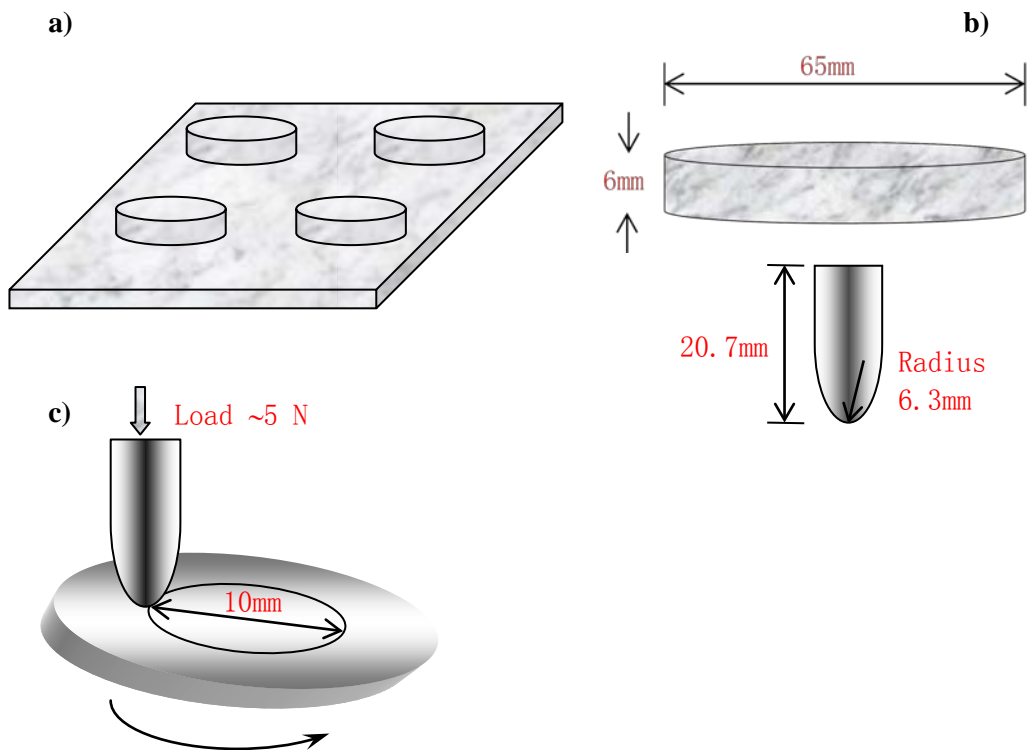


Figure 4.5 a) Sampling from the rolled material b) Configuration and dimensions of disk and pin

c) Schematic representation of wear testing

The contact load used in these tests was the highest load allowed in the tribometer, 500gf (~5N). The rotational velocity used was 10 rpm. The tribometer registers the normal and friction forces. The diameter of the track described during the wear test was 10mm for all cycles. Disks and pins were ultrasonically cleaned for 20min in acetone. The disks were dried in air. After the acetone cleaning, the disks and pins were held for 24hr before the wear test in desiccators at room temperature. In order to avoid any type of contamination, the entire manipulation of disks and pins was done with pincers. A new pin was used for each cycle. The constant force applied to the pin produced a Hertzian force equivalent to 0.94 GPa. The formula used to calculate the Hertzian force is:

$$P_o = \left(\frac{6WE^{*2}}{\pi^3 R^2} \right)^{\frac{1}{3}} = \left(\frac{6(10N)(144.76 \times 10^9 Pa)^2}{\pi^3 (0.8 \times 10^{-3} m)^2} \right)^{\frac{1}{3}} \quad (4.1)$$

where W is the load applied in the tribometer, R is the radius of the Pin, E^* is called effective Young Modulus and it is calculated by:

$$\frac{1}{E^*} = \frac{1-\nu_1^2}{E_1} + \frac{1-\nu_2^2}{E_2} \quad (4.2)$$

where: E_1 and E_2 are the Young modulus of the pin and the disk material, respectively, and ν_1 and ν_2 are Poisson's ratio of the pin and the disk material.

4.7 ISOTHERMAL TRANSFORMATION STUDIES

Samples from different steels were cut in thin slides to a thickness of 1mm and were attached to a k-type thermocouple. The samples attached to the thermocouple were heated in a controlled argon atmosphere furnace up to 1050C (around 100C above A_{cm}). The samples were heated for 2 minutes. After that, the samples were quickly transferred to an adjacent box furnace where the samples were subsequently quenched into a molten mixture of barium chloride and sodium chloride salt (in a volume ratio of 70:30) at temperatures ranging from 850C to 550C, for times ranging from 5 seconds to 30 minutes. The temperature of the furnace was controlled to within $\pm 5C$ and the salt bath was controlled to within $\pm 2C$. After the isothermal reaction in the salt bath, the samples were quenched into ice water. A schematic representation of this process is shown in Figure 4.6.

After heat treatment, the samples were cut and mounted facing the transverse section and it were prepared for optical microscopy by the standard grinding and polishing procedures.

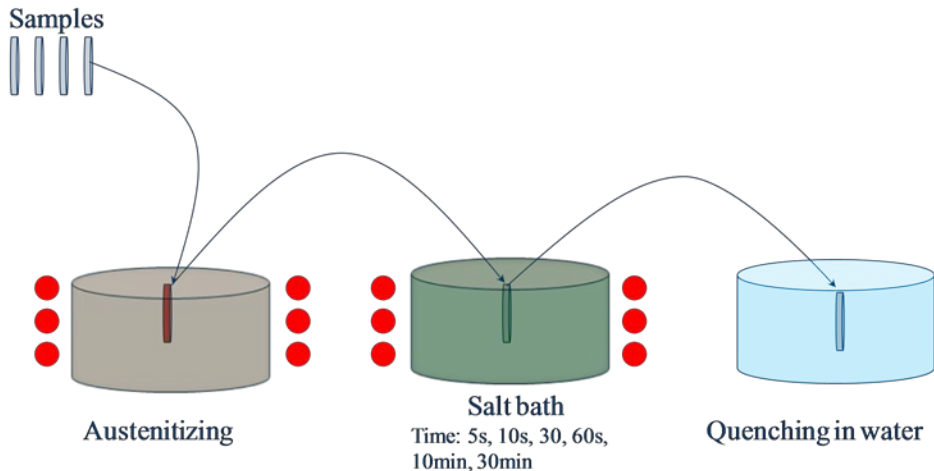


Figure 4.6 Schematic representations of isothermal transformation studies

5.0 RESULTS

5.1 MICROSTRUCTURAL ASSESSMENT OF COMMERCIAL RAIL STEELS

A systematic microstructural analysis of the 13 commercial rail samples received from different companies was performed. Samples from the 13 different steels were cut, mounted, polished and etched for microstructural examination using standard metallographic techniques. Measurements of interlamellar spacing as well as the pearlite colony size and prior austenite grains size were made with the aid of a computer controlled automated image analysis system. Optical microscopy (OM) and scanning electron microscopy (SEM) were used in this analysis. The SEM results showing micrographs of the pearlitic microstructure and interlamellar spacing for various steels investigated are shown in Figure 5.1. The measurements of interlamellar spacing were performed on these micrographs. The analysis of pearlite colony size was also performed using multiple SEM micrographs. Examples of those micrographs, delineating the pearlite colony from different steels, are shown in Figure 5.2. Figure 5.3 shows optical micrographs of austenite grains from different commercial steels. The measurement of all microstructural features was performed with the help of an automated BioQuant NOVA image analysis as stated in the experimental procedure section. The results of interlamellar spacing measurements, pearlite

colony size and austenite grain size from three different locations of the rail are summarized in Table 5.1.

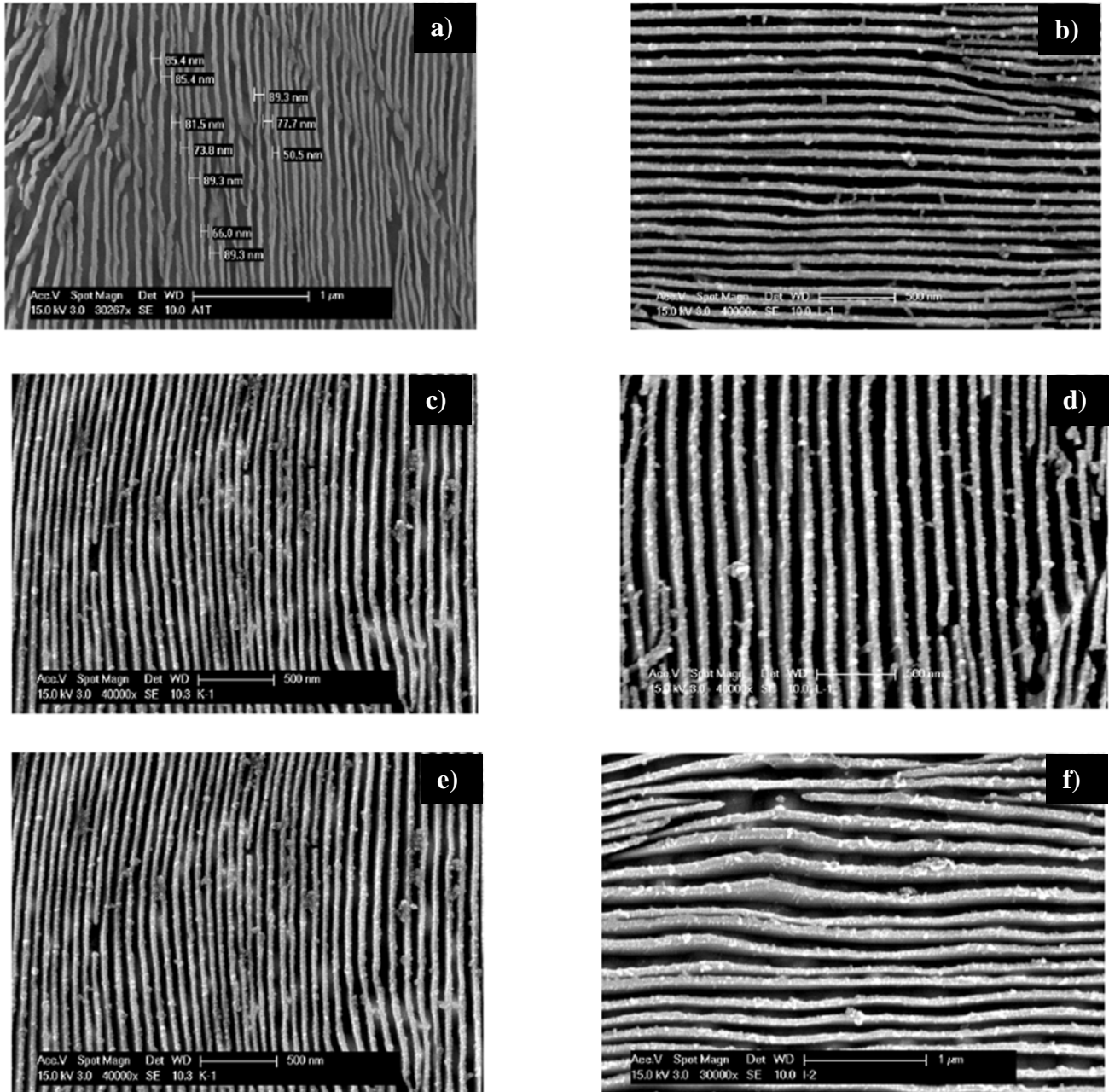


Figure 5.1 SEM micrographs showing the interlamellar spacing of some of the commercial steels
 a) Steel A, b) Steel B), c) Steel K, d) Steel L, e) Steel D, and e) Steel I

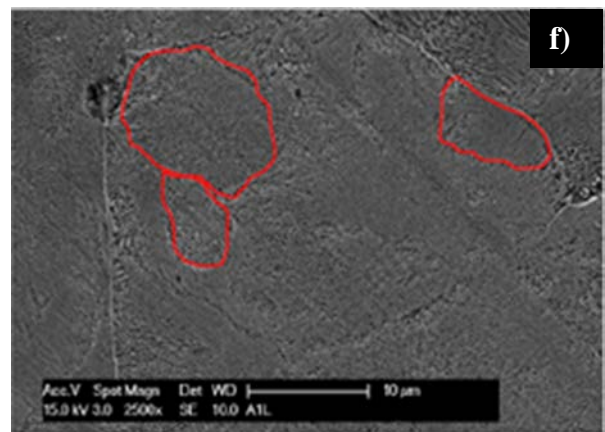
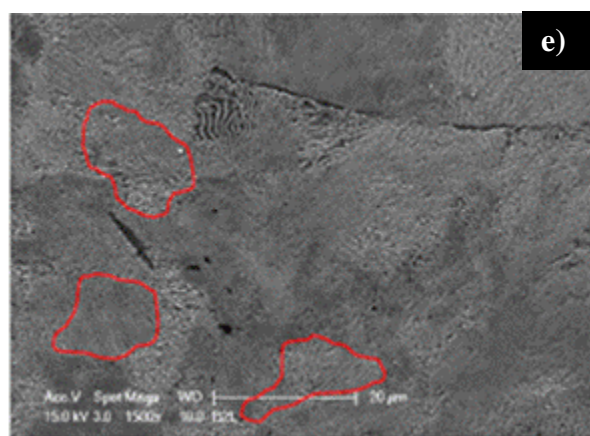
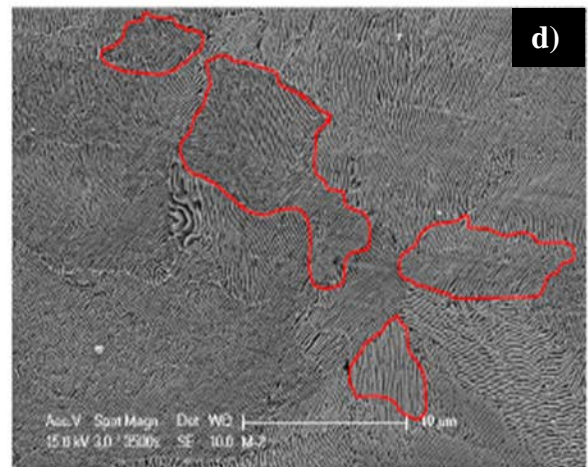
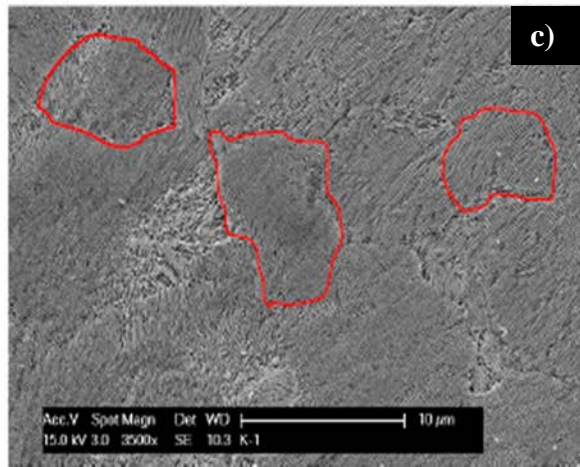
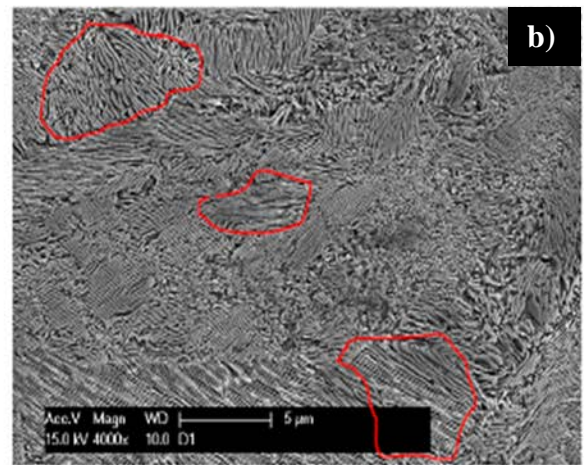
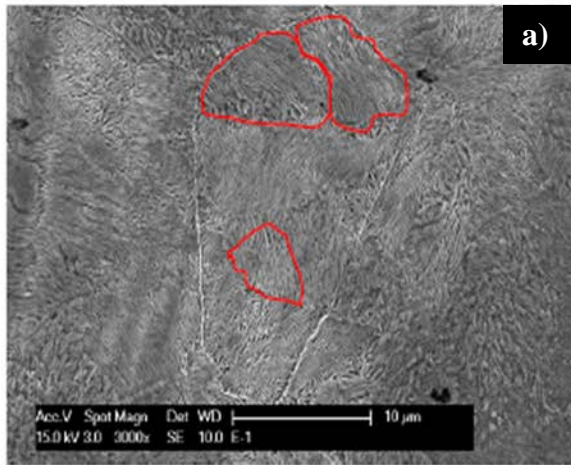


Figure 5.2 SEM micrographs showing the pearlite colony of some of the commercial steels

a) Steel E, b) Steel D), c) Steel K, d) Steel M, e) Steel A, and e) Steel B

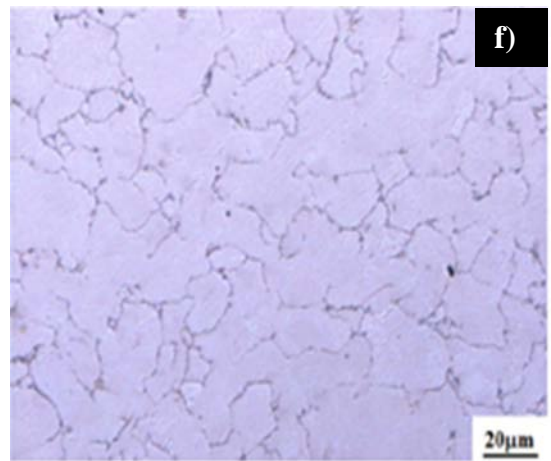
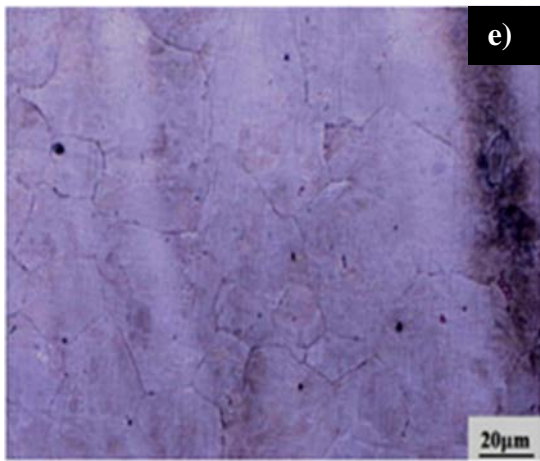
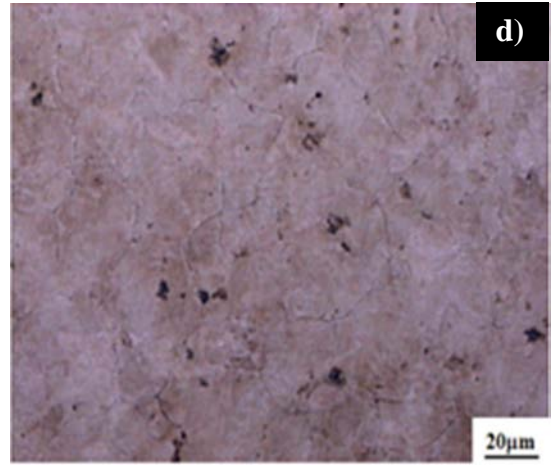
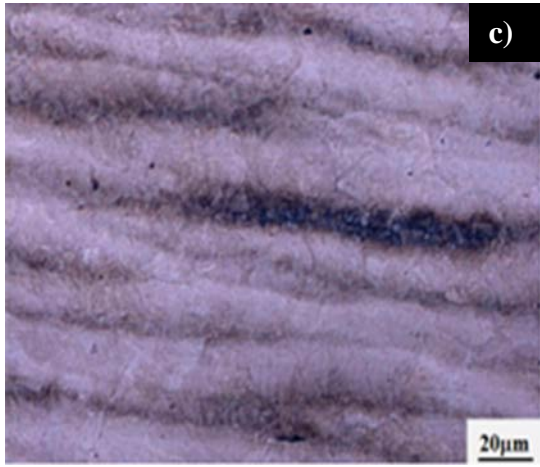
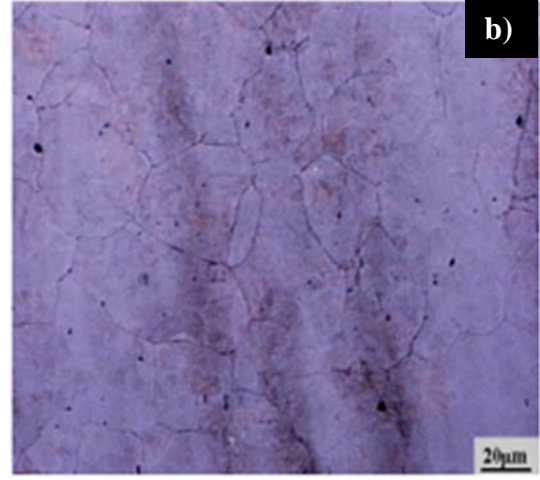
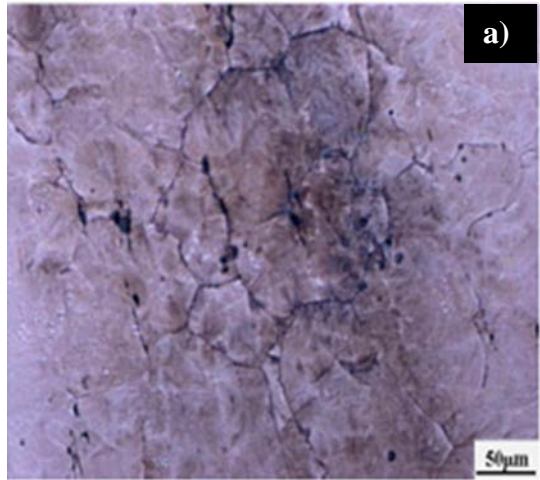


Figure 5.3 Optical micrographs showing the austenite grain boundaries of some of the commercial steels. a) Steel A, b) Steel D), c) Steel E, d) Steel B, e) Steel M, and e) Steel C

Table 5.1 Values of interlamellar spacing, pearlite colony size and prior austenite grain size from the commercial steels

Internal ID	Interlamellar Spacing [μm]			Pearlite Colony [μm]			Prior Austenite Grain [μm]		
	Head	Web	Foot	Head	Web	Foot	Head	Web	Foot
A	0.1001	0.15	0.154	2.6	3.3	3.2	67.9	74.4	21.3
B	0.101	0.129	0.135	1.9	3.6	2.4	59.4	32.1	27.3
C	0.088	0.153	0.197	2.1	3.5	4.2	34.7	64.6	21
D	0.094	0.146	0.191	2.1	4.6	3.9	34.7	27.2	28.5
E	0.089	0.145	0.163	2.9	3.9	3.7	28.8	32.1	26.3
F	0.117	0.12	0.116	2.9	3.6	3.1	23.3	32	22.1
G	0.07	0.107	0.132	2.8	4.4	3.2	24.8	27.9	22.2
H	0.098	0.133	0.145	2.9	3.9	2.9	25.9	47.8	23.9
I	0.088	0.148	0.178	2.8	2.7	3.9	58.6	61.5	20.5
J	0.078	0.129	0.175	2.4	2.6	4.3	32.4	60.8	27.3
K	0.08	0.177	0.148	2.5	4.2	3.8	64.3	73.1	28.3
L	0.099	0.125	0.148	3.0	3.9	3.3	49.8	34.3	23.2
M	0.1001	0.13	0.152	2.9	2.9	3.5	56.3	66.3	23.1

5.1.1 Yield strength and its relationship with microstructural features

5.1.1.1 Yield Strength vs Interlamellar Spacing

Tensile tests were conducted from several of the commercial steels used in this thesis. The yield strength values and the interlamellar spacing from several steels were related. See Figure 5.4. It was found that the smaller the distance between carbides plates the higher the yield strength of the steel. Similar results were observed by Embury and Fisher [88] in hyper-eutectoid steels. The yield strength of the commercial steels was found to vary as the inverse square root of the carbide plate distance, (λ). Figure 5.4 shows the variation of yield strength with inverse square root of interlamellar spacing of some commercial steels.

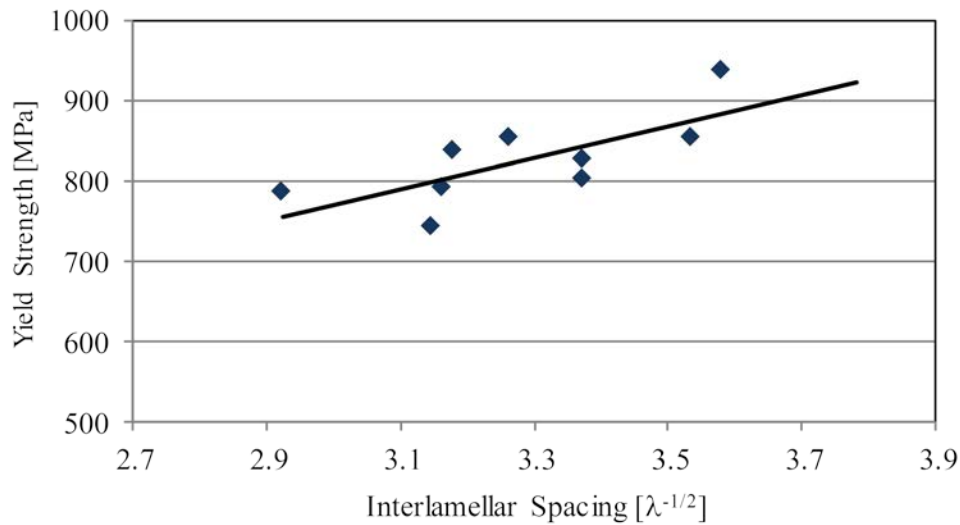


Figure 5.4 Yield strength variations with respect to interlamellar spacing from different commercial steels

The straight line in Figure 5.4 indicates the trend line of the yield strength, which seems to follow the behavior described by the Hall Petch equation (2.5). The Hall Petch equation

asserts a straight line relationship between the yield strength and the inverse square root of the interlamellar spacing. As expected, the yield strength increased as the interlamellar spacing decreased.

5.1.1.2 Yield Strength vs Pearlite Colony and Prior Austenite Grain Size

Hysak and Bernstein, working with steels containing 0.81%C [81], found that not only the interlamellar spacing has an important role in yield strength, but also the pearlite colony size and the prior austenite grain size. This observation is not surprising since it is well known that pearlite nodules usually nucleate on austenite grain boundaries and grow at a roughly constant radial velocity into the surrounding austenite grains. From Table 5.1 is clear that the pearlite colony size is slightly smaller at the head of the rail samples than at the web or base of the rail.

The results illustrated in Table 5.1 were used to calculate the contributions of the pearlite colony size according to the equation by Taleff et al., [79]:

$$\sigma_y = (\sigma_o)_{ss} + 145(P)^{-\frac{1}{2}} + 460 (\lambda)^{-\frac{1}{2}} \quad (5.1)$$

In this case, it was considered that the contribution to the strength due to the interlamellar spacing was constant and only the contribution to the strength due to the pearlite colony size was taken into account. These results are plotted in Figure 5.5. The results in this figure clearly show that by decreasing the pearlite colony size the yield strength can be increased. This behavior indicates the importance of the prior austenite grain size prior to its decomposition. Pearlite colony size is only dependent on the prior austenite grain size while λ is dependent on the cooling rate and transformation temperature.

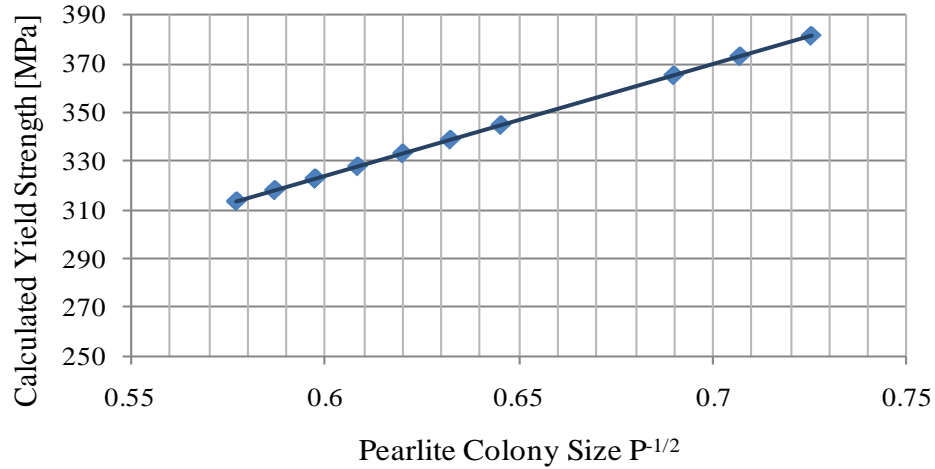


Figure 5.5 Pearlite colony size vs yield strength calculated from equation 5.1

From the results shown in Table 5.1 and the yield strength measured in the commercial steels, Figure 5.6 was plotted. The results did not show any significant increase on the strength with finer austenite grain size. However, this behavior can be attributed to the very small variation in austenite grain size exhibited by the steels investigated in this microstructural assessment.

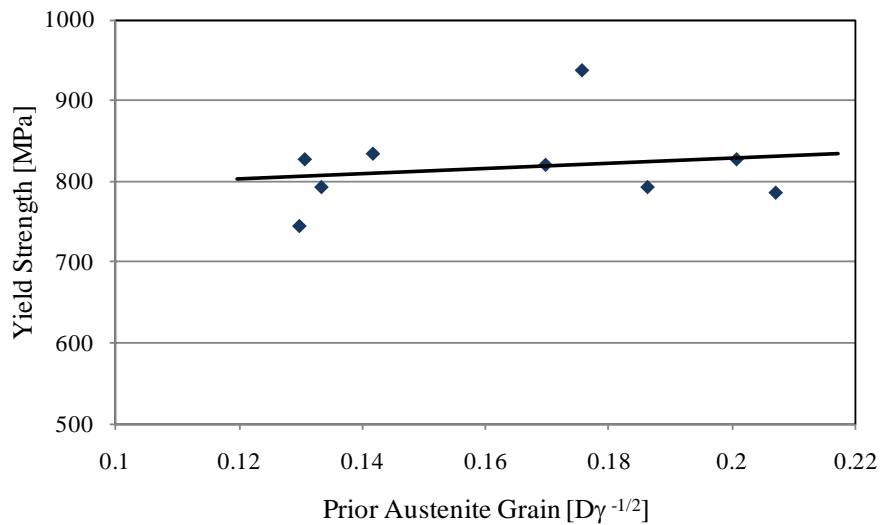


Figure 5.6 Relationship between the prior austenite grain size and the yield strength of commercial steels

The results from Figure 5.6 also seem to support the view that the majority of the current steels used in the fabrication of rails exhibit very similar microstructural conditions of austenite prior to transformation. The implication of these suggests that most of the commercial rail steels observed in this study appear to be processed in a very similar fashion.

5.1.2 Non-Metallic Inclusions

Analysis of the non-metallic inclusions was performed on all 13 commercial steels. Optical (OM) and scanning electron (SEM) microscopy were used for this analysis. The presence of non-metallic inclusions, primarily oxides and sulfides, has been linked to lowering the fatigue life or initiating rolling contact fatigue, (RCF), particularly in older and lower strength rail steels. Modern higher strength rail steels have a tighter control of this type, volume fraction and shape of non-metallic inclusions. The higher cleanliness exhibited by these steels have increased the fatigue resistance of rail steels. Steif and Iyenger [89] also studied the effect of inclusion distribution on the initiation of defects and concluded that by reducing the clustering of non-metallic inclusions results in lower tendencies to nucleation and propagation of transverse defects, in rail steels under service conditions which often occurs near inclusions. Figure 5.7 shows OM and SEM micrographs of non-metallic inclusions present in commercial steels. The quantitative assessment of the non-metallic inclusions observed and measured in the steels investigated is presented in Table 5.2. In addition, this table shows the proeutectoid cementite measured for each commercial steel.

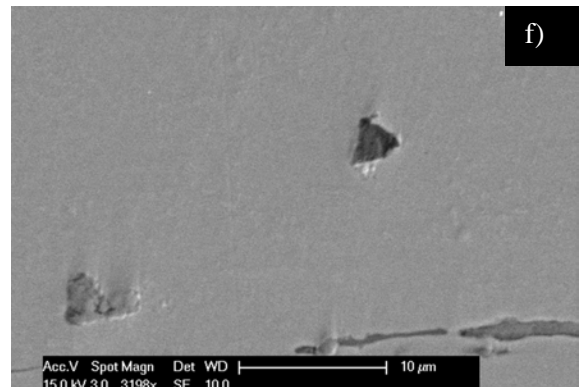
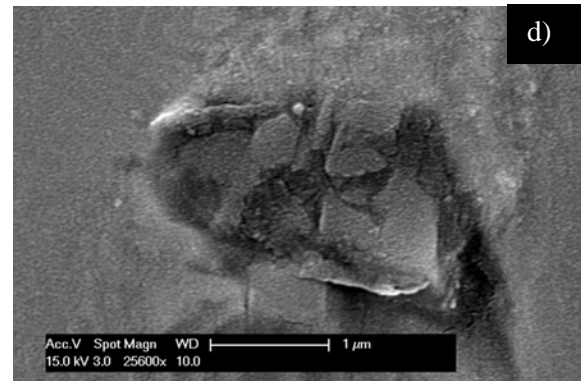
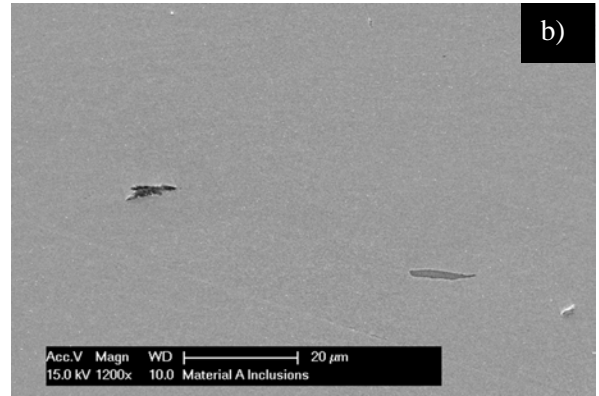
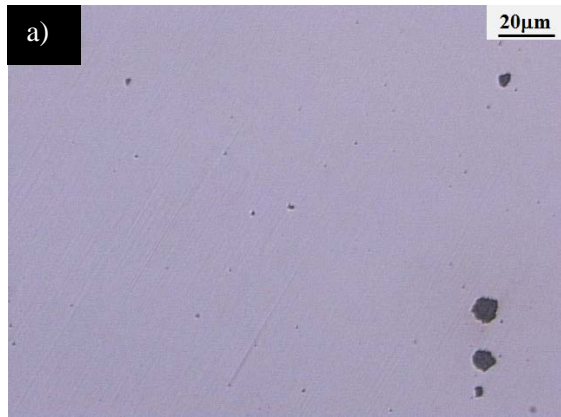


Figure 5.7 Optical micrographs of non-metallic inclusions of commercial steels a) Steel F, c) Steel E, and e) Steel A, SEM micrograph from the same area b) Steel F), d) Steel E and e) Steel A

Table 5.2 Summary of the values of volume fraction of non-metallic inclusions and the measured proeutectoid cementite in commercial steels

ID	MnS	Al₂O₃	SiC	TiN, VN	CaCO₃, MgCO₃	Mesured Proeutectoid cementite V_f
A	0.005272	0.000803	0.000021	-	-	1.02
B	0.000928	0.00058	-	-	-	1.98
C	0.00304	0.00206	0.000019	0.000071	-	1.26
D	0.01655	0.00187	0.00001	0.00028	-	2.98
E	0.00112	0.000174	0.000017	-	-	3.05
F	0.000861	0.000448	-	-	0.000098	1.11
G	0.00088	0.000274	0.00001	0.000015	-	2.65
H	0.00091	0.000178	-	0.000013	-	0.99
I	0.00087	0.000273	0.000033	0.000026	-	1.25
J	0.00022	0.00068	-	-	-	2.25
K	0.0131	0.003018	0.000011	0.00013	-	1.99
L	0.00109	0.000194	-	0.000029	0.000032	3.53
M	0.00097	0.00017	0.000024	-	-	2.71

5.1.3 Proeutectoid Cementite

The presence of the proeutectoid cementite phase was observed in several of the commercial steels. The presence of this phase was detected along the prior austenite grain boundaries, as is shown in Figure 5.8. The proeutectoid phase is the cementite which forms directly from the high temperature austenite phase below the eutectoid temperature in a metastable fashion. From the point of view of technology, the presence of this phase is undesirable due to its brittle nature, particularly if it forms continuously along the austenite grain boundaries. It has been found as a

source of embrittlement [15]. The volume fraction of the proeutectoid cementite of commercial steels was measured by metallographic techniques. The results of this evaluation are shown in Table 5.2.

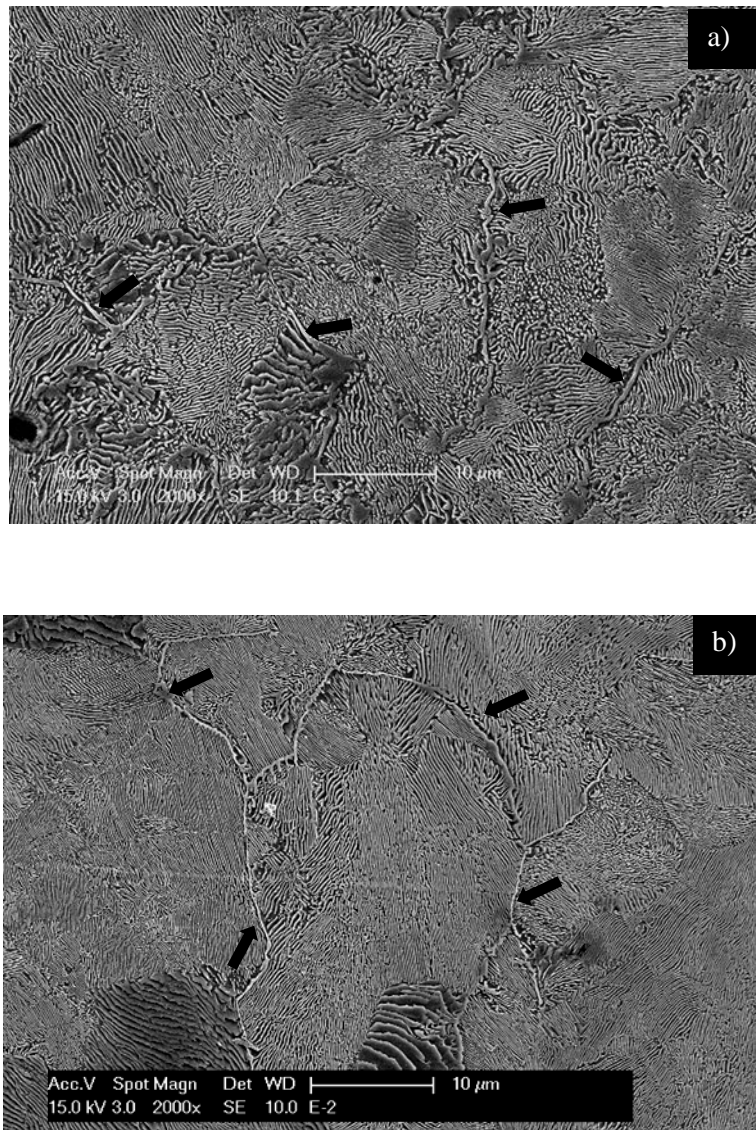


Figure 5.8 Scanning electron micrographs of some commercial steels. Arrows show the presence of the proeutectoid phase a) Steel D and b) Steel M

5.2 THERMOMECHANICAL EXPERIMENTS

The understanding of the microstructural state of the austenite prior to any hot deformation studies is of primary importance. The state of the austenite prior to transformation plays both a very important role on the morphology of the pearlite and the formation of proeutectoid cementite by controlling the transformation temperatures. Therefore, a series of austenite coarsening studies were performed. Samples from each laboratory heat, previously encapsulated in quartz tubes, were heated at different temperatures from 950 to 1250C in a box furnace. In accordance with the results, different temperatures were selected to develop similar austenite grain size. Table 5.3 shows the conditions used in this heat treatment.

Table 5.3 Prior austenite grain size and reheating temperatures used in each steel

	T reheat [C]	Austenite grain size [μm]
Rsteel1	1160	208 ± 11
Rsteel2	1200	211 ± 13
Rsteel3	1210	215 ± 9

The reheating temperature to achieve very similar austenite grain size prior to any subsequent deformation was different for the steels and is strongly related to their chemical composition. This temperature was used to reheat the compression samples from the experimental steels prior to any subsequent deformation.

The general thermomechanical procedure, illustrated in Figure 4.1, indicates the following: a) reheating of the compression sample to a prescribed temperature and held for 2

min, b) lower temperature to the first deformation temperature followed by one single hit at the strain rate of 20 sec^{-1} , c) the second deformation was performed below the recrystallization temperature of austenite using the previous strain rate, d) after the second deformation, one sample of each steel was quenched in ice water to verify the austenite grain size. Prior to transformation, other samples were cooled at 5C/s at different transformation temperatures and held for different times until the full transformation of the required final microstructure was obtained. The transformation temperatures were different and depended on the state of the austenite prior to transformation and the overall chemical composition of the steel. The transformation start temperatures used in this investigation were determined theoretically for a given steel composition and austenite grain size prior to transformation using a computational thermodynamic, JMatPro 4.0, program.

5.2.1 Rsteel1

For Rsteel1, the reheating temperature was 1160C for two minutes. The first deformation was 50% (engineering strain) at 1100C , and the second deformation was, again, 50% (engineering strain) at 850C . After the second deformation, the sample was cooled at 5C/s to room temperature. Even though the sample had the required hardness value (we established a threshold hardness value of 38HRC, which, in experience, would assure the appropriate mechanical properties), the microstructure generated after this experiment was not pearlite.

With the idea to generate the full pearlite microstructure, and using the same values of deformation, two samples after the second deformation were continuously cooled at 0.1C/s and 1C/s . The sample continuously cooled at 0.1C/s was fully transformed to pearlite; however, the

interlamellar spacing of this sample was too large (250 μ m). Therefore, the hardness was below the required threshold hardness value. On the other hand, the sample cooled at 1C/s was not fully transformed to pearlite but the hardness was above the threshold value.

A different approach was tried; isothermal transformation at a prescribed temperature. Samples were deformed at the same temperatures and the same amounts of deformation, cooled at 5C/s up to 550C and held for different times. The hold times were 20 and 100 minutes. However, the microstructure developed was not fully pearlitic. The hardness values from each sample were above the threshold value. Based on the TTT diagram calculated from the JMatPro 4.0 program (see Figure 5.9), a different holding temperature, 600C was chosen. Two samples were held at this temperature for 10 and 20 minutes. Both samples were fully transformed to pearlite; however, only the sample held for 20 min had a hardness value above the required threshold. Figure 5.10 illustrates the hardness and the microstructure of the thermomechanical treatments performed.

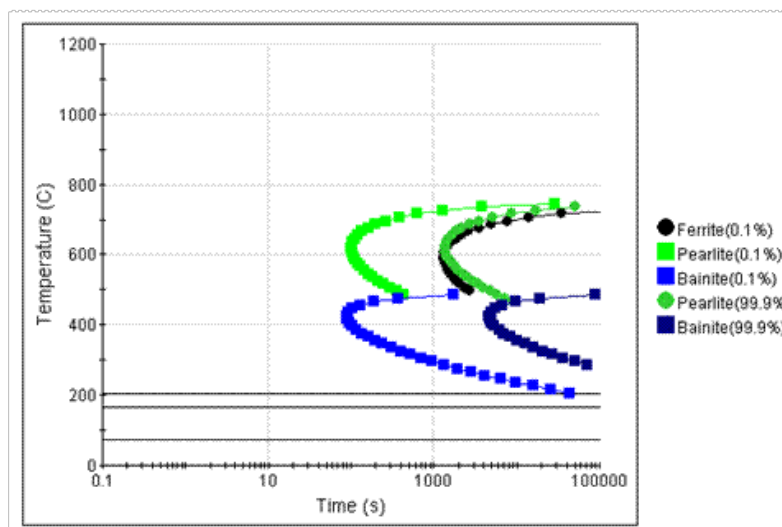


Figure 5.9 TTT diagram calculated by the JMatPro 4.0 program from the chemical composition on the Rsteel 1

Table 5.4 Thermomechanical processing details, hardness and microstructures generated

TMP	Continuously Cooling [C/s]	Isothermal Path [C]	Type of Microstructure	Hardness [HRC]
1	Quenched	Quenched	Martensitic	53.3 ± 1.3
2	5	-	Not fully pearlitic	52 ± 2.2
3	-	550/ 20min	Not fully pearlitic	54 ± 1.7
4	-	550/ 100min	Not fully pearlitic	53 ± 2.5
5	0.01	-	Fully pearlitic	17.6 ± 0.8
6	1	-	Not fully pearlitic	40.2 ± 0.9
7	-	600/10min	Fully pearlitic	32.6 ± 1.3
8	-	600/20min	Fully pearlitic	39.6 ± 2.1

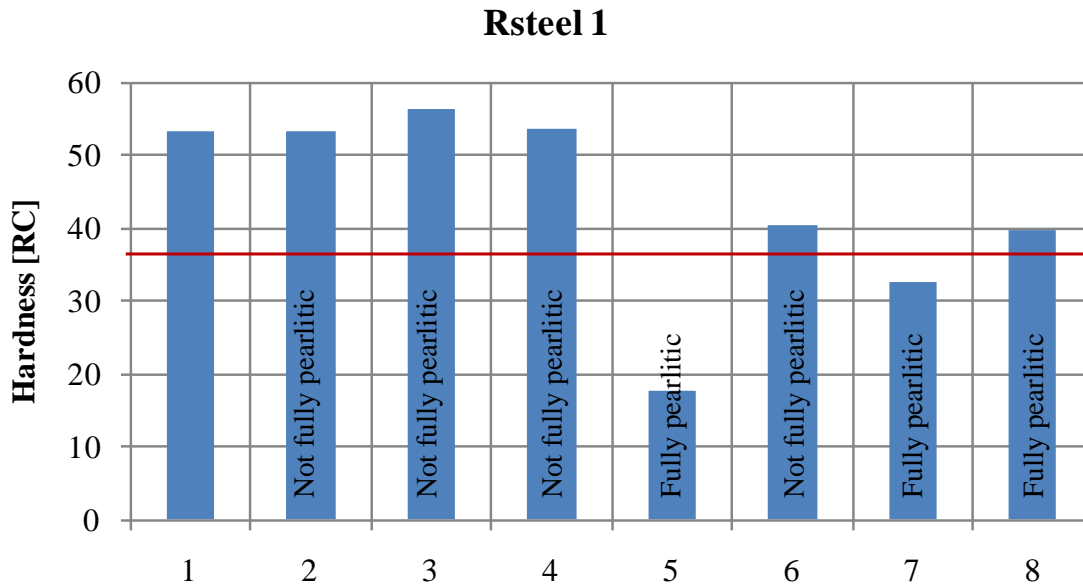


Figure 5.10 Results of hardness and microstructure of rail steel 1

Examples of the microstructure developed during thermomechanical processing experiments are shown in Appendix A. Figure 5.11 shows the final microstructure obtained with the thermomechanical processing experiment number 8.

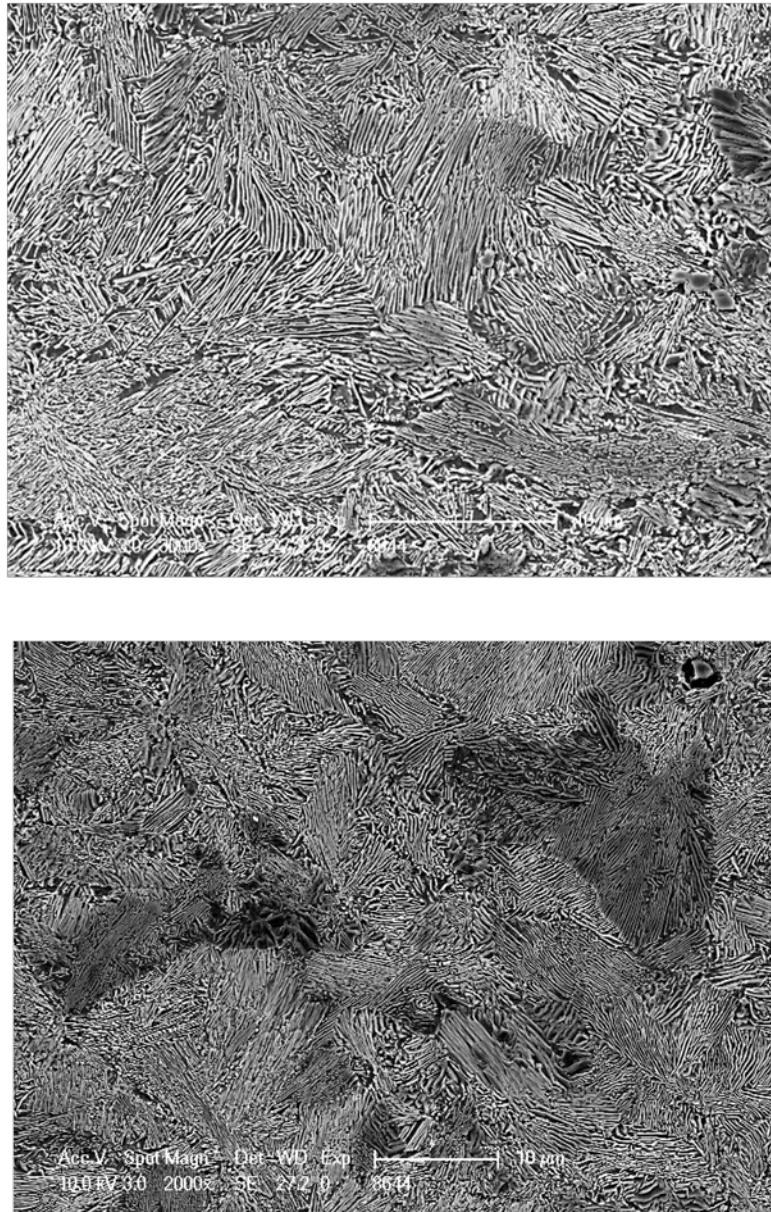


Figure 5.11 Scanning electron micrograph of Rsteel1 developed throughout the thermomechanical experiment number 8. Fully pearlitic microstructure is shown

5.2.2 Rsteel2

The reheating temperature for Rsteel2 was 1200C for 2 min. The amount of deformation in the first compression process was 50% at 1100C; then, the sample was cooled to 880C. The second deformation was also 50%. As in other steels, one sample was quenched right after the second deformation, in order to evaluate the austenite grain size. Another sample deformed under the same conditions was continuously cooled at a rate of 5C/s up to room temperature. The hardness obtained from this TMP was 52.3 HRC, this is about 14HRC above the hardness threshold; however, the microstructure developed was not fully pearlitic. Examples of all microstructures are shown in Appendix A.

As in Rsteel1, the temperature chosen for the isothermal paths were based on the TTT diagram calculated with the JMatPro 4.0 program. Figure 5.12 shows this TTT diagram.

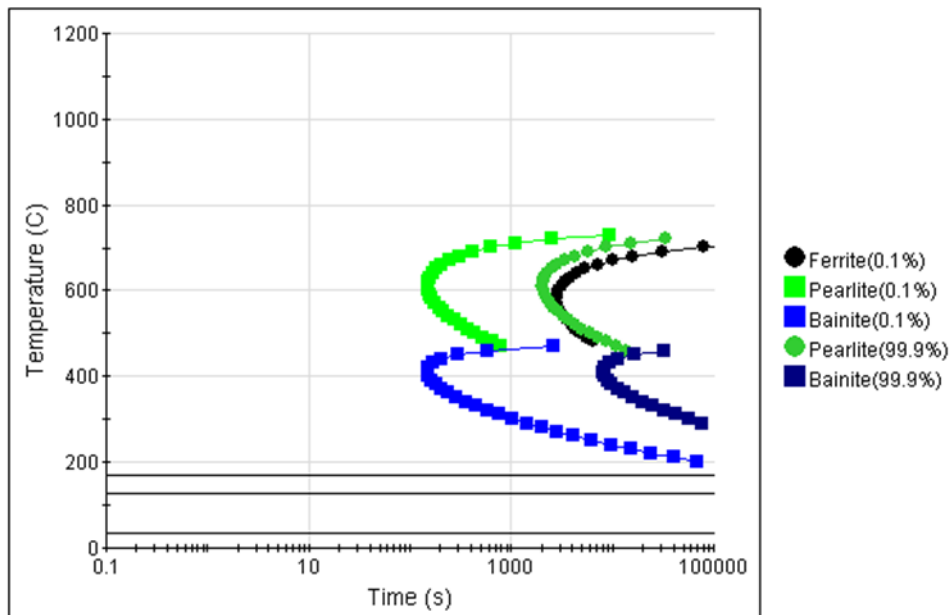


Figure 5.12 TTT diagram calculated on JMatPro program from Rsteel2 chemical composition

In order to satisfy the requirements of hardness and microstructure, isothermal paths were also tried. After the second deformation, the sample was cooled at 5C/s to 550C and held for two different times, 20 and 100 minutes. These samples developed fully pearlitic microstructure. The hardness of the sample held for 20minutes was 43.3HRC and the hardness for the sample held 100 minutes was 39.33HRC. Then the hardness of both isothermal paths was above the hardness threshold. Even though these samples met the hardness and microstructural requirements, we investigated different isothermal temperatures.

One sample was deformed under the same conditions as those of the previous samples, but right after the second deformation, it was cooled at 10C/s to 500C and held for 20min. The microstructure developed was not completely pearlitic. However, the hardness obtained was above the threshold, 46.2HRC. A different approach was tried; increasing the amount of the second deformation from 50% to 70%. After the second deformation (at 880C), the sample was cooled to 500C at 10C/s and held for 20min. Nevertheless, the microstructure developed was not fully pearlitic. Table 5.5 summarizes the TMP conditions, microstructure and hardness developed in these experiments. Figure 5.13 also shows, graphically, the resulting hardness and microstructure of the thermomechanical treatment performed on Rsteel2.

Table 5.5 Thermomechanical processing details, hardness and microstructure generated

TMP	Second Deformation [%]	Continuously Cooling [C/s]	Isothermal Path [C]	Type of Microstructure	Hardness [HRC]
1	50	Quenched	Quenched	Martensitic	63 ±0.5
2	50	5	-	Not fully pearlitic	52.3 ± 1.4
3	50	-	550 / 20min	Fully pearlitic	43.3 ±0.8
4	50	-	550 / 100min	Fully pearlitic	39.3 ± 0.6
5	70	10 to 500C	500 / 20min	Not fully pearlitic	46.2 ± 1.3
6	70	5 to 500C	500 / 20min	Not fully pearlitic	37.6 ± 1.6

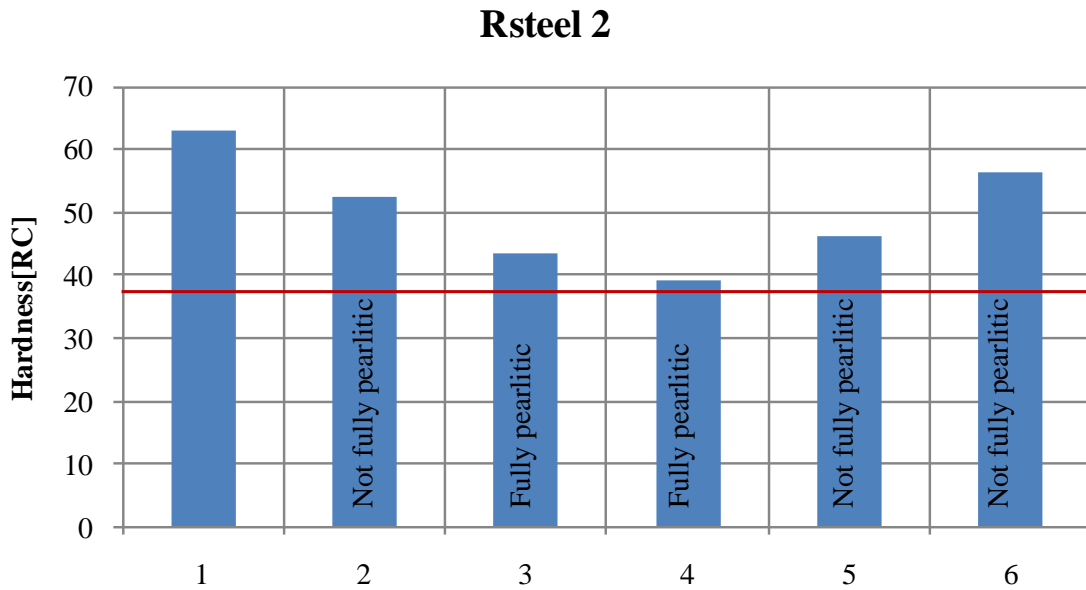


Figure 5.13 Results of hardness and microstructure of Rsteel2

Examples of the microstructure of the samples that met, successfully, the requirements of the hardness and microstructure, are shown in Figure 5.14. Even though they are fully pearlitic microstructures, the type of pearlite is known as divorce pearlite.

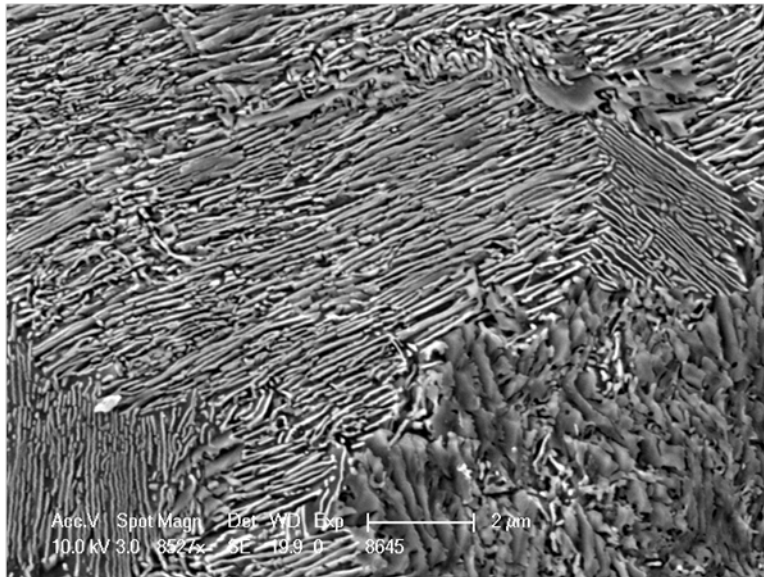
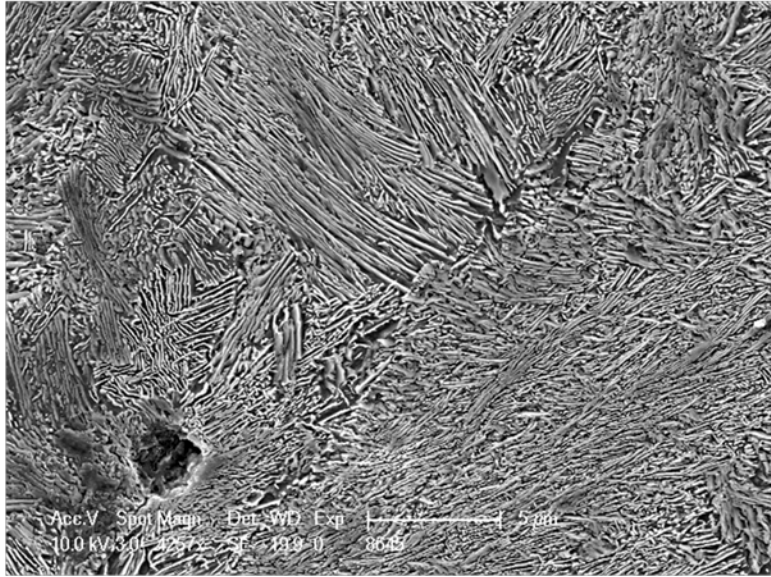


Figure 5.14 Scanning electron micrograph of Rsteel2 developed throughout the thermomechanical experiment number 3

5.2.3 Rsteel3

The Rsteel3, the one which has the higher carbon content, was primarily reheated at 1200 C and held for 2min. The sample was cooled to 1150C at which the first deformation, 50%, was performed. Secondly, the sample was cooled from 1150 to 850C at a rate of 5C/s and the second deformation of 50% (engineering strain), was performed. Once the second deformation was completed, the sample was continuously cooled at a cooling rate of 5C/s until room temperature. This sample did not develop a fully pearlitic microstructure, however, the hardness reached by the sample was above the threshold. Another sample deformed under the same conditions was continuously cooled at 0.01C/s, developing a fully pearlitic microstructure with a coarse interlamellar spacing. This coarse interlamellar spacing yielded a lower hardness value than the threshold (38HRC). As in the case of Rsteel1 and Rsteel2, an isothermal approach was also attempted.

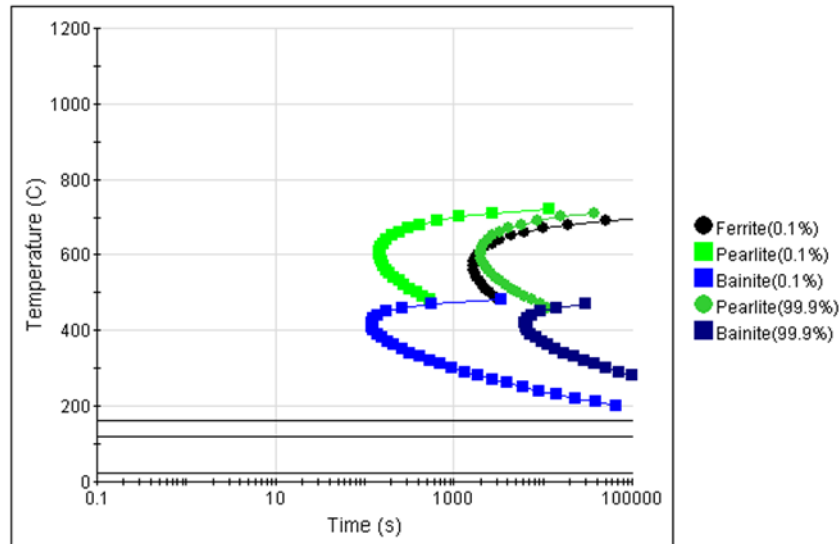


Figure 5.15 TTT diagram calculated by the JMatPro program from the chemical composition of the Rsteel3

Based on the chemical composition, and using the JMatPro 4.0 program, the TTT diagram was calculated in order to have an indication of what would be the isothermal path temperatures. Figure 5.15 shows the TTT diagram calculated with the JMatPro program. Another sample was deformed under the same conditions as those of the previous samples (50% at 1200C and 50% at 850). After that, the sample was cooled at a rate of 5C/s to 550C and held for 20 and 100minutes. Each sample was cut in the middle and mounted facing the transverse section. Both samples developed a fully pearlitic microstructure. The hardness reached by the sample held for 20min was 37.9 HRC and the hardness of the sample held for 100min was 36.1HRC. Scanning electron micrographs of all the microstructures are shown in Appendix A.

Regarding the hardness results, another isothermal temperature was selected. The sample was annealed at 1200C for 2min and then it was deformed 50% at 1150 C. A second deformation of 50% was performed at 850 and cooled at a rate of 10C/s to 500C. Then the sample was held for 40 min, and then cooled in air to room temperature. The hardness of this sample was 33.6 HRC, and the microstructure developed was not fully pearlitic (see Appendix A). Another sample was tested with the same isothermal path but with different deformation conditions. The new sample was deformed initially 50% at 1150C and cooled to 850C and deformed 70% (engineering strain). After the second deformation, the sample was cooled at a rate of 5C/s to 500C and held for 40minutes. Unfortunately, the microstructure developed was not fully pearlitic and the hardness did not reach the threshold value.

The fact that the microstructure developed during the 500C isothermal path was not fully pearlitic gave us the idea to increase the isothermal temperature path. Therefore, another sample

was tested. The sample was reheated at 1200C for 2 min, then deformed 50% at 1150C, cooled to 850C and deformed 70%. After that, the sample was cooled at 5C/s to 600C and held for 15minutes. The microstructure generated was fully pearlitic; however, the hardness was only 28HRC.

One more attempt was performed. In this case, with an isothermal temperature of 550C. The sample was deformed 50% at 1150 C and 70% at 850C; cooled at 10C/s to 550C and held for 20minutes. After that, the sample was cooled in air to room temperature. Finally, the microstructure was fully pearlitic and the hardness was 39.5HRC, reaching the threshold value. Table 5.6 summarizes the thermomechanical processing details and the hardness obtained for each sample. Figure 5.16 shows the hardness and the microstructure developed in each TMP experiment.

Table 5.6 Thermomechanical processing details, hardness and microstructure generated for Rsteel3

TMP	Second Deformation [%]	Continuously Cooling [C/s]	Isothermal Path [C]	Type of Microstructure	Hardness [HRC]
1	50	Quenched	Quenched	Martensitic	52.6 ± 0.6
2	50	5	-	Not fully pearlitic	52 ± 2.1
3	50	5 to 550C	550 / 20min	Fully pearlitic	37.8 ± 0.9
4	50	5 to 550C	550 / 100min	Fully pearlitic	36.3 ± 0.6
5	50	0.01	-	Fully pearlitic	16.3 ± 0.8
6	50	10 to 500C	500 / 40min	Not fully pearlitic	33.6 ± 1.7
7	70	5 to 500C	500 / 40min	Not fully pearlitic	33.1 ± 1.8
8	70	5 to 600C	600 / 15min	Fully pearlitic	28.6 ± 1.1
9	70	10 to 550 C	550 / 20min	Fully pearlitic	39.3± 1.0

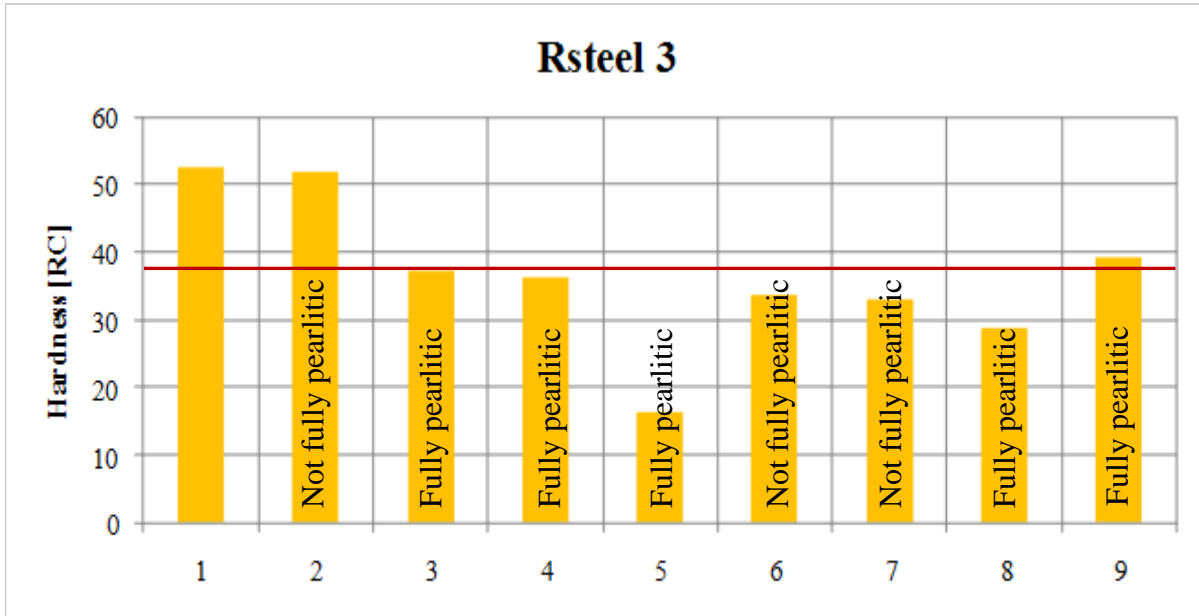
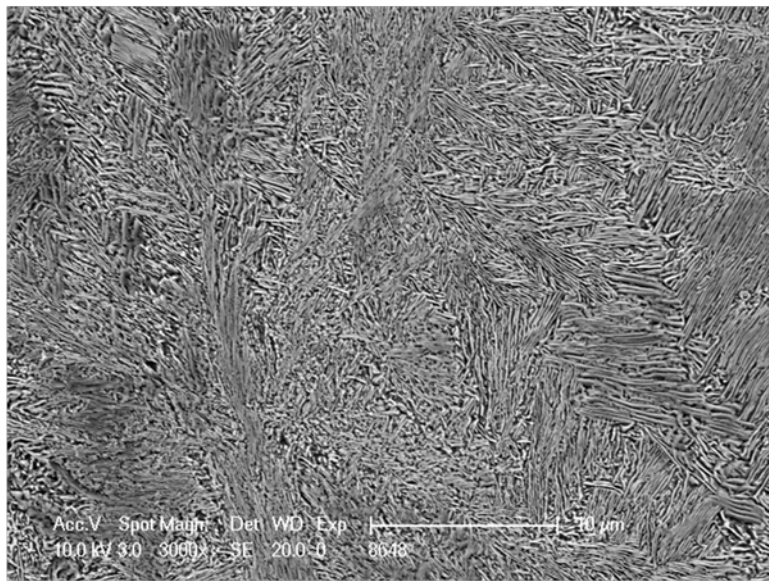


Figure 5.16 Results of hardness and microstructure of Rsteel3

Examples of the SEM micrographs from the sample obtained in experiment 9 are shown in Figure 5.17.



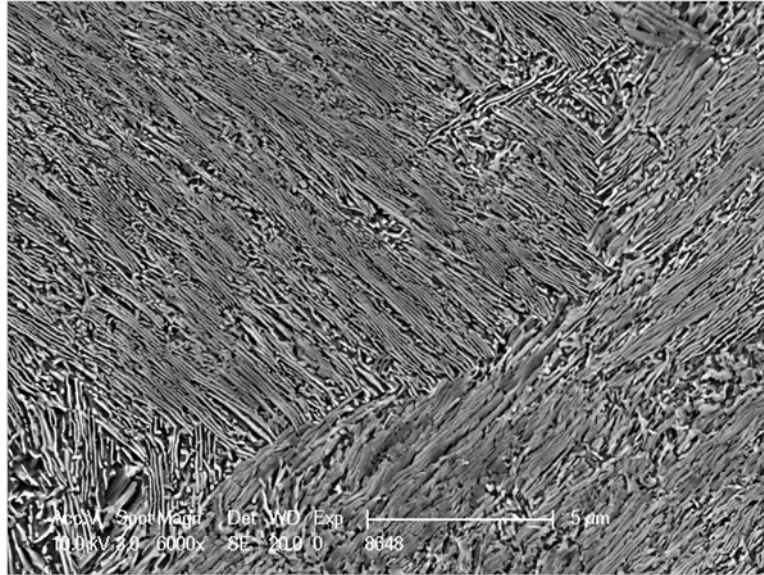


Figure 5.17 Scanning electron micrograph of Rsteel3 developed throughout the thermomechanical experiment number 9

Each sample from the thermomechanical experiments was observed in the SEM. The SEM examination revealed the differences in terms of the distances between cementite lamellas. Several micrographs were evaluated from each sample in order to obtain the most reliable value of interlamellar spacing. The smaller value of interlamellar spacing is associated with the higher hardness value of each steel. It is clear a relationship exists between the interlamellar spacing and hardness in these eutectoid steels, as shown by Clayton and Danks [83]. Figure 5.18 shows the hardness and interlamellar spacing of samples from each experiment that generated a fully pearlitic microstructure. Another way to show the dependence of hardness with interlamellar spacing is shown in Figure 5.19. The hardness decreases as the interlamellar spacing increases.

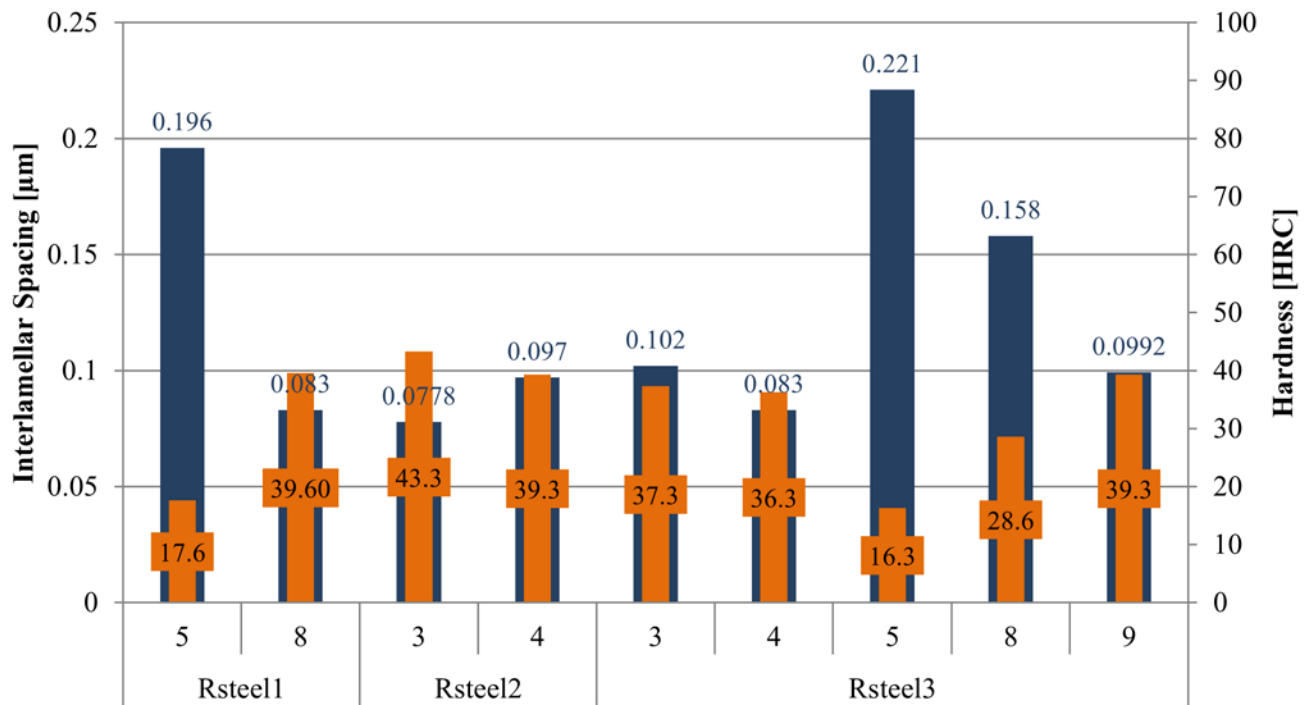


Figure 5.18 Hardness and interlamellar spacing values of thermomechanical experiments

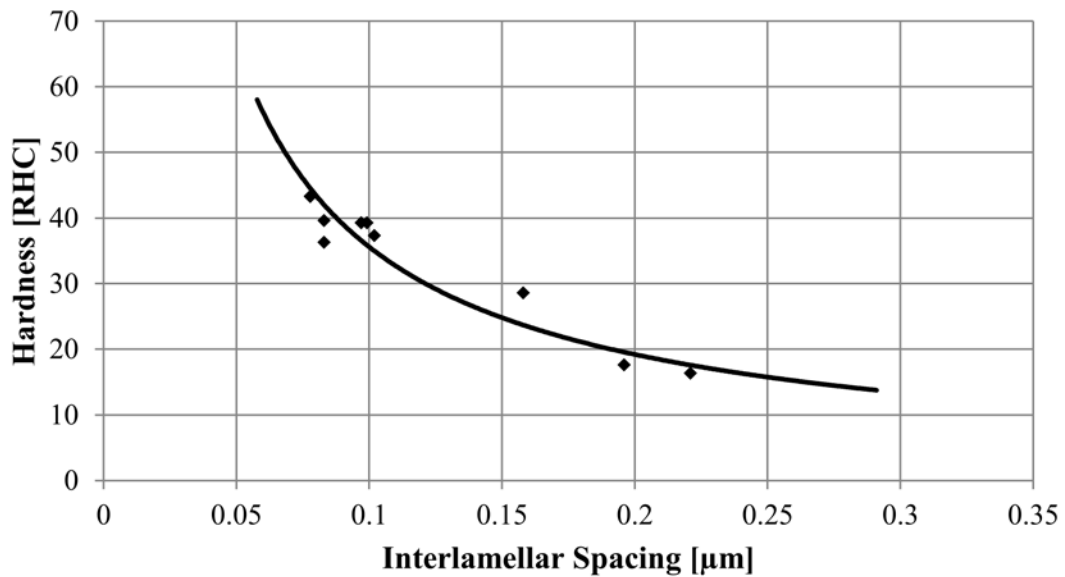


Figure 5.19 Hardness dependence on interlamellar spacing

5.3 MECHANICAL PROPERTIES

To obtain the criteria of rail steels in terms of hardness and microstructure a minimum 38 HRC and fully pearlitic was used to adjust the TMP experimental parameters. It provided the guidelines to design the best thermomechanical conditions for rolling the steels. The laboratory rolling was carried out at the US Steel facilities. The rolling procedure was adjusted to the rolling capabilities of the lab. The rolled plates produced from this procedure were microstructurally and mechanically tested.

5.3.1 Hardness Testing

Samples from the plates rolled at US Steel facilities were sectioned and the hardness was measured and the interlamellar spacing was assessed. The hardness values obtained on these samples are shown in Table 5.7. They are compared with the hardness values from commercial steels in Figure 5.20. It is clear that the three steels produced under laboratory conditions have the hardness values above the limiting criteria of 38HRC. The Rsteel2 registered the highest hardness value and the smallest interlamellar spacing of the three steels, as predicted by Clayton and Danks [83]. Even though Rsteel1 and Rsteel2 have similar interlamellar spacing, the hardness of Rsteel1 is slightly higher than that of the hardness of Rsteels2. In Figure 5.20 it is evident that the hardness values of the steels developed are higher than those of commercial steels.

Table 5.7 Hardness values and interlamellar spacing of the developed steels

	Rsteel1	Rsteel2	Rsteel3
Hardness [HRC]	40.4	43.1	38.3
Interlamellar spacing [μm]	0.095	0.084	0.096

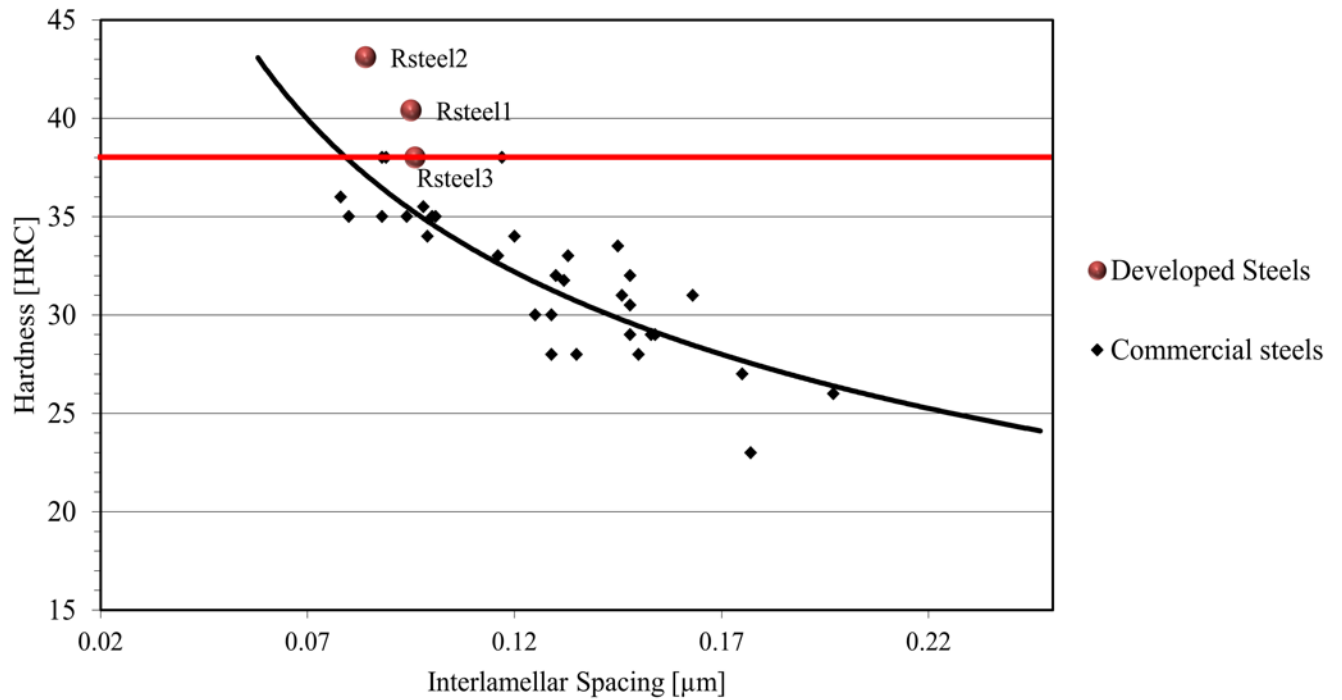


Figure 5.20 Relationship of hardness and interlamellar spacing of developed steels and commercial steels

Following the classic view of wear behavior, in which the hardness plays the most important role of the wear resistance [83, 84], the wear resistance of the steels developed in this research would be expected to be higher than that in the commercial steels.

5.3.2 Tensile Testing

Table 5.7 shows the mechanical properties such as the yield strength, the ultimate yield strength and the total elongation. The stress vs strain plot of the three steels is shown in Figure 5.21. It is evident from Table 5.8 that the Rsteel2 has the highest value of yield and tensile strength (1095.6 and 1459.6 MPa), though the Rsteel3 has the largest elongation value (20.4%) which would imply a larger toughness value. The yield strength is the most important value for structural design because it determines, practically, the stress at which the materials begins to deform plastically. Figure 5.22 shows that difference between the yield strength of the commercial steels and the yield strength of the steels developed in this research. This figure makes clear that the steels developed in this research have better resistance to deformation. The differences between yield strength and tensile strength in the three steels are very similar. Even though the chemical compositions are somewhat different, the materials should have similar strain hardening exponents. Another important value that the tensile test provides is the strain that these materials are able to reach. Meanwhile, although the commercial materials have an average strain below 10%, the developed materials in this research are above that strain value. Figure 5.23 shows a comparison of strain of commercial steels and the strain of developed steels. This characteristic of the developed steels is very important, a common view in any steel, is that the higher the carbon content the higher the yield strength but the lower is the elongation that it can withstand. However, in the developed steels, thanks, to a combination of other alloying elements and the thermomechanical path followed, the elongation exceeded the valued observed in typical commercial rail steels with lower yield strength.

Table 5.8 Tensile test values of rail steels developed by this research

	Yield Strength [MPa]	Tensile Strength [MPa]	Difference [TS-YS]	Strain [%]
Rsteel1	930.1	1298.9	368.8	20.4
Rsteel2	1095.6	1459.6	364.0	13
Rsteel3	847.4	1254.8	407.4	14.2

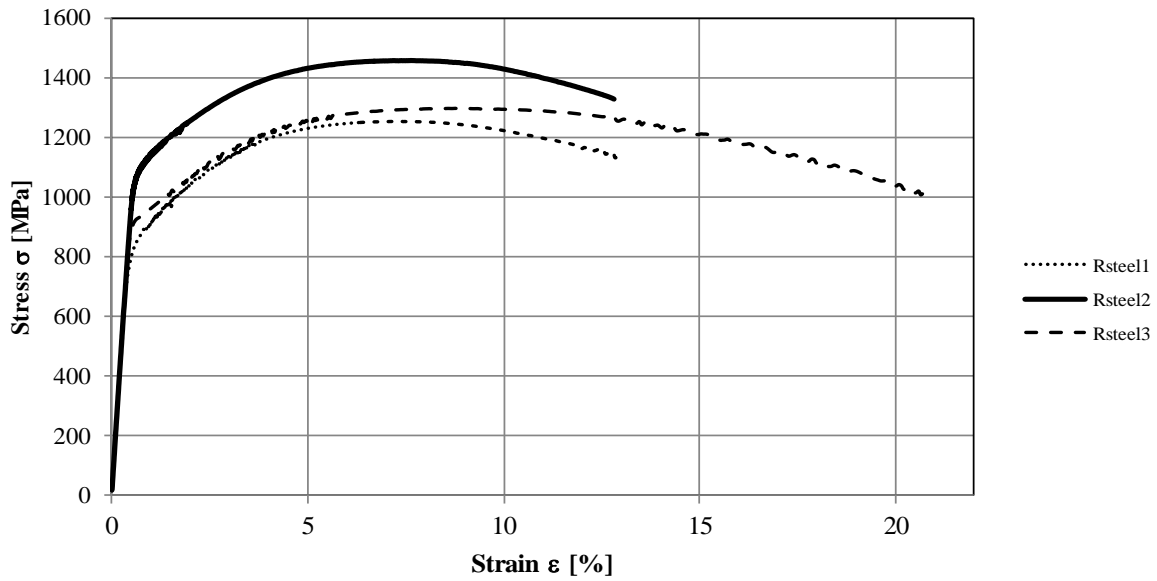


Figure 5.21 Stress vs Strain curves of the developed steels (Rsteel1, Rsteel2 and Rsteel3)

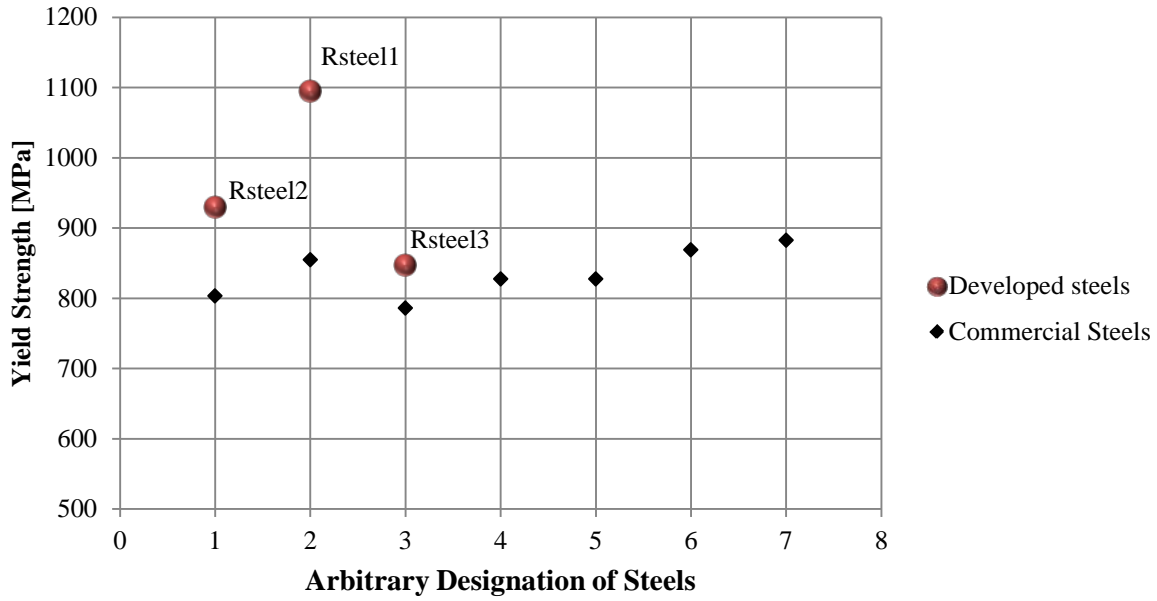


Figure 5.22 Comparison of yield strength between developed steels vs yield strength of some commercial steels

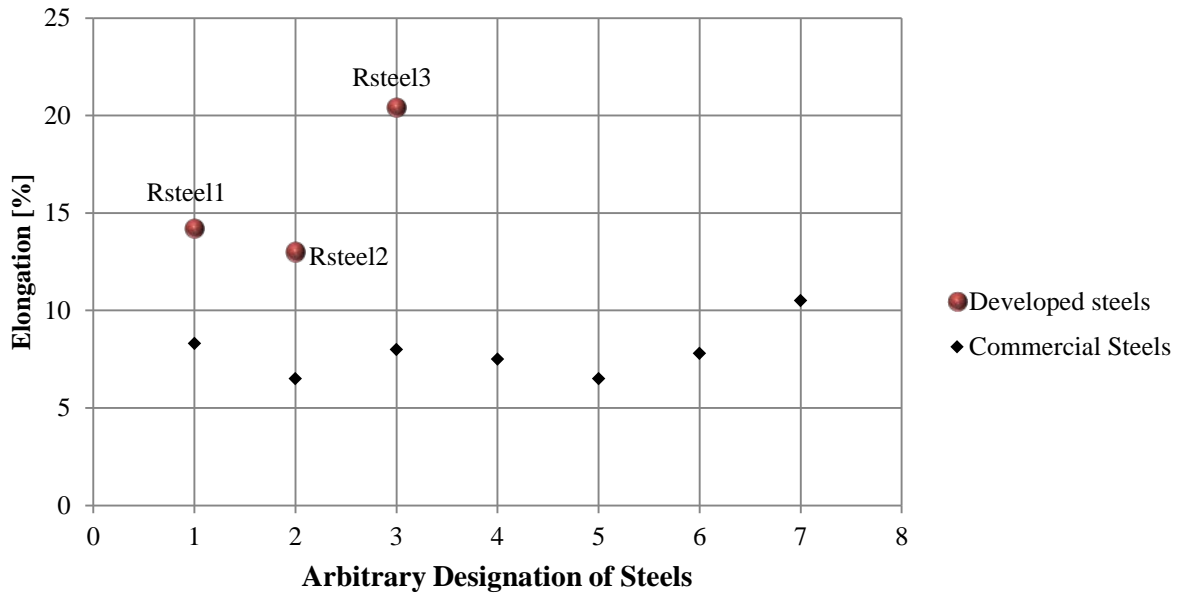


Figure 5.23 Comparison of elongation between developed steels vs elongation of commercial steels

5.3.3 Fracture Toughness

An additional criterion was established with the mechanical properties evaluated previously. The two steels developed with the higher yield strength were selected for fracture toughness evaluation. The fracture toughness (K_Q and/or K_{IC}) of Rsteel1 and Rsteel2 was assessed. The results from this evaluation are in Table 5.9. The fracture toughness of a material is its resistance to crack propagation or it is also known as the ability of the material to absorb energy through plastic deformation. This test assesses the ability of a material containing a crack to resist fracture; which is one of the most important properties of any material for virtually almost all design applications. Fracture toughness is a quantitative way for a material to express resistance to brittle fracture when a crack is present. If a material has high fracture toughness it will probably undergo ductile fracture. It is clear that the steel with larger deformation values also has the higher fracture toughness value, as mentioned previously in Section 5.3.2.

Table 5.9 K_Q / K_{IC} test results

	Notch location	CTOD at F_{max} [mm]	K_Q [MPa - m^{1/2}]	Test temp [C]
Rsteel 2	X-Y	0.005	47.48	23
Rsteel 3	X-Y	0.027	67.97	23

5.4 WEAR TESTING

As it was mentioned in Chapter 4, the wear test was carried out on the disk machine. The numbers of cycles performed on each sample were 50, 100, 1000, 5000, and 10000. The most common way to report the wear behavior is the weight loss versus the number of cycles performed on the disks. The disks were weighed right before and immediately after the test. However, no weight loss was registered in any of the wear tests performed. This initial observation is important because it means that the disk did not have weight loss even after 10000 cycles. The material in the disk was not removed during the test; it was displaced to the edges of the formed groove. The depth and the width of the channel formed were measured in four equidistant points along the perimeter described by the groove (see Figure 5.24).

A special high resolution digital microscope (Keyence) was used to measure these features. Table 5.10 shows the values of the average of the four points where depth and width measured in each steel.

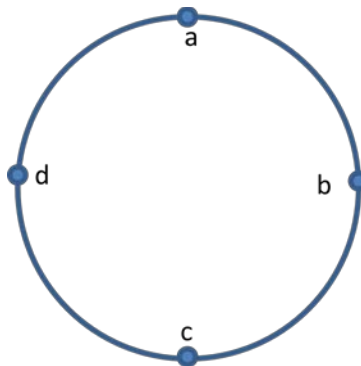


Figure 5.24 Schematic representations of the locations where the groove height and depth were measured

Table 5.10 Average of the depth and width values of wear test of each steel

Cycles	Rsteel1		Rsteel2		Rsteel3	
	Depth [μm]	Width [μm]	Depth [μm]	Width [μm]	Depth [μm]	Width [μm]
50	0	255.8	0	260.67	0	280.5
100	0	298.9	0	290.1	0	329.1
1000	153.2	641.2	136.93	568.1	118.2	637.5
5000	162.8	794.1	134.1	822.6	150.63	702
10000	169.3	833.2	138.2	845.5	158.3	803.4

The high resolution digital microscope takes a series of pictures focusing from the bottom of the groove up to the top of the original height, reconstructing a three dimensional image. In addition to this image, the microscope is equipped with special software that provides the depth profile of the groove generated. In each steel a series of micrographs were taken on each of the four locations previously described. From the depth and width profile generated with the series of micrographs, the wear behavior was quantified. Micrographs from the surface of the disk used before the wear testing and its three dimensional reconstruction are shown in Figure 5.25.

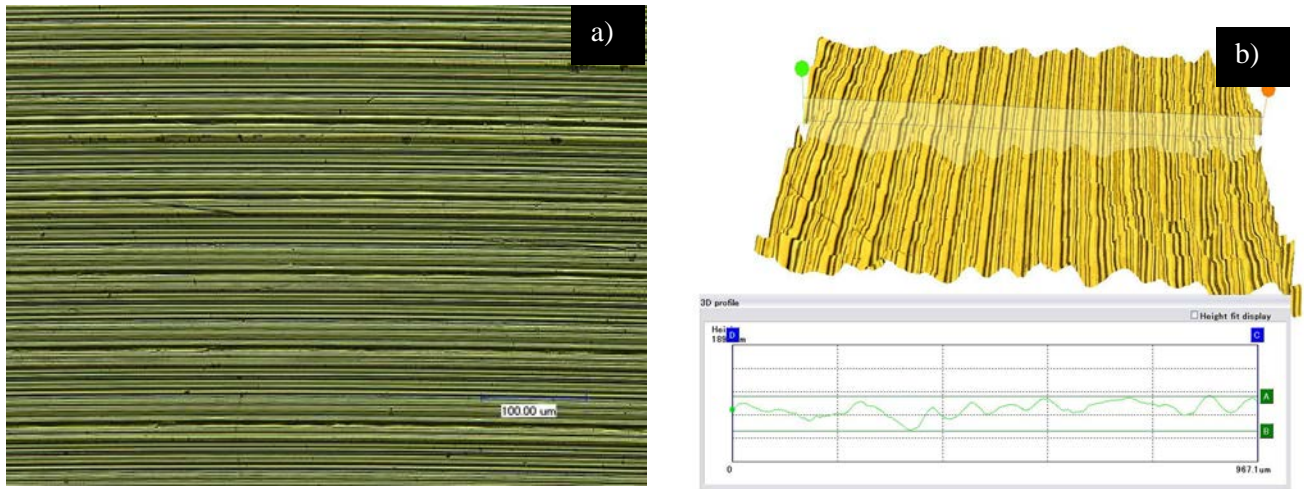


Figure 5.25 a) Micrographs of the surface of the wear test disk before performing the test. b) Three dimensional representation of the surface of the wear test disk before performing the test

Micrographs of the groove generated after 10000 cycles in the steels developed in this research are shown in Figure 5.26, 5.27 and 5.28. More micrographs from other different locations are shown in Appendix B.

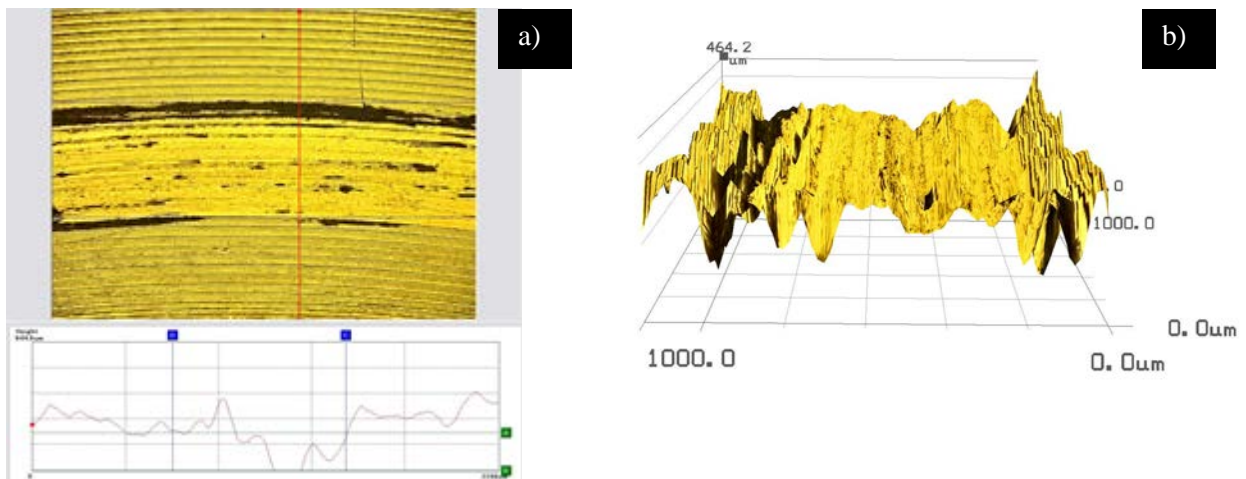


Figure 5.26 a) Micrograph from the top of the disk, showing a groove generated during wear testing after 10000 cycles in Rsteel1, b) Three dimensional representation of the groove generated

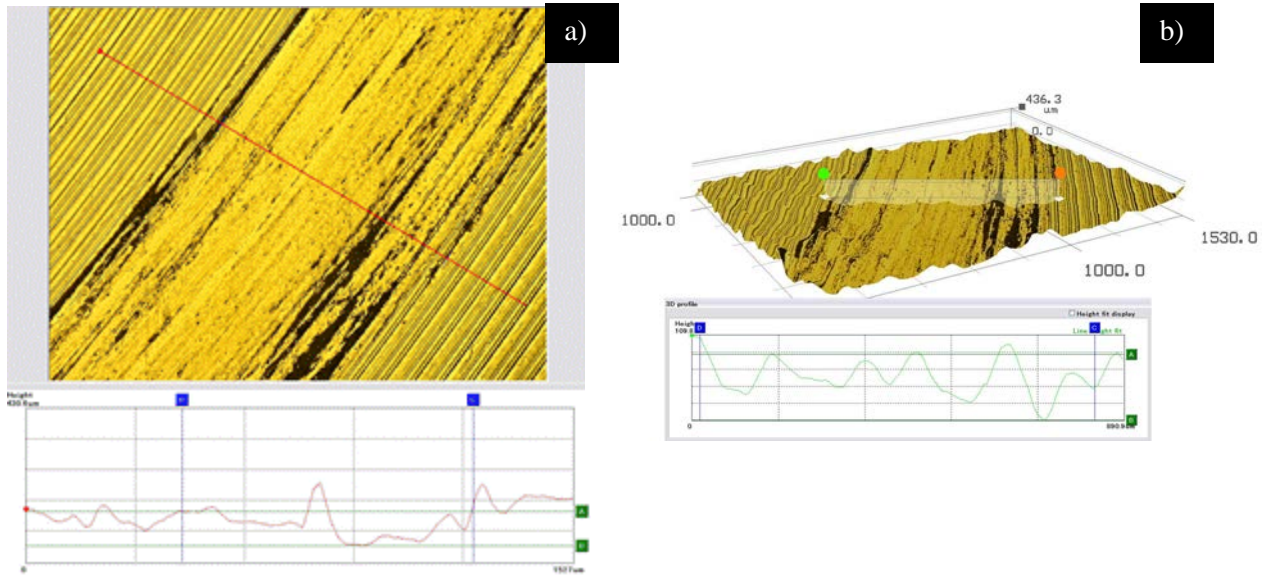


Figure 5.27 a) Micrograph from the top of the disk, showing a groove generated during wear testing after 10000 cycles in Rsteel2, b) Three dimensional representation of the groove generated

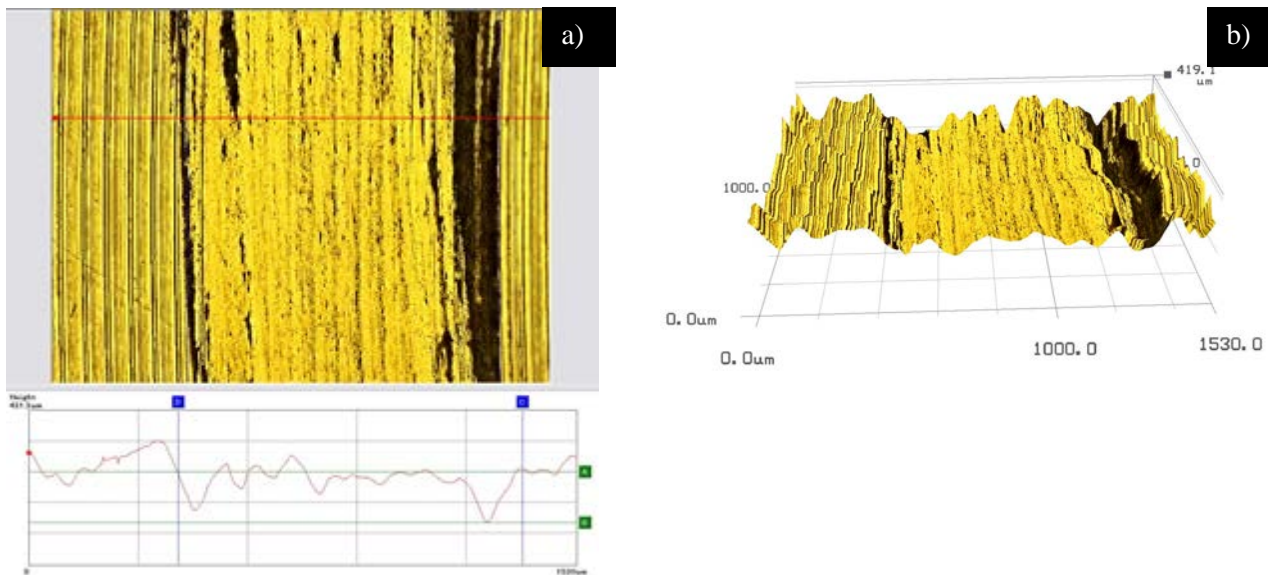


Figure 5.28 a) Micrograph from the top of the disk, showing a groove generated during wear testing after 10000 cycles in Rsteel3, b) Three dimensional representation of the groove generated

It is important to emphasize that none of the three steels developed in this research had a loss of weight even after 10,000 cycles. Even though the material was not removed from the disk, most of the material was relocated at each side of the groove. The height profile in all steels showed this behavior. Figure 5.29 shows, schematically, this behavior.

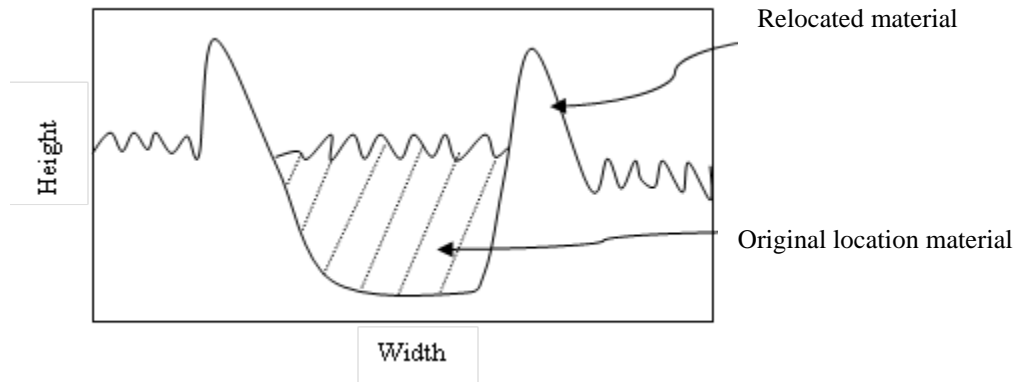
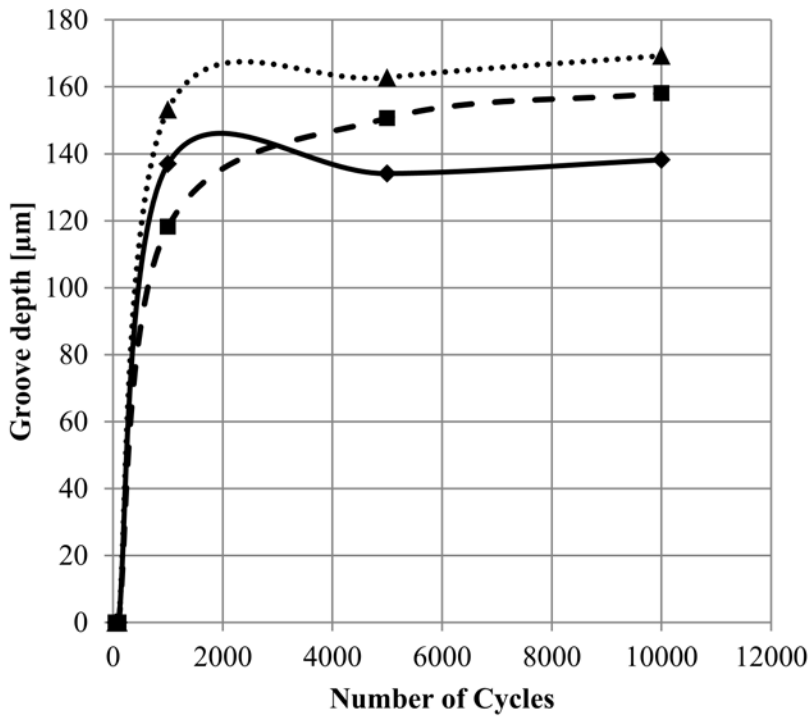
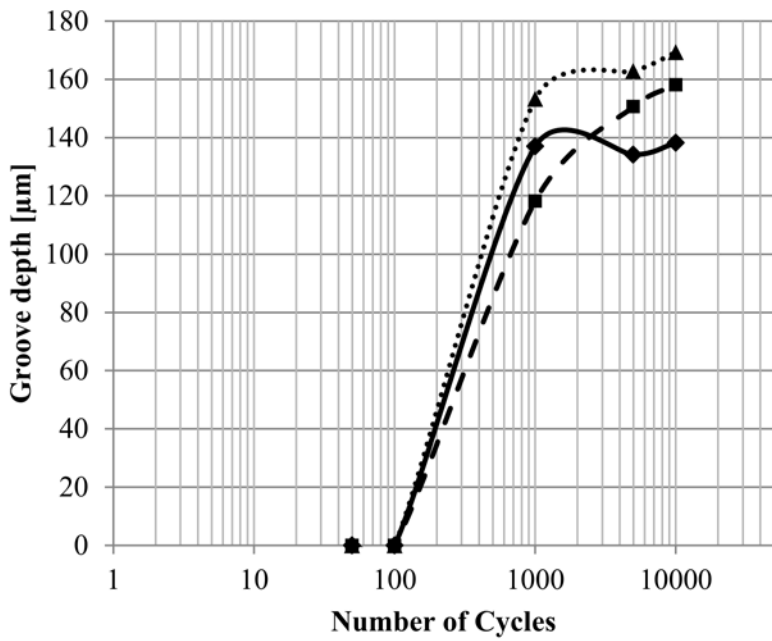


Figure 5.29 Schematic representation of the material relocation process during wear testing

Another interesting behavior found in the developed steels is that the depth of the groove generated during wear testing had a depth rate of growth during the first cycles of the test. However, this growth rate, after a certain number of cycles, seemed to decrease dramatically until it eventually stops growing. Figure 5.30 a) and b) show the relationship between the depth of the groove generated and the number of cycles. This behavior seems to be different when instead of the depth or only width and the number of cycles it is analyzed the area generated by the groove and its relationship with the number of cycles. Figure 5.31 shows how the area generated by the groove increase with the time, it increases with a slightly different slope after 1000 cycles.



a)



b)

Figure 5.30 a) Depth of generated groove with respect to the number of cycles of the developed steels b) Depth of generated groove with respect to the log number of cycles of the developed steels

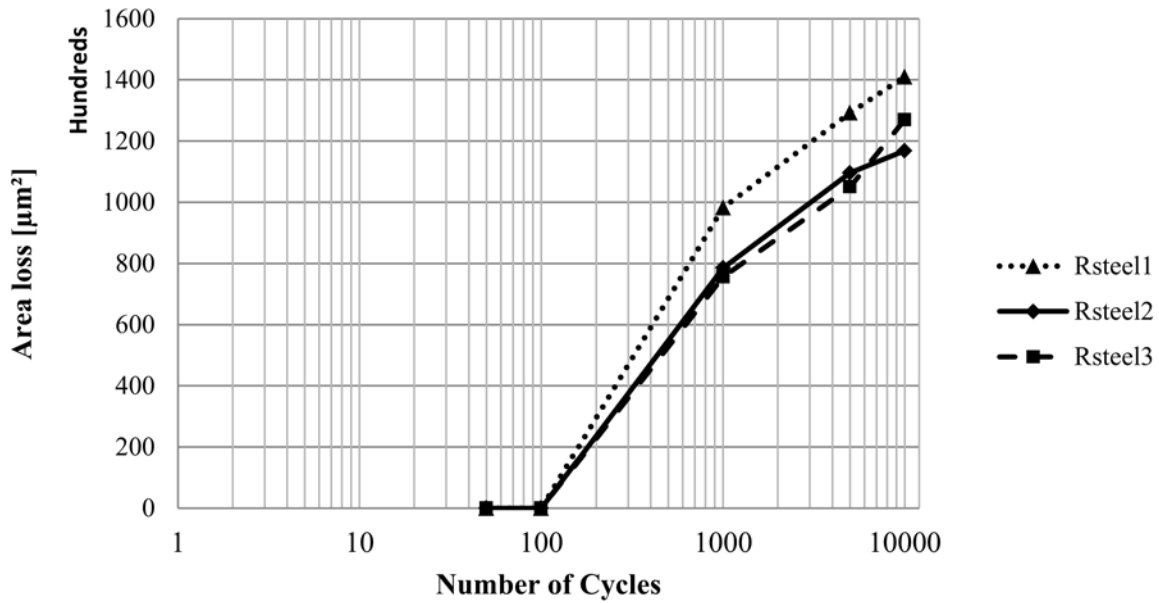


Figure 5.31 Wear measurements in terms of area displaced of the developed steels

5.5 ISOTHERMAL TRANSFORMATION STUDIES

In order to verify the differences between the isothermal behavior of the steels developed in this research and the commercial steels, two steels were selected for isothermal studies. The Rsteel2 and commercial steel identified as D were chosen. As described in Chapter 4.8, several heat treatments were performed for each one of these two studies. Figure 5.32 shows the S-shaped” or sigmoidal curves of austenite transformation to pearlite of commercial steel D. At any given temperature, the transformation occurred at different times. Initially, the transformation rate is slow associated with an incubation period. This means the time required for a stable nucleus occurs. As expected, the rate of transformation increases with the time. Latterly, the rate of

transformation slows when the microstructure gradually approaches a complete transformation. The shorter time at which the first nucleus occurs was at the isothermal temperature of 610C;

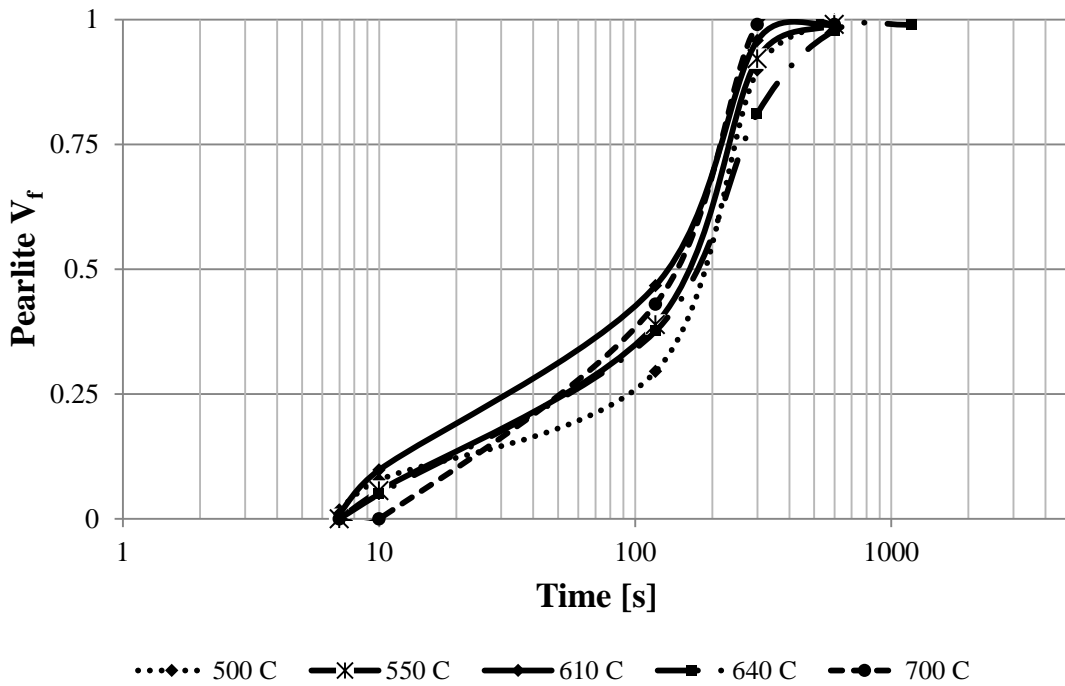


Figure 5.32 Fraction of pearlite transformed as a function of time for different temperatures of commercial steel D

the longest time at which the first nuclei appeared was at 700C. The fully pearlitic transformation occurred at a similar time for most of the isothermal temperatures, except for the isothermal temperature of 640C, when complete transformation took the longest time.

Figure 5.33 shows the fraction of austenite transformed to pearlite of Rsteel2. A similar behavior with commercial steels occurred in steel Rsteel2. However, it is clear that the incubation time of commercial steel D is shorter than the one in Rsteel2. Apparently, the first stages of transformation in Rsteel2 were slightly slower than in commercial steel D. In the Rsteel2 the shorter time at which the first nuclei appeared was at the isothermals 550 and 610C.

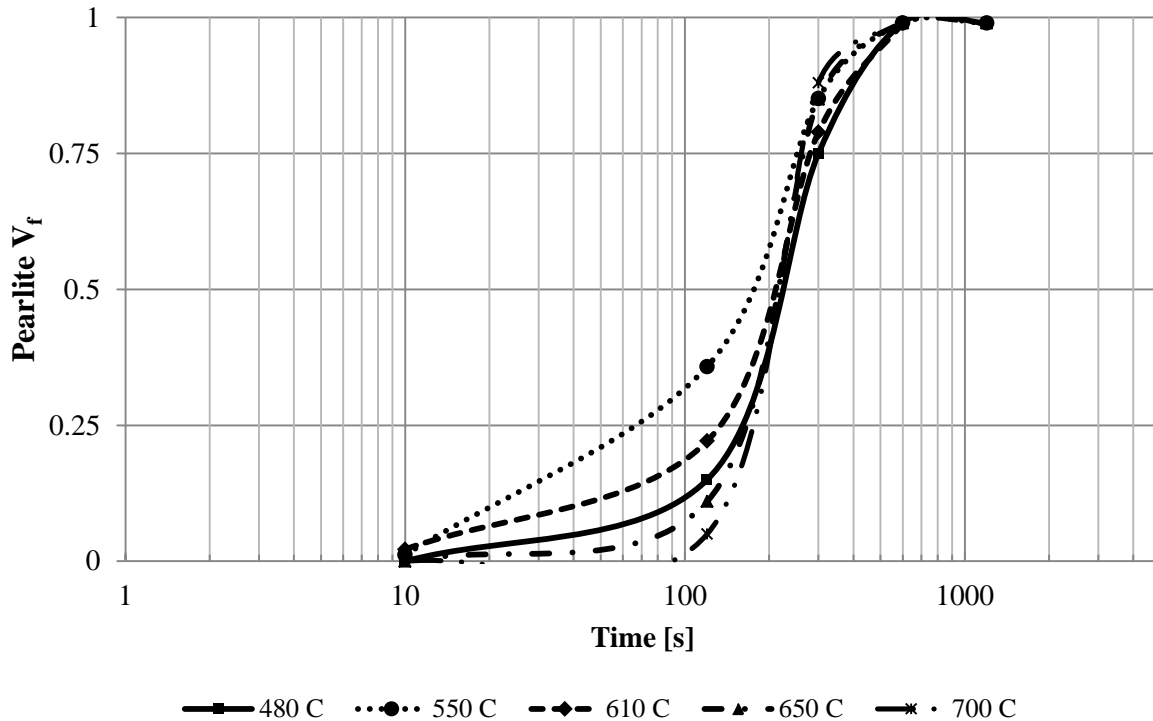


Figure 5.33 Fraction of pearlite transformed as a function of time for different temperatures of Rsteel2

The 700C isothermal treatment promotes the slower incubation process, however, a quick transformation occurred after a critical period of time (120s). The full pearlite transformation took place at similar times in most of all the isothermal treatments. The isothermal treatment at 550 C promotes the shorter time for complete transformation.

The time periods necessary for the beginning and completion of the full pearlite transformation at any given temperature are related to the initial and the end of the transformation curves in isothermal transformation diagrams, TTT. Figure 5.34 shows the temperature transformation time diagram (TTT) of commercial steel D formulated based on the isothermal transformation curves. This TTT diagram shows the starting transformation of

pearlite and the starting transformation of proeutectoid phase (cementite) as well as the finishing pearlite transformation only.

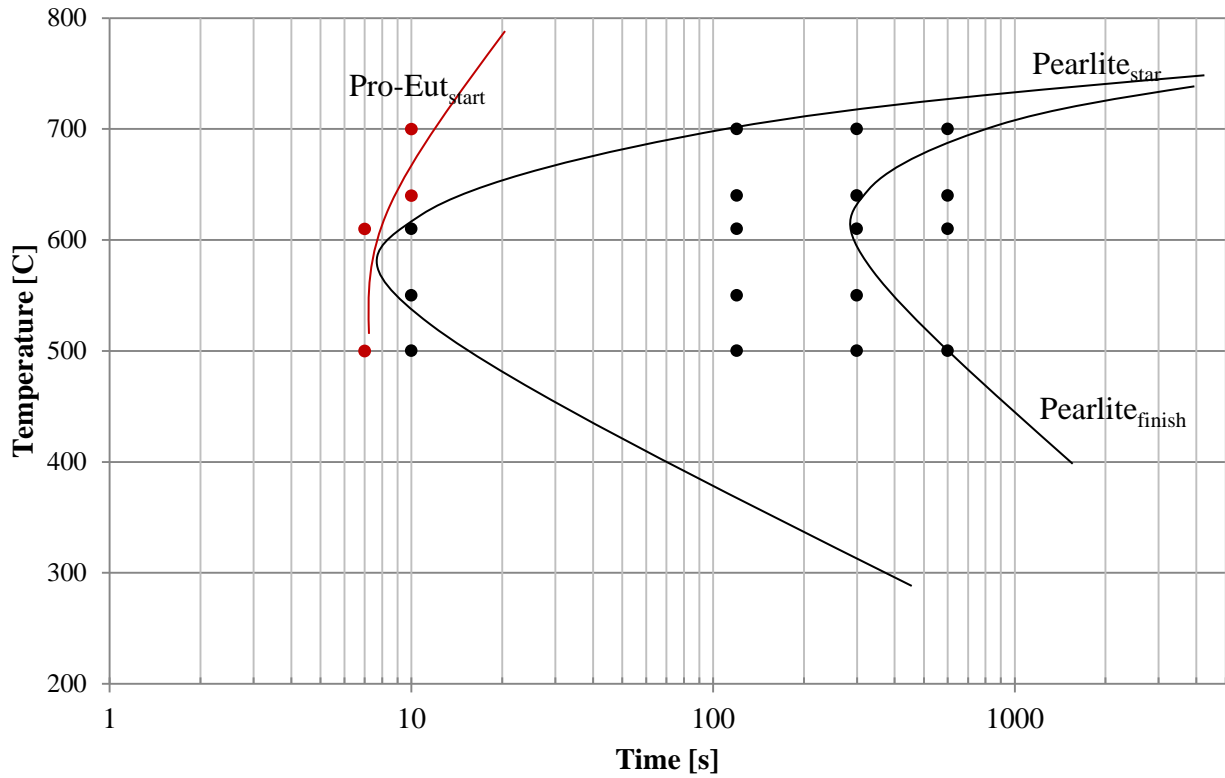


Figure 5.34 Temperature transformation time diagram (TTT) of commercial steel D

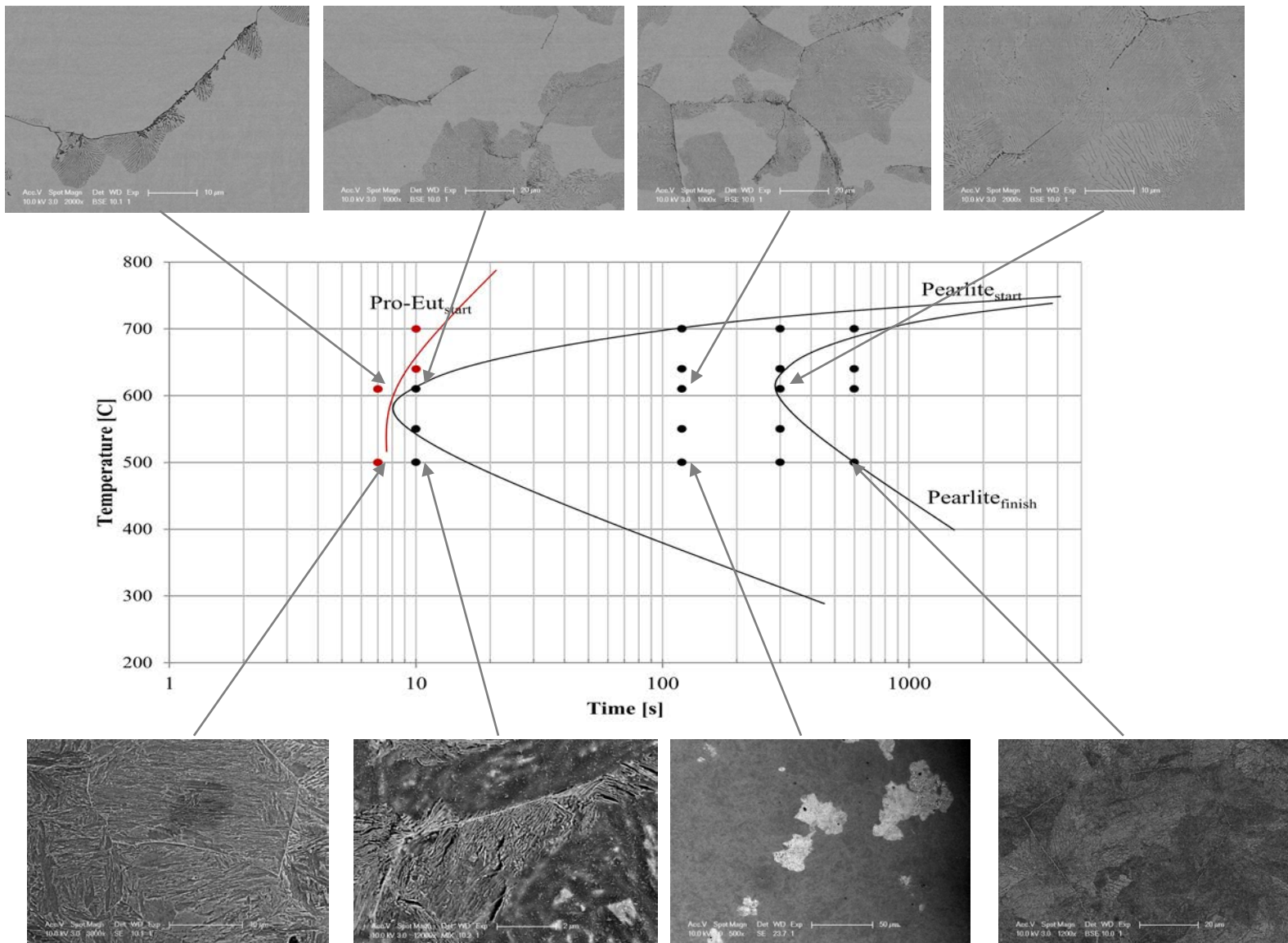


Figure 5.35 TTT diagram of commercial steel D and the micrographs at different times and temperatures

Figure 5.35 shows the TTT diagram of commercial steel D built based on the isothermal transformation curves as well as the micrographs used to measure the volume fraction of pearlite transformed. The right upper micrograph shows, in great detail, the first formation of proeutectoid cementite along the prior austenite grain boundaries and the initial nucleus development of pearlite. Subsequently with longer times, the microstructure evolves to larger pearlite volume fractions and most of the austenite grain boundaries are covered by the proeutectoid cementite. At lower isothermal temperatures, i.e. 500C, the precipitation of proeutectoid cementite is evident in the shorter time even before the formation of the first nuclei of pearlite.

Figure 5.36 shows the TTT diagram of developed steel Rsteel2; the lines of the initial pearlite formation and the complete transformation are shown. The diagram does not show any proeutectoid cementite formation at any time or temperature. The shorter time at which the austenite starts transforming to pearlite is 10s, however, due to the small amount (~1%) of pearlite observed, and the sensitivity of the technique used to follow the transformation, the transformation observed at 550 and 610C in 10s were negligible. Therefore, the time at which the first nucleus of pearlite was observed was at 120s. This represents a slower initial transformation rate than in commercial steel D. However, the complete pearlitic transformation in Rsteel2 took place at similar times as in commercial steel D.

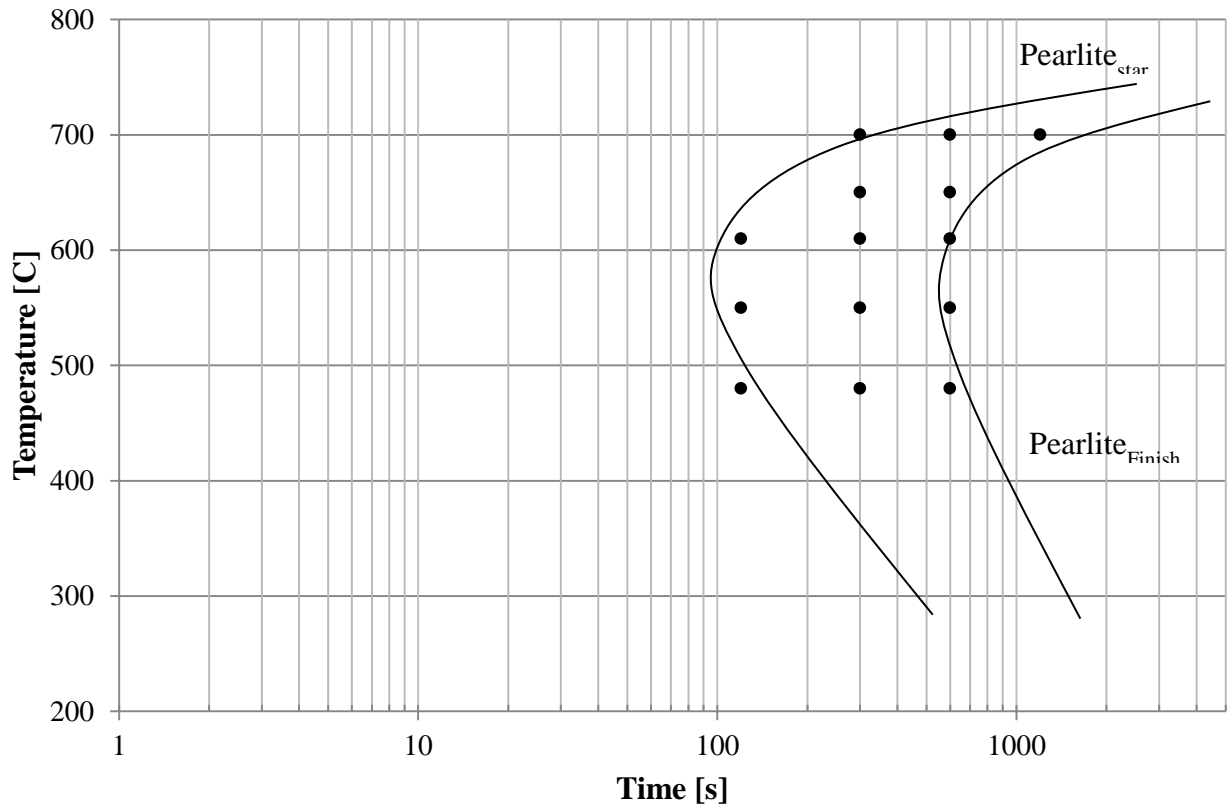


Figure 5.36 Temperature transformation time diagram (TTT) of developed steel Rsteel2

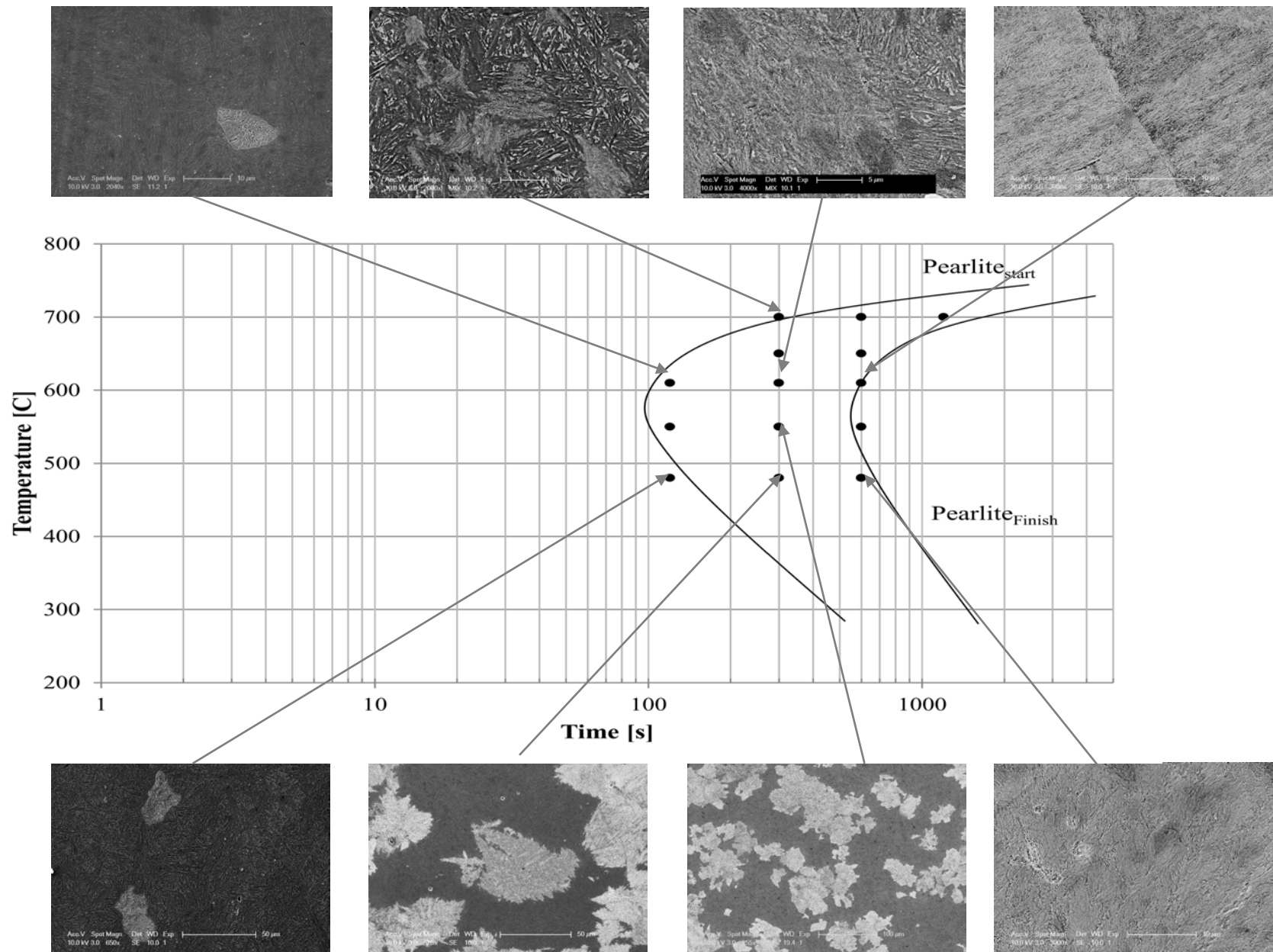


Figure 5.37 TTT diagram of Rsteel2 and the micrographs at different times and temperatures

Figure 5.37 shows the TTT diagram and some of the micrographs. The micrographs show the transformation evolution from the initial stages up to the complete transformation for different temperatures. Again, one important observation on the micrographs is that no proeutectoid cementite was observed, the prior austenite grain boundaries were not decorated by cementite. Figure 5.38 shows the example of a prior austenite grain boundary in a full transformed pearlite sample without the presence of proeutectoid cementite.

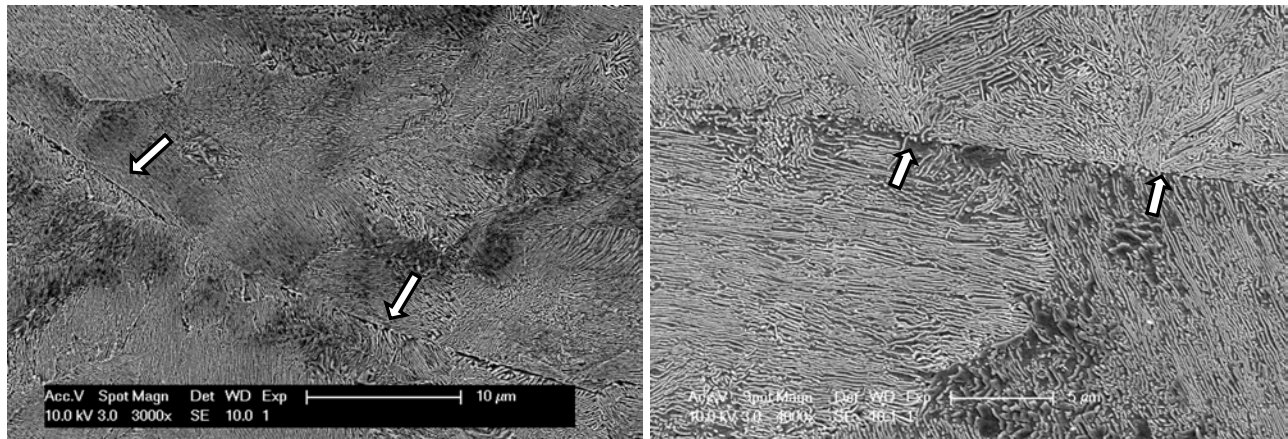


Figure 5.38 Prior austenite grain boundary of Rsteel 2 without proeutectoid cementite

6.0 DISCUSSION

6.1 MICROSTRUCTURAL ASSESSMENT

The different processing stages can have a strong dependence on the microstructure development, which has a direct relationship to the final mechanical properties. Two types of phases/microconstituents were identified on the microstructural assessment; the main phase (in eutectoid and hyper-eutectoid steels) is pearlite (P) and proeutectoid cementite (PC). It is then essential to understand the effect of these phases on different properties of these steels. Figure 6.1 shows the examples of pearlitic microstructure and proeutectoid cementite.

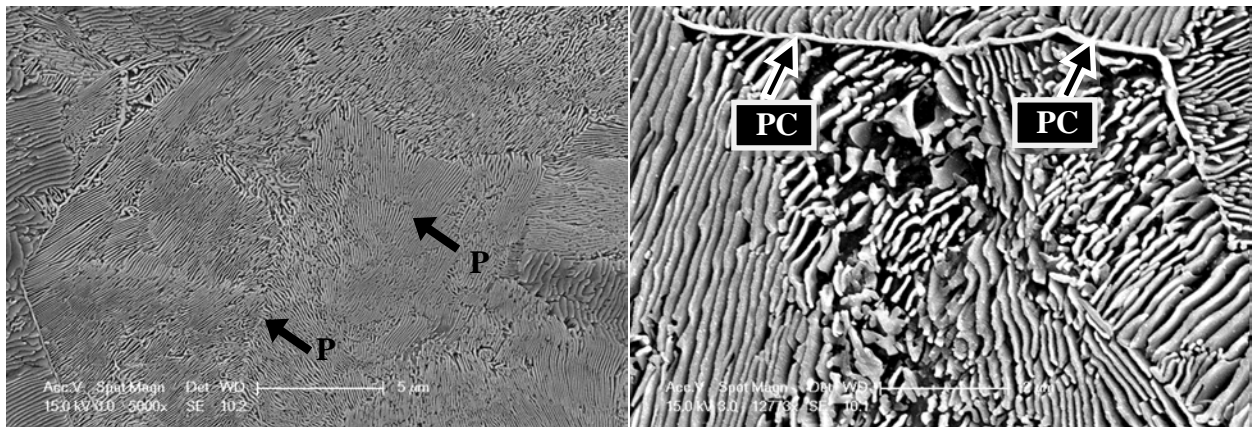


Figure 6.1 Typical appearance of the pearlite (P) and proeutectoid cementite (PC)

Apparently, there are three main microstructural features that control the deformation and fracture process in eutectoid and hyper-eutectoid steels; these three features are interlamellar spacing, pearlite colony size and prior austenite grain size. As shown previously by different authors [14, 76-77, 90-95], the yield strength is known to increase as the pearlite interlamellar

spacing decreases; more specifically, the yield strength is directly proportional to the reciprocal root of the interlamellar spacing, as shown in Figure 6.2, even though there is not a significant variation in interlamellar spacing between the commercial steels, as shown in Figure 6.3 .

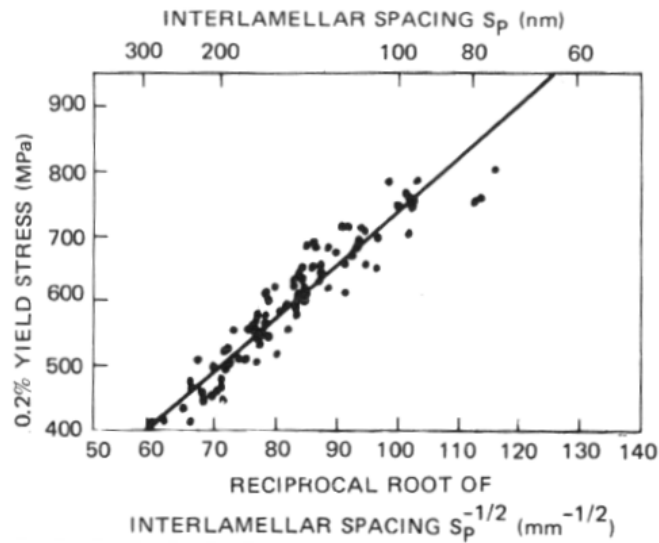


Figure 6.2 Relationship between 0.2% offset yield strength and interlamellar spacing of pearlite in eutectoid carbon steels

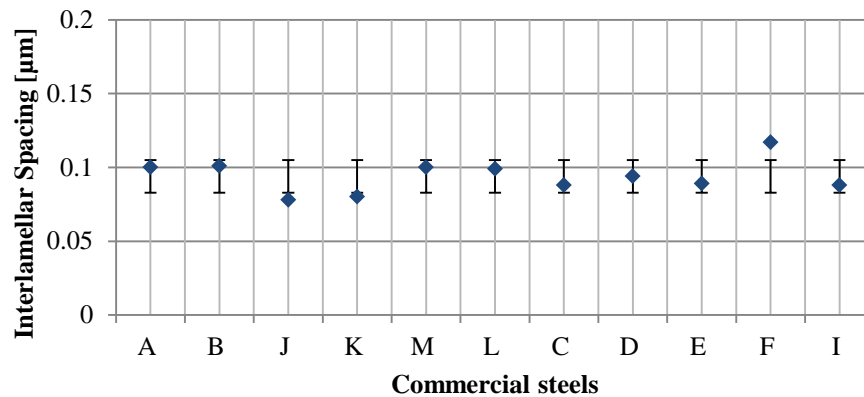


Figure 6.3 Interlamellar spacing of different commercial steels

The pearlite interlamellar spacing has a strong influence on the isothermal transformation temperature or, more specifically, with the ΔT ; the larger is the ΔT , the smaller is the interlamellar spacing [96]. However, some authors like Gladman [59] and Bernstein [81], have seen some variation (base on statistical analysis) of interlamellar spacing with respect to austenite grain size. Interlamellar spacing increases as austenite grain size decreases.

From equation 5.1 we can see that pearlite colony size has only a slight effect on yield strength. The inverse square root of a larger number (compared with the interlamellar spacing at least twenty times larger) would not be a large influence on the final yield strength. The small influence of pearlite colony size on the strength has been reported by different authors [81,76 and 96].

The third microstructural characteristic that was evaluated on the microstructural assessment is prior austenite grain size. In low carbon steels, this microstructural feature affects the hardenability and toughness. Because the transformation to ferrite is nucleated at grain boundaries, therefore the greater the amount of grain boundaries, the greater will be the density of nucleation sites and the lower the hardenability. The importance of the austenite grain size on toughness in low carbon steels and in alloy steels is also well known. The austenite grain refinement is an approach to achieve high toughness at high strength. In high eutectoid and hyper-eutectoid steels, research has indicated that impact toughness (as measured by Charpy impact testing), increases with decreasing prior austenite grain size for equivalent interlamellar spacing [73, 97]. Tensile ductility of these materials also increases with decreasing prior austenite grain size [98]. In the microstructural assessment, it was found that the prior austenite grain size has a minimum effect on the yield strength (see Figure 5.6). This is in agreement with the results of Bernstein [73] and Taleff [96].

Another microstructural feature to which little attention has been paid is the cleanliness of the steels. It refers to its relative freedom from non-metallic inclusions. Manganese sulfides and aluminum oxides were the main non-metallic inclusions observed in the commercial steels. However, relatively small amounts of SiC , TiN, VN, CaCO₃ and MgCO₃ were also observed. It has been stated that the general ductility decreases exponentially as the volume fraction of non-metallic inclusions increase. The detrimental effect on ductility is larger when the inclusions (MnS) are elongated during the hot rolling process [99]. This behavior is very common in sulfides. During deformation, voids are nucleated around sulfides as well as other types of inclusions, which grow and link up to give rise to the subsequent fracture. Other types of inclusions like oxides and even carbides can crack and, thus, give rise to void nucleation. Globular inclusions have low concentration factors in the transverse direction, which produces a lower void growth than do planar inclusions. Figure 6.4 shows how the total ductility is affected by the volume of sulfides.

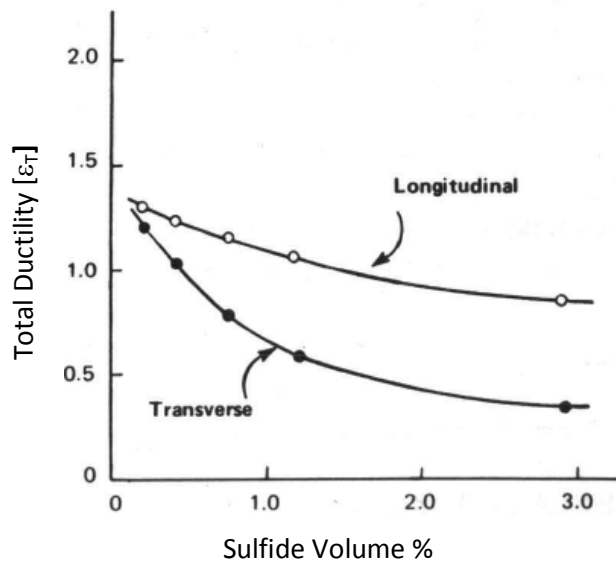


Figure 6.4 Effect of sulfide volume fraction on longitudinal and transverse total ductility at fracture

The presence of the proeutectoid phase in the commercial steels was observed and quantitatively assessed. Table 5.2 shows the results of this assessment. The proeutectoid cementite was found decorating the prior austenite grain boundaries. Even though the presence of proeutectoid phase has been observed previously in rail steels, it hasn't been considered as a main factor that deteriorates the performance of this structural component. G. Krauss [15] has identified the proeutectoid cementite as a main source of grain boundary embrittlement. However, others properties can be affected by the presence of proeutectoid cementite, for example the drawability and toughness. The larger the volume fraction of proeutectoid cementite the lower the toughness in terms of impact transition temperature [68].

Rail components suffer from different types of damage; rolling contact fatigue (RCF) and wear are some of the most important. RCF is a family of damage phenomena that appear on and in rails due to overstressing of the rail material. This damage may appear first on the surface (e.g. head checks, shelling, squats) or the subsurface (deep seated shell). In either case, these phenomena are the result of repeated overstressing of the surface or subsurface material by the hundreds or thousands or millions of intense wheel-rail contact cycles [2]. Two key processes govern RCF - crack initiation and crack propagation. These processes are governed by a number of factors. Wear was found to be a three stage process, as mentioned in Chapter 2.

The microstructural features influence rolling contact fatigue and wear in different ways. The relationship between the effects of non-metallic inclusions on contact fatigue life has shown that more oxides, especially hard or brittle inclusions, such as alumina and silicates result in

shorter fatigue life, because they are discontinuous. Most of the rail fatigue failure initiates at oxide inclusions in the head [100]. Figure 6.5 shows the results of rolling contact fatigue tests [100] and their dependence with respect to the volume fraction of oxides.

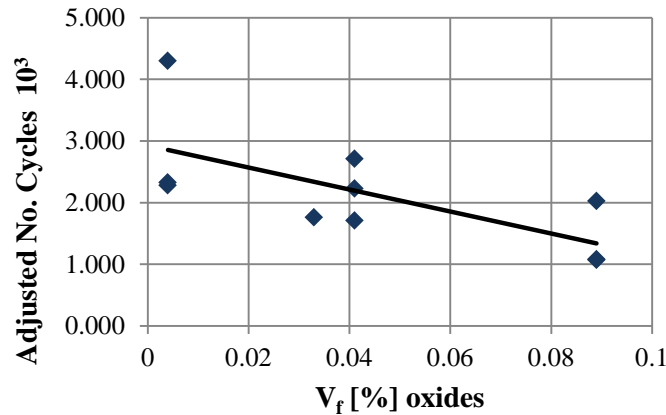


Figure 6.5 Rolling contact fatigue No. cycles versus volume fraction of oxides

Ev.A. Shur [101] measured the amount of oxygen from different non-metallic inclusions of rail steels and related it to the rail fatigue life in terms of millions of gross tons (MGT). In Figure 6.6, it is observed that the lower oxygen content the larger the MGT. Above an oxygen critical content (7ppm), the fatigue life is reduced drastically.

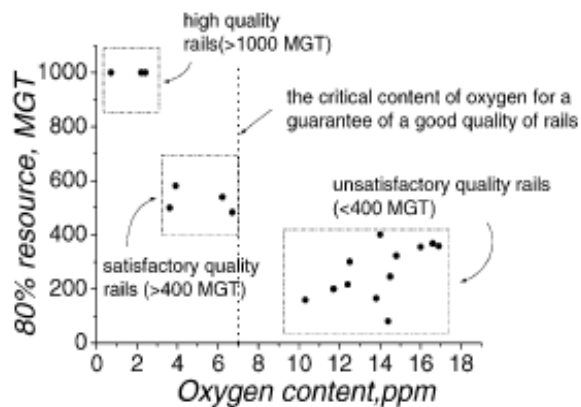


Figure 6.6 Relationship between the 80% resource of rail and oxygen content in rail steels

Clayton and Danks [83] have shown, in previous work, that hardness has a strong effect on wear in eutectoid steels. This is based on the hardness that is modified by the interlamellar spacing, Figure 2.25 shows the hardness correlation with wear resistance for rail steels.

The prior austenite grain size apparently plays a role on rolling contact fatigue resistance of eutectoid steels. V. Sagadze [102] using (C-Mn) in steel with 0.75% C, 0.90% Mn, 0.20% Si, with fine and coarse interlamellar spacing, and globular pearlite, has shown the existence of a close relationship between prior austenite grain size and RCF (Figure 6.7). The growth of austenite grain leads to a substantial decrease of steel contact fatigue limit.

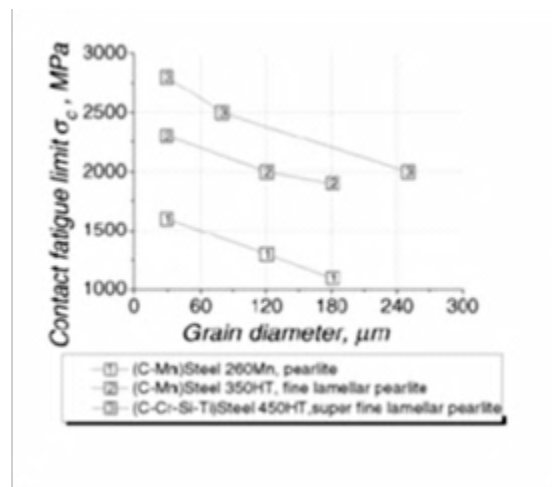


Figure 6.7 Relation between contact fatigue limit and prior austenite grain size

Based on the microstructural observations obtained in this study and coupled with the wear performance of the premium rail steels provided by the Transportation Technology Center, a linear relationship was developed, as shown in Figure 6.8. The wear factor (WF) in Figure 6.8 is strongly related to a series of microstructural factors, i.e., the type, size and volume fraction of

non-metallic inclusions, the matrix hardness, the volume fraction of proeutectoid cementite and the microstructure (especially the interlamellar spacing). Even though the actual wear seems to have a correlation with the WF, the straight line that describes a theoretical perfect correlation has a R^2 value only 0.4368.

$WF = f(\text{NMI, Proeutectoid Cementite, Hardness, Prior austenite grain size, Interlamellar spacing})$

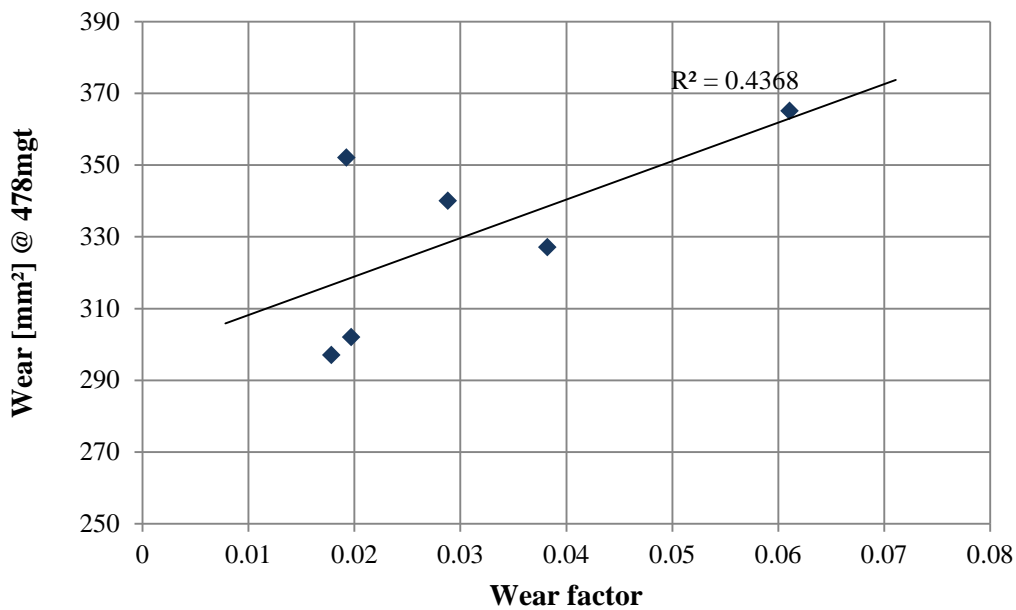


Figure 6.8 Relationship between wear versus wear factor

6.2 THERMOMECHANICAL EXPERIMENTS

The primary goal of modern thermomechanical treatment is to refine the grain structure in order to obtain the best combination of mechanical properties in the hot rolled condition. In low carbon steels, the grain refinement is recognized as the only way to simultaneously improve strength and

toughness. In the case of eutectoid and hyper-eutectoid steels, the strength is related to the interlamellar spacing and the toughness with the prior austenite grain size.

The microalloyed steels are usually alloyed with small quantities of strong carbide forming elements such as vanadium, titanium and niobium. The effect of these alloying elements is to retard the progress of recrystallization by being dissolved in austenite (solute-drag) or by forming precipitates (precipitation pinning) such that a fine austenite can be produced before the pearlite transformation. Similar solute drag behavior of these alloying elements in high carbon chromium steels for ball bearings has been reported by Nobuhisa et al. [103]. Then the main goal of the thermomechanical experiments in eutectoid steels is to develop a fine prior austenite grain size which can be a factor to improve the toughness and the refinement of interlamellar spacing to get high strength.

6.2.1 Rsteel1

Table 5.4 shows a summary of the thermomechanical experiment (TMP) results for Rsteel1. The thermomechanical experiment 1 produced a fully martensitic material. The main idea for performing this experiment was to measure the austenite grain size right after the second deformation. The TMP experiments that successfully produce a fully pearlitic microstructure were the TMP 5, 7 and 8. The microstructures generated in TMP 5 were fully pearlitic but with a coarse interlamellar spacing (Figure 6.9). Clayton and Danks [83] showed that this microstructural feature is related to hardness. As shown in Figure 5.18, the average interlamellar spacing measured was $0.196\mu\text{m}$; this is probably the main reason for the low hardness values obtained in this TMP experiment.

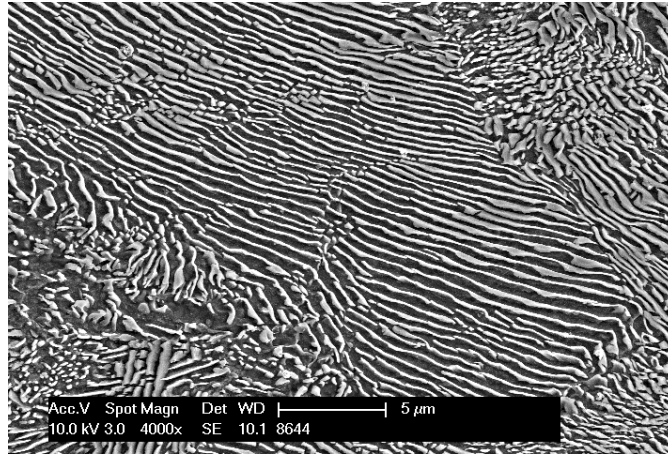


Figure 6.9 Coarse pearlite generated through TMP5

In the case of the TMP 7 and 8, both experiments using the same amounts of deformations and the same isothermal temperature (600C) but with different isothermal times (10 and 20min respectively), generated a fully pearlite microstructure. The hardness value of TMP experiment 7 was smaller than that in experiment 8, even though the interlamellar spacing is quite similar (0.91 and 0.083 μm), the hardness is different (7HRC). This difference in hardness can be attributed to a different source of hardening. For example, precipitation hardening. Both samples were examined by TEM. Figure 6.10 shows the micrograph of the TMP 7 (isothermal treatment 600C for 10min).

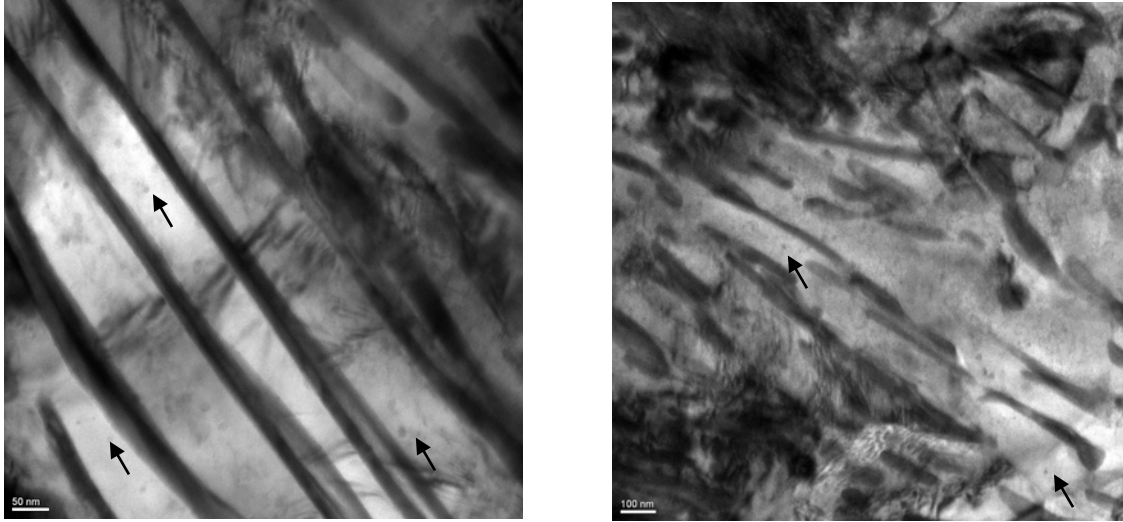


Figure 6.10 Bright field TEM micrographs from TMP 7 of Rsteel1

The TEM evaluation showed the presence of small precipitates in the ferrite of the pearlite. The black arrows point out the particles. Chemical analysis of these precipitates was performed. The Figure 6.11 shows the energy dispersive X-Ray (EDX) spectrum of one of the particles. The chemical analysis indicates the presence of vanadium, chromium and molybdenum. Apparently, the precipitates are carbides of these elements. It is important to mention that no significant amount of precipitates were found in this sample.

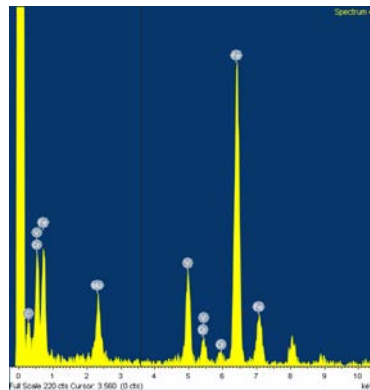


Figure 6.11 Chemical analysis spectrum from one precipitate observed in the sample of TMP experiment 7

Figure 6.12 shows the micrograph of the TMP 8 (isothermal treatment 600C for 20min). The presence of precipitates in ferrite was also observed in this sample. The black arrows point out some of them. It is evident the volume fraction of these precipitates is larger than that in the TMP 7. Chemical analysis was also performed in some of these precipitates.

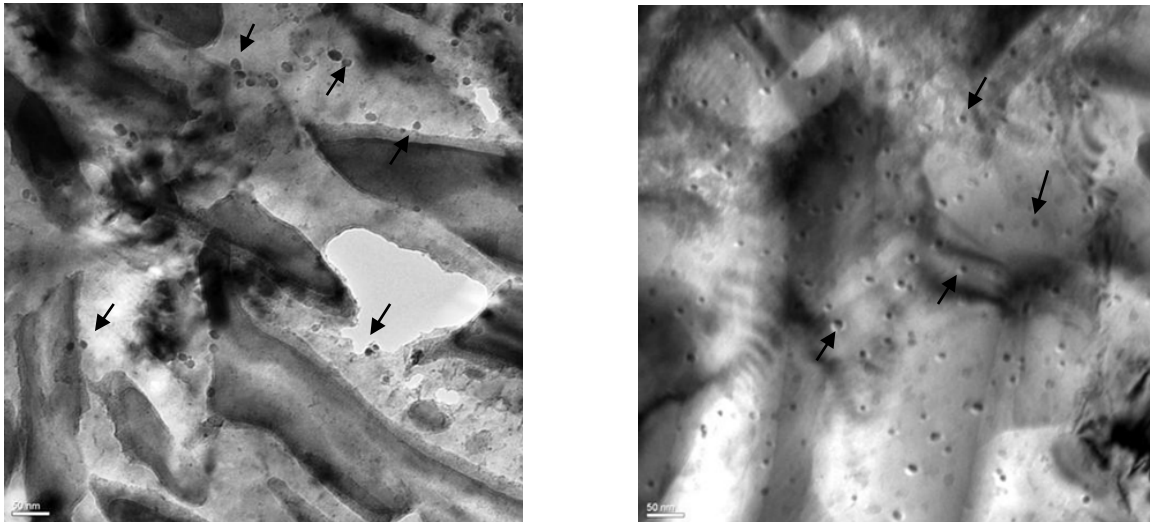


Figure 6.12 Bright field TEM micrographs from TMP 8 of Rsteel1

The results show the presence only of vanadium and silicon. Figure 6.13 shows the chemical spectrum of one of the precipitates.

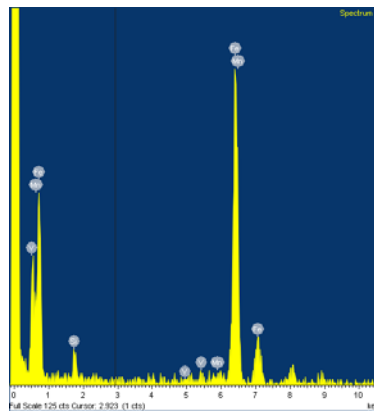


Figure 6.13 EDX spectrum from one precipitate observed in the sample of TMP experiment 8

The differences in volume fraction of particles precipitated between the TMP 7 and 8, seems to be the reason for the hardness differences when the interlamellar spacing is quite similar. Precipitation of vanadium carbides in ferritic pearlite has been reported by K. Han, G.D.W. Smith and D.V. Edmonds [104] in vanadium-bearing steel (0.79C-0.62Mn-0.22Si-0.2V).

6.2.2 Rsteel2

As the in Rsteel1, the first TMP experiment was to perform the deformation path and then quench the sample in order to obtain the austenite grain size produced by the deformation path. The grain size generated was 45 μ m. The TMP which produces a fully pearlitic microstructure was performing experiments 3 and 4. The other TMP experiments, i.e., 5 and 6, even though they started developing a pearlitic microstructure, the complete transformation did not take place. Apparently the kinetics of pearlitic transformation at 500C was slow and requires more time. An increment of temperature of 50C was enough for the same isothermal time to complete the pearlitic transformation. This is the case of TMP experiments 3 and 4; both developed a fully pearlitic microstructure and exceed the threshold hardness value. The interlamellar spacing of these two experiments was 0.0778 and 0.097 μ m, respectively. Although there were big differences of isothermal time (20min and 100min), the difference in hardness between these experiments was only 4HRC. A TEM evaluation revealed the presence of a secondary precipitation in pearlitic ferrite in the sample of experiment 4. However, no precipitates were observed in the sample of experiment 3. Figure 6.14a shows the bright field TEM micrograph of the sample of experiment 4, Figure 6.14b shows the EDX micro chemical analysis spectrum of the particle encircled.

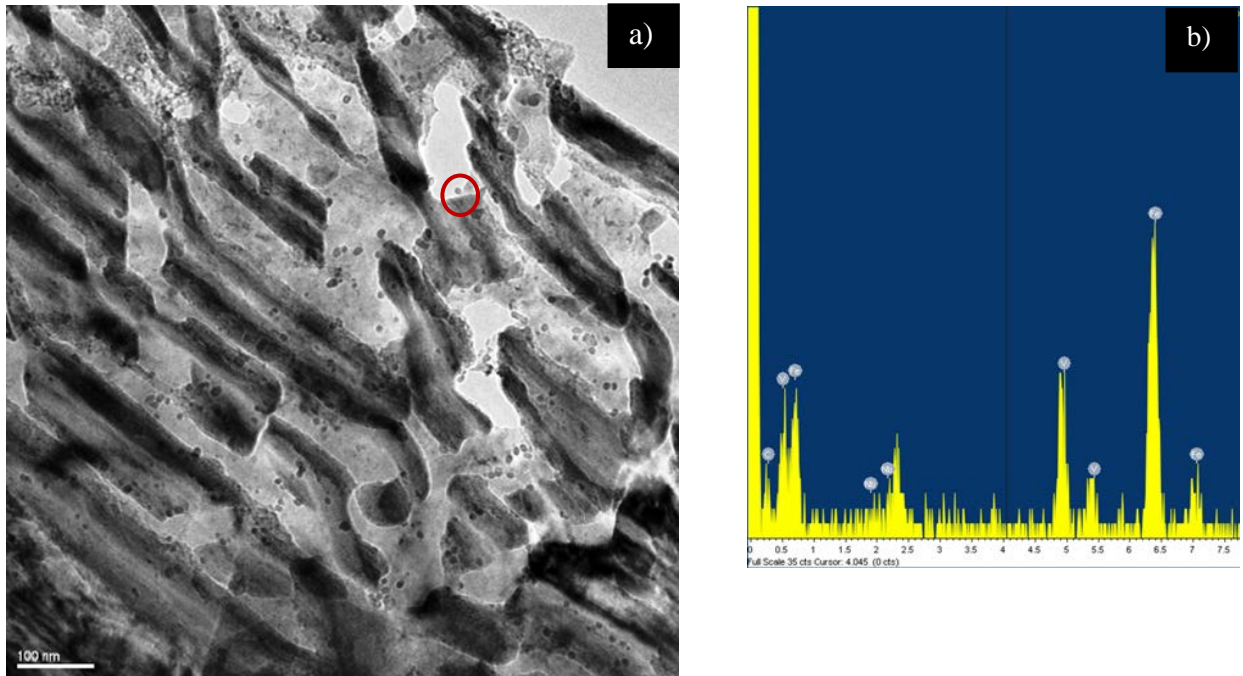


Figure 6.14 a) Bright field TEM micrographs from TMP 4 of Rsteel2, b) EDX spectrum from the encircled precipitate

Another TEM micrograph of the sample after TMP 4 is shown in Figure 6.15. It is important to point out the large presence of these precipitates. The EDX spectrum indicates that not only vanadium is present in these precipitates but also elements like molybdenum and niobium.

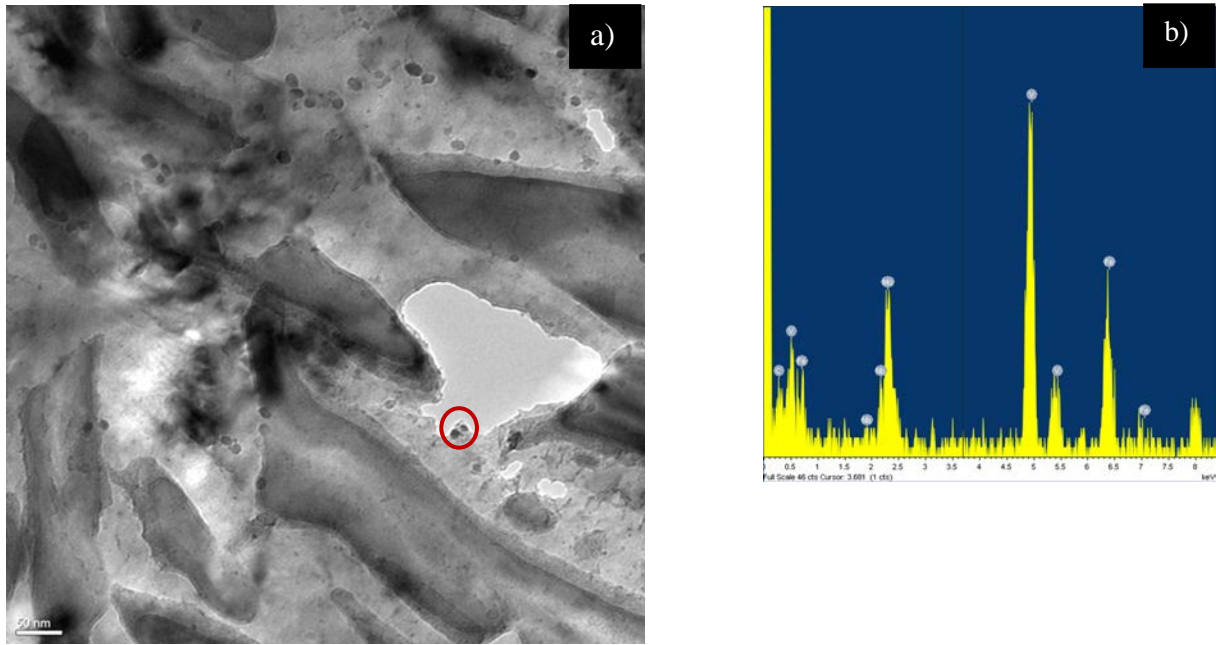


Figure 6.15 a) Bright field TEM micrographs from TMP 4 of Rsteel2, b) EDX spectrum from the encircled precipitate

The TEM characterization of TMP 3 indicated that no precipitation on pearlitic ferrite happened on this sample. It seems that the kinetics of precipitation of these particles requires longer times at this temperature. The hardening contribution associated with solid solution of different elements such as molybdenum, niobium and vanadium in the ferritic matrix is still available because no precipitates of these elements were observed. Figure 6.16 shows the examples of bright field TEM micrographs.

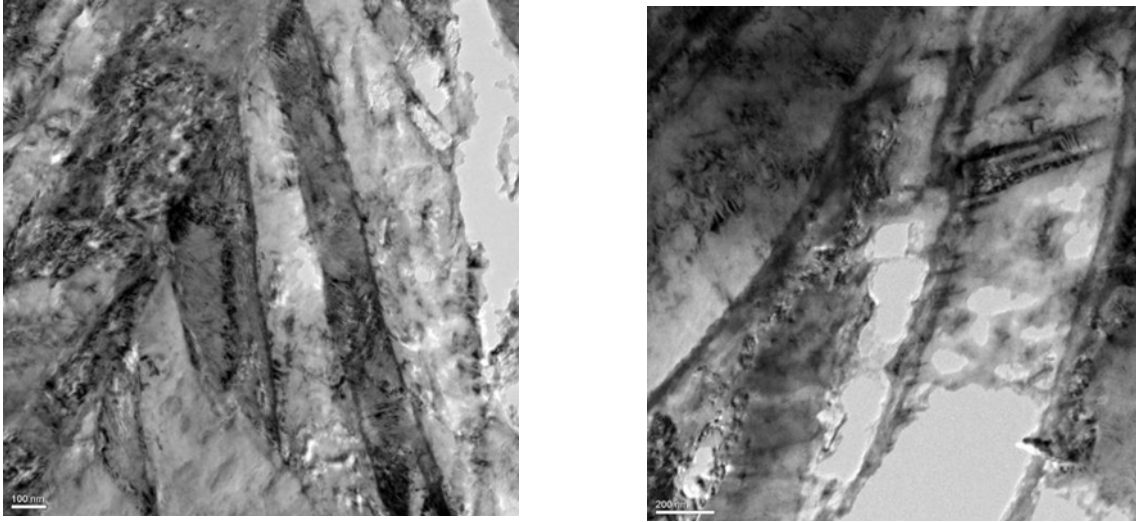


Figure 6.16 Bright field TEM micrographs from TMP 3 of Rsteel2

The small hardness differences between these two experiments can be explained by the precipitation of carbides (V, Mo, and Nb) within the pearlitic ferrite. These precipitates maintain the hardness (hardening effect) in sample 3 even after a longer time of isothermal treatment. On the other hand, the precipitation process depleted the concentration of these elements on the pearlitic ferrite diminishing the contribution of solid solution on strengthening, which did not occur in sample 4. This would explain the fact that in TMP experiment 3, no carbide precipitation was registered but the solid solution contribution on strengthening is still active.

6.2.3 Rsteel3

In the TMP of Rsteel3, many experiments developed effectively fully a pearlitic microstructure. TMP 3 and 4 had the same deformation path, cooling and isothermal temperature but with different holding time (20 and 100min). A behavior similar to that in Rsteel2 was observed in these samples, that means that carbide precipitation took place in TMP 4 after a longer isothermal treatment which maintains the hardness. The TMP 5 developed a coarse pearlite which is unfavorable and most likely responsible for the low mechanical properties.

In TMP 8 and 9, the final deformation amount was larger (70%) but with a different isothermal path. In the case of TMP 8, the isothermal treatment was carried out at 600C for 15minutes. Evidently, the isothermal temperature was too high to develop a fine interlamellar spacing, which clarifies the difference in interlamellar spacing and hardness between these two TMP experiments.

Although the hardness of TMP 3 and 9 had similar hardness values (37.3 and 39.3 HRC, respectively), the interlamellar spacing was smaller in the case of the sample with lower hardness (from these two), contrary to all the work done from other investigators. This behavior can be explained by an additional strengthening contribution of a different source. A TEM characterization was carried out on samples 9 to verify which type of strengthening mechanism can contribute to the hardness. Figure 6.17a shows the bright field TMP micrograph of TMP 9 of Rsteel3. In this figure the presence of precipitates in the pearlitic ferrite is evident. However, its apparent volume fraction is not high. Figure 6.17b shows the EDX spectrum that indicates the presence of vanadium and molybdenum in the encircled particle. Even though TMP 3 and 9 had exactly the same isothermal path, the particle precipitation did not occur in TMP 3. The only

differences between these two thermomechanical experiments is the amount of the second deformation; TMP 3 was deformed (50%) and TMP 9 was deformed (70%).

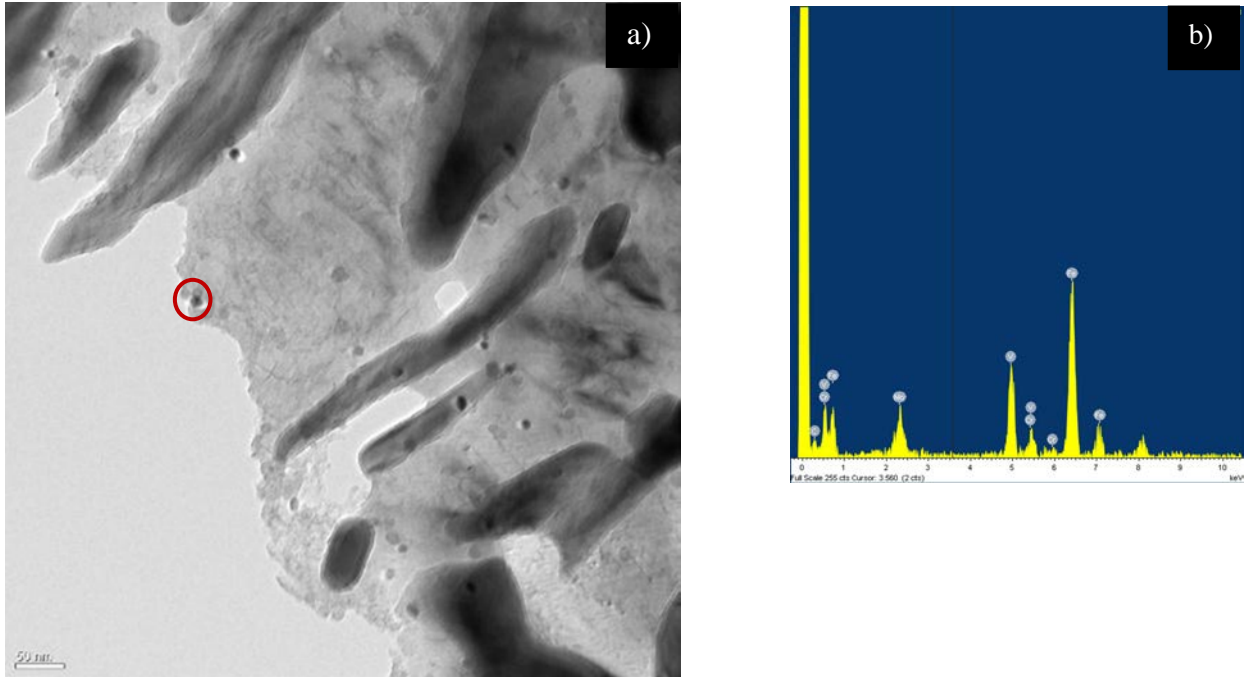


Figure 6.17 a) Bright field TEM micrographs from TMP 9 of Rsteel3 b) EDX spectrum from the encircle precipitate

It is known that deformation of austenite promotes the $\gamma \rightarrow \alpha$ transformation and intensifies the transformation [105-109]. The deformation plays a role of driving forces for this transformation. Larger strain and lower deformation temperatures stimulate the rate of this transformation. If the TMP 9 was deformed 20% more than TMP 3, this can provide the extra energy required for the precipitation of these particles.

6.3 MECHANICAL PROPERTIES

The mechanical behavior of eutectoid and hyper-eutectoid steels is largely controlled by the microstructure developed during the manufacturing processing. The microstructural features most likely responsible for the mechanical properties are pearlite colony size, prior austenite grain size and interlamellar spacing. However, other factors are also related to the mechanical properties, such as solid solution, precipitation of particles and cleanliness of the material.

6.3.1 Hardness

The hardness of the samples rolled at US Steel facilities are shown in Table 5.7. The hardness variation between them is significant. The interlamellar spacing of the samples was assessed. The average interlamellar spacing was very similar between Rsteel1 and Rtseel3 (0.095 and 0.096 μm , respectively), and slightly different with respect to Rsteel2 (0.084 μm). In accordance with the work done by Clayton and Danks, the highest hardness corresponds to the smaller interlamellar spacing. Figure 5.20 shows a comparison of the hardness values of the commercial steels and the steels developed in this research and its relation with interlamellar spacing. The three Rsteels do not follow a perfect trend described by the trending line (black). This behavior can be attributed to the presence of precipitates in the pearlitic ferrite found in the thermomechanical experiments.

6.3.2 Tensile Testing

The summary of tensile testing results is shown in Table 5.8. The Rsteel2 was the steels with the highest yield strength (1095.6 MPa); the Rsteel 3 showed the lowest yield strength (847.4MPa). Even though the Rsteel 3 has the lowest YS of the three developed steels, its YS value is higher with respect to the commercial steels. Figure 5.22 shows the comparison of YS between commercial steels and the developed steels. The general agreement seems to indicate that the interlamellar (λ) spacing controls the yield strength. The dependence of yield strength on interlamellar spacing can be represented by the Hall-Petch relation, $YS \propto \lambda^{-1/2}$ [14,73-76, 93]. Taleff [96] summarized yield strength and interlamellar spacing data from various eutectoid and ultrahigh carbon steels. Figure 6.18 shows a reasonable correlation between the two characteristics. The red dots show the superimposed yield strength values and the inverse square root of interlamellar spacing of the developed steels.

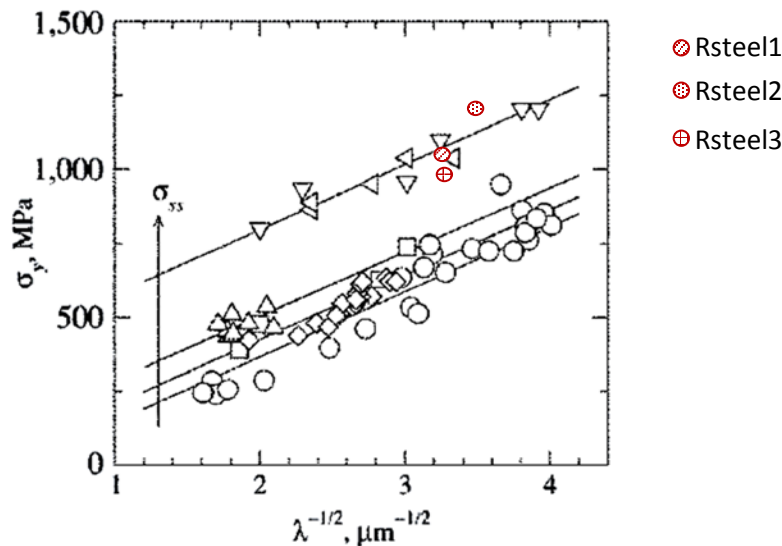


Figure 6.18 Data for yield strength of eutectoid and ultrahigh carbon steels are plotted against the inverse square root of pearlite interlamellar spacing

In accordance with yield strength and the inverse square root of interlamellar spacing values of the developed steels, there are other strengthening contributions to the yield strength. T.D. Mottishaw and G.D. Smith, working with microalloyed pearlitic steels, showed that additions of chromium and vanadium produce strength increments up to 200MN/m² under continuous cooling transformation conditions by secondary carbonitride precipitation within the pearlitic ferrite. Taleff et al., showed in ultra-high carbon steels that aluminum and chromium are strong solid solution strengtheners.

The yield strength may then be considered as the linear addition of different strengthening effects. The strengthening from interlamellar spacing (σ_λ), the solid solution strengthening (σ_{ss}), the composite strengthening (σ_c) which increases as the carbon content increases, the precipitation strengthening (σ_{pp}) and pearlite colony size strengthening (σ_{pc}). The contribution of the prior austenite grain size on yield strength has been shown not to have a substantial contribution [90] and can be considered negligible. The yield strength can be considered as in Equation 6.1.

$$\sigma_y = \sigma_\lambda + \sigma_{ss} + \sigma_{pc} + \sigma_{pp} + \sigma_c \quad (6.1)$$

Because the nature of strengthening by interlamellar spacing and the strengthening by precipitation is similar through inhibiting the dislocation motion, decreasing the slip length in ferrite they can be enclosed in one expression, $\sigma_{\lambda p}$. Eric M. Taleff, J.J. Lewandowski and Bandam Pourlandia, also combine the composite strengthening contribution and the solid solution strengthening contribution in a term called alloy strengthening (σ_0)_{ss}. Then the Equation 6.1 can be reduced to:

$$\sigma_y = \sigma_{\lambda p} + (\sigma_0)_{ss} + \sigma_{pc} \quad (6.2)$$

The observation of the pearlitic microstructure of commercial steels exhibited the presence of proeutectoid cementite, which would be detrimental to the mechanical properties [110]. This phase was not resolvable by optical microscopy neither by SEM, which suggests that yield strength was not affected negatively.

Figure 5.23 shows the comparison between the elongations of developed steels vs the elongation of commercial steels, the difference between them is remarkable. The minimum elongation value was reached by Rsteel2, which had the highest yield strength of the three steels. However, the steel with the largest elongation was the Rsteel1. The ductility of eutectoid and hyper-eutectoid steels has been associated with a larger interlamellar spacing which allows a larger dislocation glide through slip planes. Coarse pearlite possesses low strength and initially deforms by dislocation generation at ferrite/cementite interfaces [86], although the three developed steels have a substantially fine pearlite. The tensile ductility as a measured of fracture strain is independent of prior austenite grain size and pearlite colony size [73, 75, 111-116]. In materials with similar austenite grain size, generally finer interlamellar spacing exhibits a slightly larger ductility. This can be attributed to the differences in deformation behavior between fine and coarse pearlite [95]. Other authors have attributed the increment of ductility in finer pearlite to the fact that finer pearlite produces also thinner cementite lamellas which are more susceptible to deformation as they may rupture by necking rather than failing in a brittle manner [85, 112,117].

6.3.3 Fracture Toughness

The fracture toughness of a material is its resistance to crack propagation or its ability of the material to absorb energy in the plastic deformation range. It is a measure of the energy to resist fracture. Fracture toughness in steels is dependent on numerous factors which influence the mechanical properties, such as temperature, chemical composition, microstructure, grain size, strain rate etc. Table 5.9 shows the results of fracture toughness evaluation of the two steels with larger yield strength. Hyzak and Bernstein [73], working with fully pearlitic steels, concluded that toughness as measured by both the Charpy transition temperature and the dynamic fracture toughness is a strength inverse function of the prior austenite grain size, with a considerable influence of the interlamellar spacing. The fracture toughness (obtained using chevron-notch samples) results from hyper-eutectoid carbon steels, have shown an increase in toughness with decreasing the austenite grain size [118]. Figure 6.19 compares these results to these of the steels developed by this research.

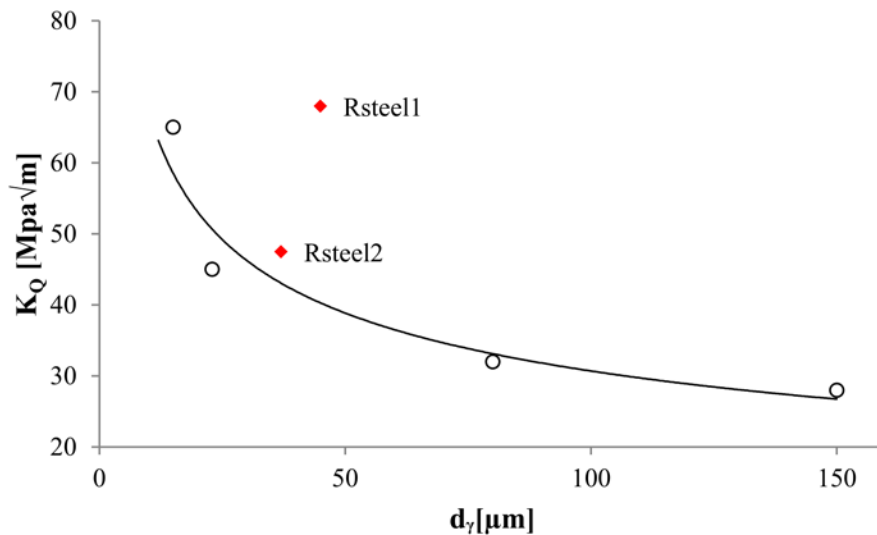


Figure 6.19 Comparison of results from ultra-high steels [118] and the developed steel

These results suggest that there is something else that contributes to toughness resistance. This can be explained by the lack of proeutectoid phase on the developed steels. The presence of the proeutectoid phase in eutectoid and hyper-eutectoid steels has been considered deleterious to the mechanical properties; its presence decorating the austenite grain boundaries reduces the cohesive forces between austenite grains producing nucleation sites for cleavage fracture. Other researchers [94,95-119,120], have shown that cleavage fracture stress of fully pearlitic steels increases with a decrease of pearlite interlamellar spacing.

Therefore, the best microstructure to increase the toughness of eutectoid steels should have a combination of small austenite grain size, not very fine interlamellar spacing, and the grain boundaries should be free of particle networks. Inclusions should be avoided to preserve high toughness since they readily debond. Large, widely spaced inclusions usually are less damaging than finely spaced inclusions where inclusions are weakly bonded to the interface.

6.4 WEAR TESTING

The major objective in the development of new rail materials is improving both wear resistance and the mechanical properties. Traditionally, the main method to reach this objective was through increasing the initial bulk hardness of the steels, which was accomplished by raising the carbon content. Over the years, a relationship between hardness and wear of rail steels has been observed [83,121]. Other microstructures like martensite and/or bainite have higher hardness levels than the fully pearlitic microstructure. However, they are not extensively used in commercial rail roads. Therefore, there should be some other parameters that modify the wear behavior in steels. Robles Hernandez [122], working with premium rail steels, suggested that the

differences in work hardening between the bainitic rail steel and the premium rails with pearlitic microstructure could be the reason for better wear resistance of the pearlitic steels. Results of wear testing of the developed steels in this study are shown in Table 5.10. One important finding of this test was the fact that no change in weight was registered in the disks used during the testing. This can be attributed to the low Hertzian load used in this test, or due to the behavior of the material to resist wear. Figure 5.29 shows the typical profile of the disk at the end of the wear testing; this profile suggests that the relocation material goes to the edge of the groove. This profile is also shown in Figure 6.20. This figure shows a three dimensional representation of the groove generated. The color degradation (from blue to red) shows the differences in groove depth. The black arrows point out the relocated material that was displaced from the center of the groove (blue center area). Because there was not material lost during the testing, the material displaced and the material relocated must be the same.

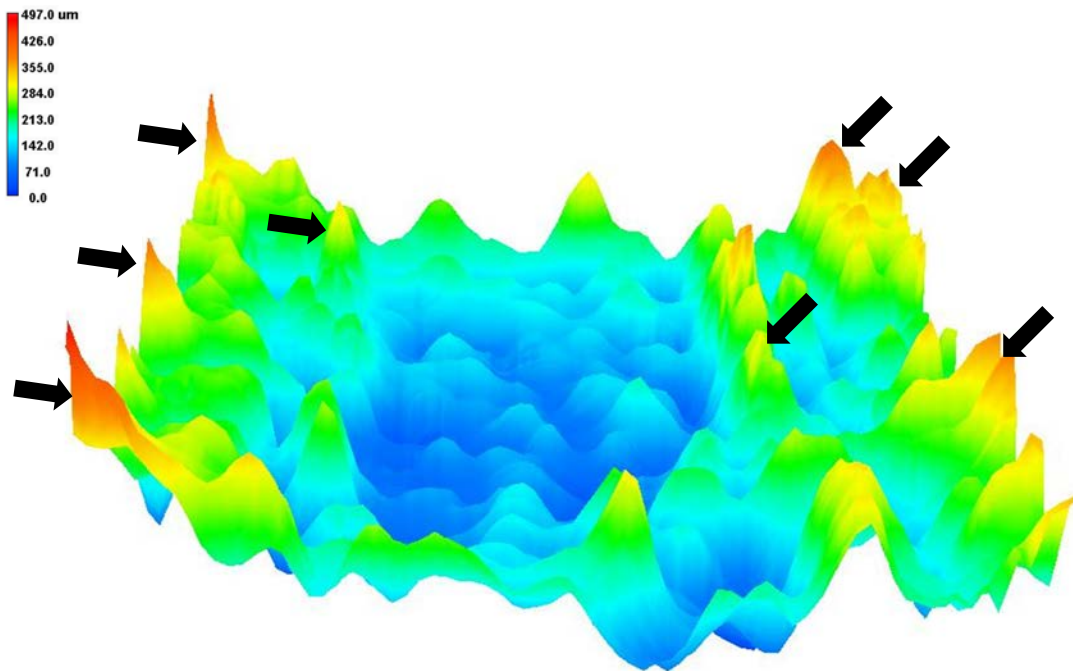


Figure 6.20 Three dimensional representation of the groove generated

The conservative principle of the material is used to explain this behavior. Figure 5.29 shows, schematically, the profile of the groove and the suggested behavior. A and B represents area of the transverse section of the peaks where the material relocated and C is the area of the transverse section of the groove generated, therefore $A + B = C$.

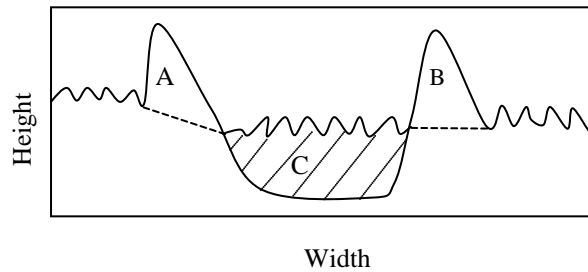


Figure 5.29 Schematic representation of the material relocation process during wear testing

Initially, the material flows from the contact area of the disk and the pin to the edges of the pin (a). Later, as the test progresses, the material from the center of the initial channel flows to the bottom of the incipient peak (b). The channel becomes a groove through the continuous flow of material to the bottom of the previous material producing more strain (c). This process occurred repeatedly until the hardness of the material at the bottom of the groove reaches the hardness of the

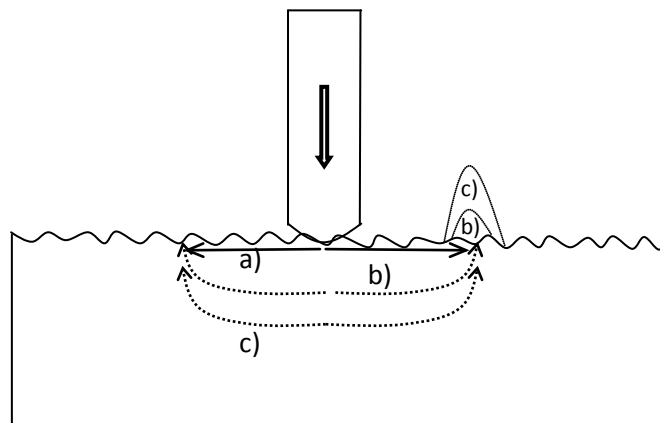


Figure 6.21 Schematic representation of wear processes suggested

pin throughout work hardening processes. Afterwards, the relocated material at the highest point of the peak must be higher than the material at the bottom. Therefore, the work hardening plays an important role on wear resistance. During each cold plastic deformation, a part of forming energy is transformed to heat and/or to strain hardening of steel. The material hardness increases and the load required to produce a plastic deformation needs to be higher. If the load used to induce the plastic deformation does not increase, then the material reduces the wear rate, until wear is no longer induced in the material. This process explains the wear behavior described by the material in Figure 6.21.

6.5 ISOTHERMAL TRANSFORMATION STUDIES

The transformation of pearlite in steels involves the cooperative, diffusional growth of ferrite and cementite from austenite. The practical nature of the information obtained from a series of isothermal reaction curves makes them very important to study.

Figure 5.32 and 5.33 show the fraction of pearlite transformed as a function of time for different temperatures of commercial steel D and Rsteel2, respectively. From these reaction curves the time required to begin the transformation and the time required to complete the transformation can be obtained. In the case of commercial steel D, the pearlitic transformation starts slightly sooner than in Rsteel2. This suggests that the incubation period in Rsteel2 is longer than that in the commercial steel D. For longer time (120s), the Rsteel2 still experiences a slow kinetics of transformation with a pearlite volume fraction approximately 0.2 with the exception for the isothermal temperature of 550C which almost reaches 0.4. The commercial steel D exhibited a different behavior. The transformation reached after 120s was approximately 0.4 in most of the isothermals. The end of transformation was taken as the time required to transform 0.99 of the volume fraction, as commonly is done in different studies. Apparently, the shape of the transformation curves follows the classical nucleation and growth model suggested by Johnson and Mehl, Equation 2.1 [52].

Figures 5.34 and 5.35 show the reconstruction of TTT diagrams from commercial steel D and Rsteel2, respectively. One of the significant factors about the pearlite transformation is the primarily precipitation of proeutectoid cementite along grain boundaries in the commercial steel D. This precipitation took place at very short times, even before the primarily nuclei of pearlite. This proeutectoid phase has been documented in different steels [103,104,110,122] and

it has a detrimental effect on mechanical properties. However, contrary to what happened in commercial steel D, the proeutectoid phase was not precipitated in Rsteel2. Another important difference is the time of the beginning of transformation between the two steels. Because of the nucleation of the pearlite occurred at grain boundaries, the slow incubation process in Rsteel2 can be explained by a larger prior austenite grain size; nevertheless, contrary to this, the prior austenite grain size of Rsteel2 is smaller than the one in commercial steel D. Therefore, other features must affect the kinetics of transformation of the pearlite. Han and Mottishaw [110], working with hyper-eutectoid steels showed that additions of vanadium results in the formation of discrete grain boundary cementite particles rather than a continuous network along the grain boundaries. Because Rsteels2 contains silicon, chromium, and molybdenum, these elements decrease the eutectoid carbon content; therefore it might be expected to exhibit hyper-eutectoid behavior [104]. However, in hyper-eutectoid steels containing vanadium and silicon, the reverse behavior occurred. No grain boundary cementite was resolvable and the pearlitic microstructure was predominantly lamellar. This can explain the behavior of Rsteel2 in which proeutectoid cementite was not observed.

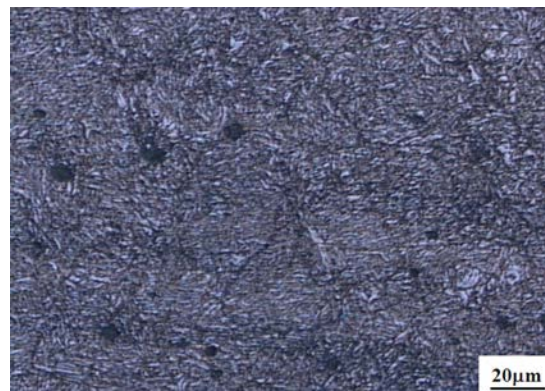
7.0 CONCLUSIONS

- The eutectoid steels developed in this research successfully exceeded the mechanical properties desirable for optimum wear performance.
- The mechanical properties of eutectoid steels seem to be controlled by microstructural features such as interlamellar spacing, pearlite colony size and prior austenite grain size.
 - Hardness is strongly influenced by interlamellar spacing
 - The yield strength is dependent not only on the interlamellar spacing but also on the effect of hardening by precipitation and solid solution hardening.
 - The improvement of elongation is controlled by two main contributions the refinement of austenite grain size as well as the thinning of cementite lamellae.
 - The proeutectoid cementite that has a detrimental effect on toughness was not observed in the developed steels.
- The wear behavior of the developed steels is controlled not only by the hardness or interlamellar spacing but also by the differences between the yield strength and the tensile strength (work hardening).
- The pearlite transformation kinetics was affected mainly by the addition of alloying elements and a lesser degree by the austenite grain size.

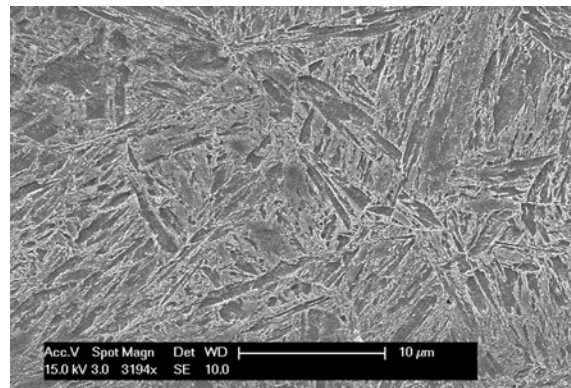
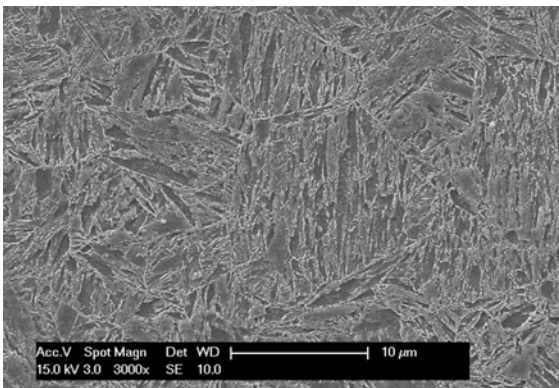
APPENDIX A

A.1 RAIL STEEL1, MICROSTRUCTURES GENERATED BY THERMOMECHANICAL PROCESSING

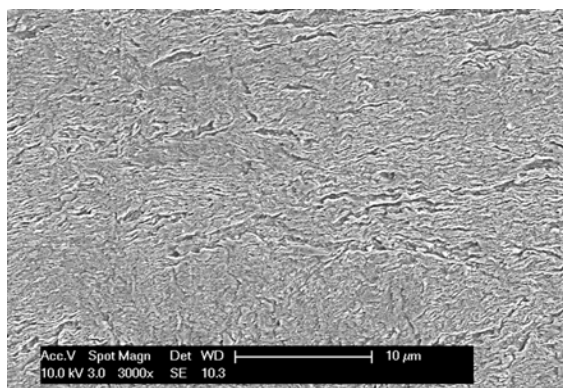
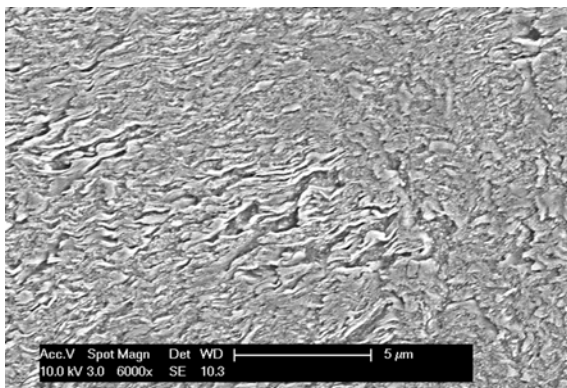
Thermomechanical experiment number 1



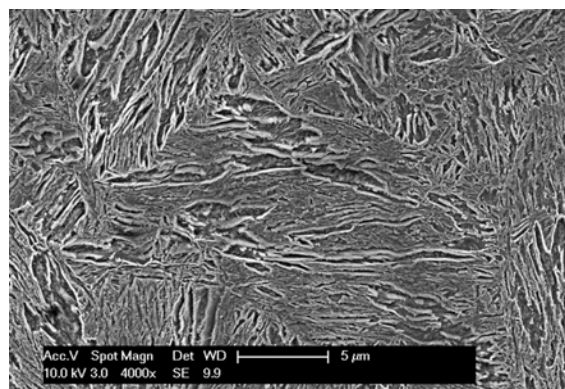
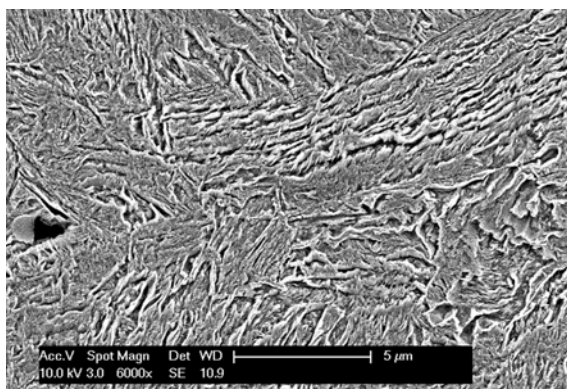
Thermomechanical experiment number 2



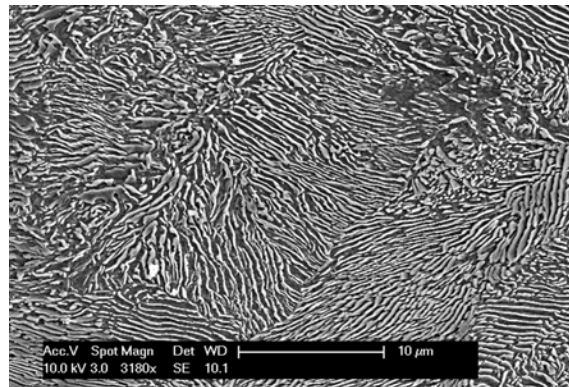
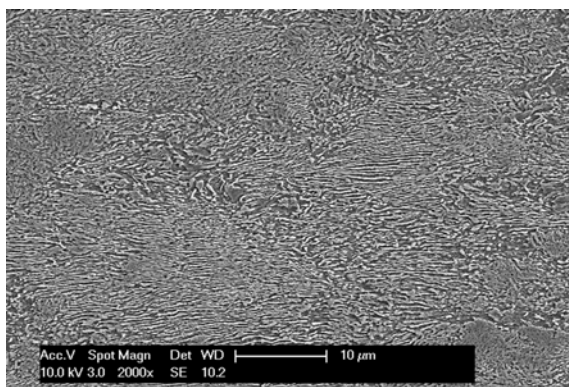
Thermomechanical experiment number 3



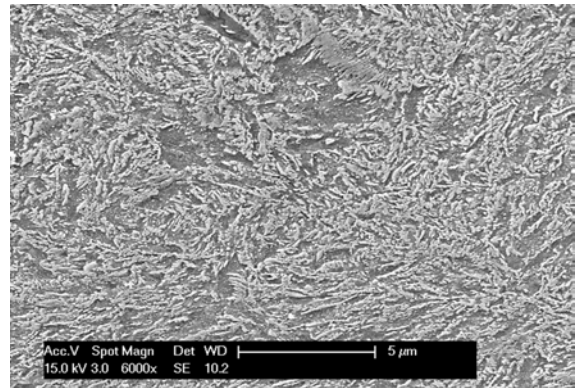
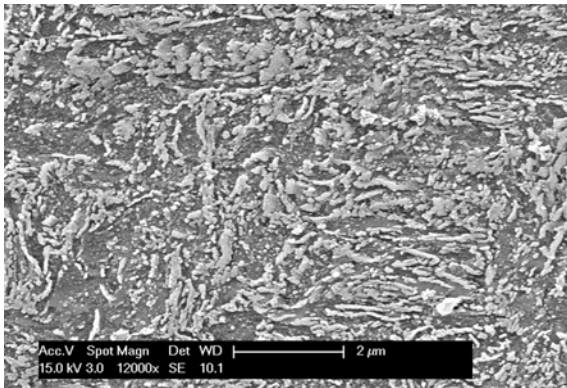
Thermomechanical experiment number 4



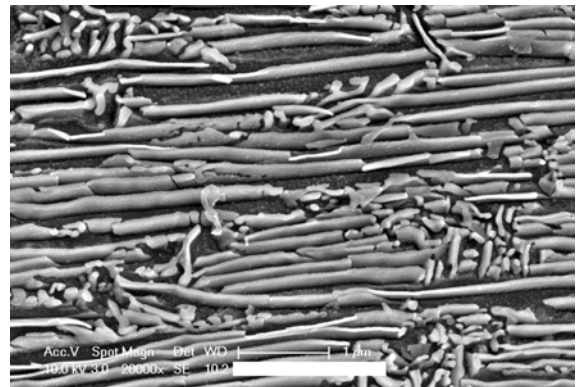
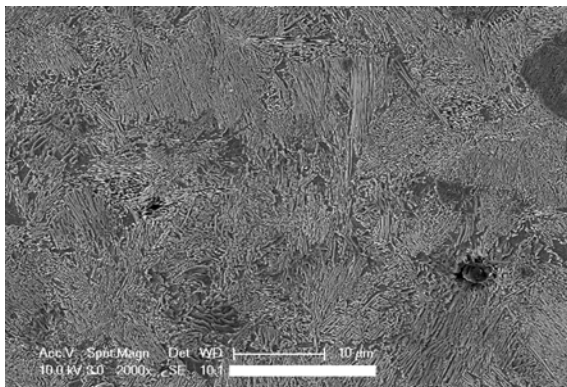
Thermomechanical experiment number 5



Thermomechanical experiment number 6



Thermomechanical experiment number 7

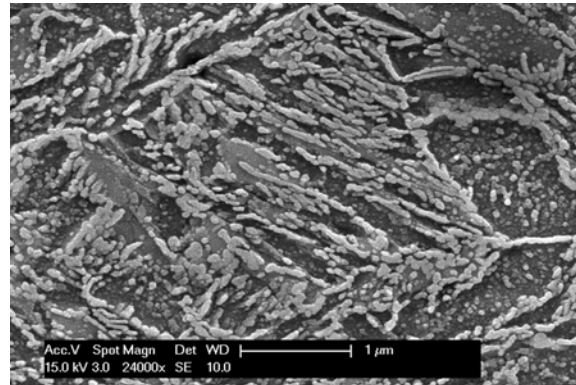
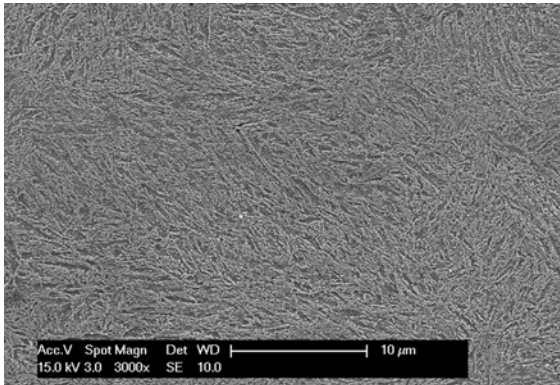


A.2 RAIL STEEL2, MICROSTRUCTURES GENERATED BY THERMOMECHANICAL PROCESSING

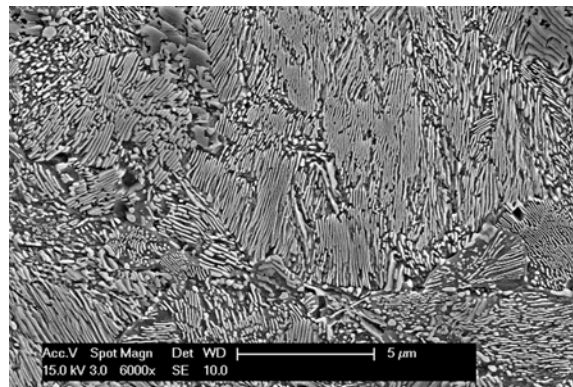
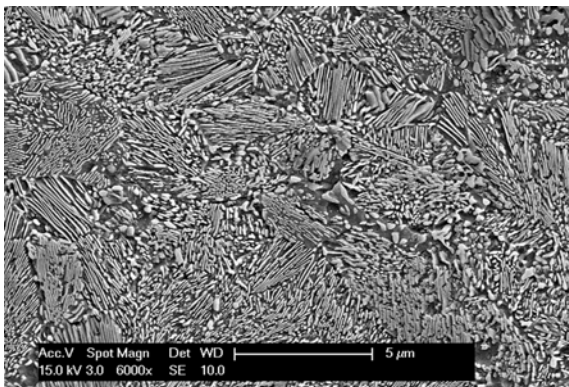
Thermomechanical experiment number 1



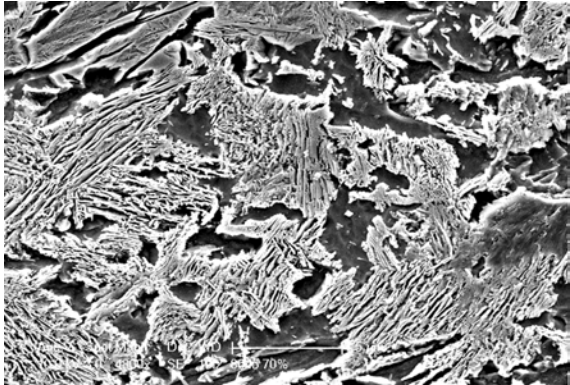
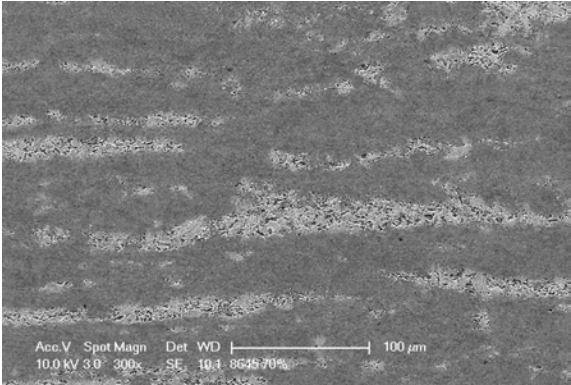
Thermomechanical experiment number 2



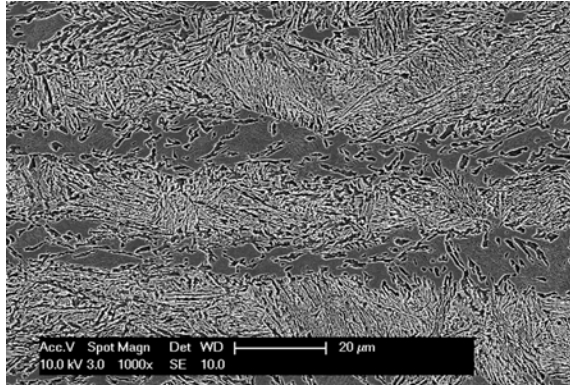
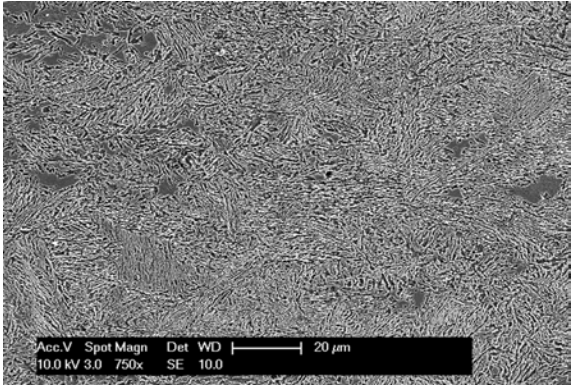
Thermomechanical experiment number 4



Thermomechanical experiment number 5

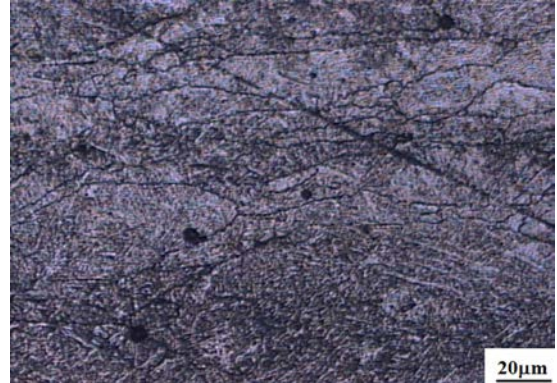
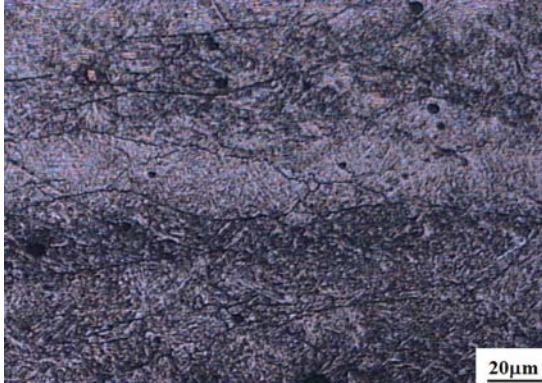


Thermomechanical experiment number 6

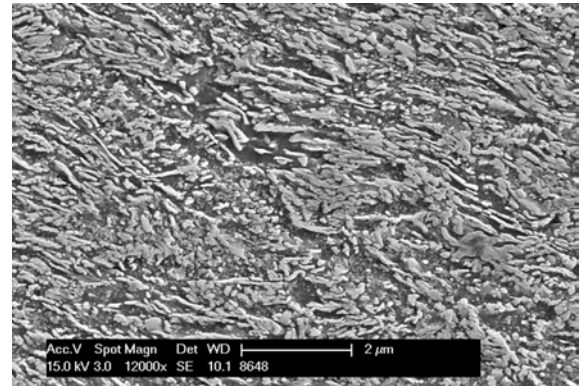
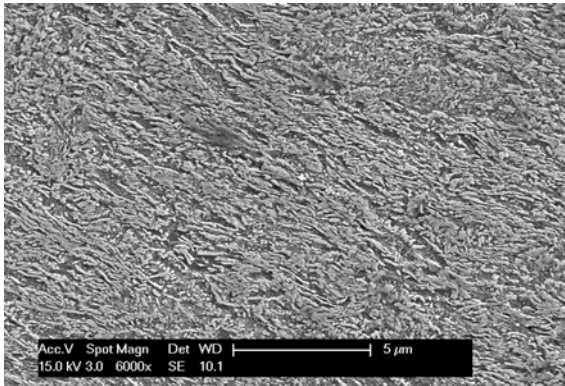


A.3 RAIL STEEL3, MICROSTRUCTURES GENERATED BY THERMOMECHANICAL PROCESSING

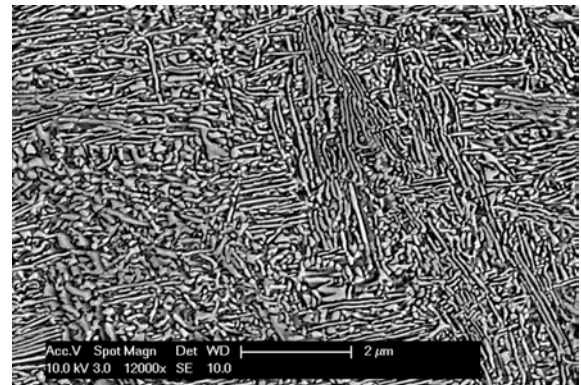
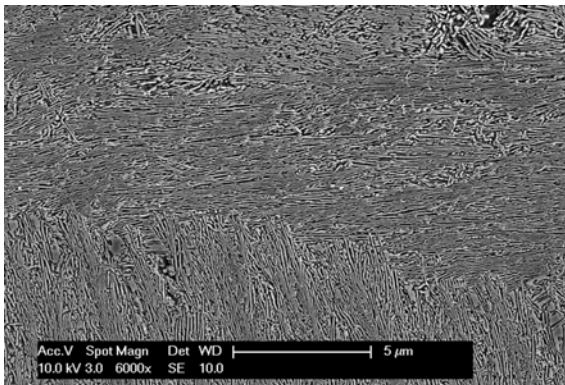
Thermomechanical experiment number 1



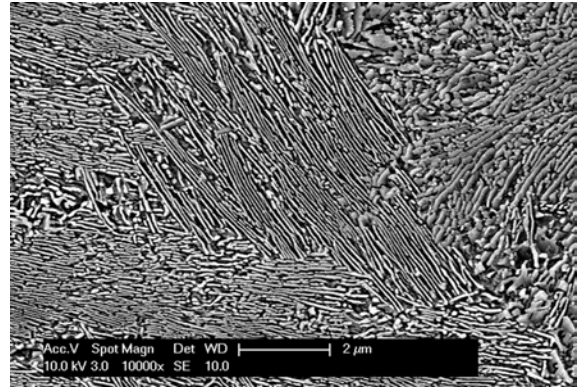
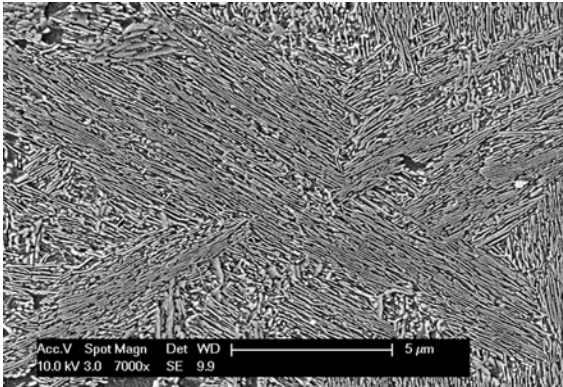
Thermomechanical experiment number 2



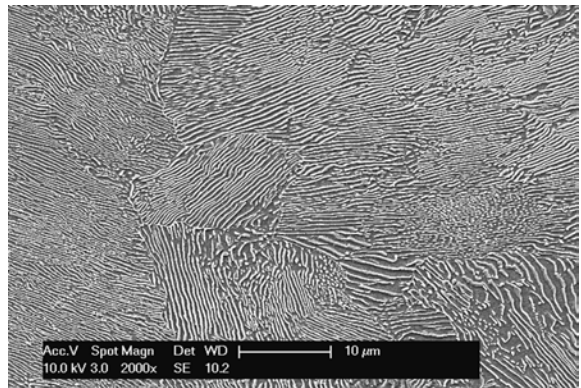
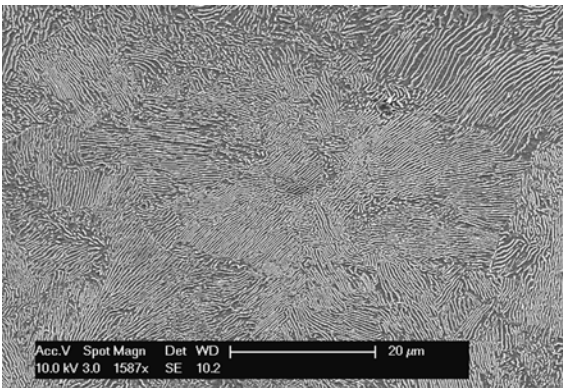
Thermomechanical experiment number 3



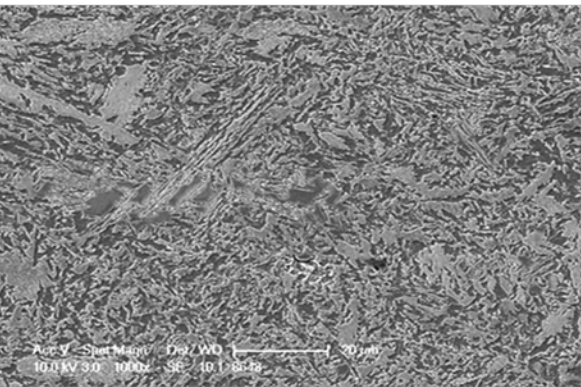
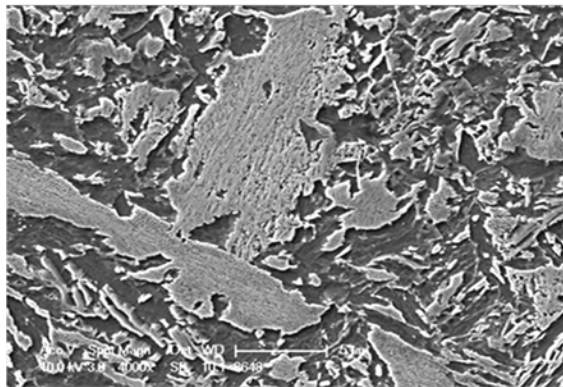
Thermomechanical experiment number 4



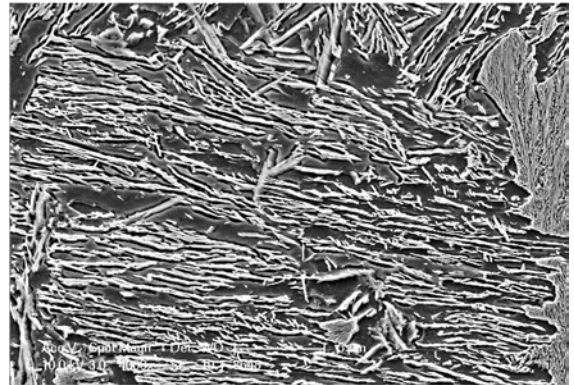
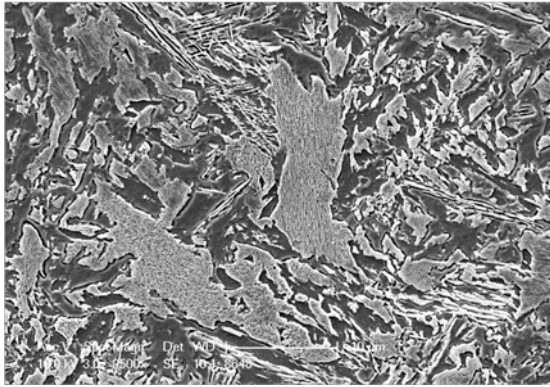
Thermomechanical experiment number 5



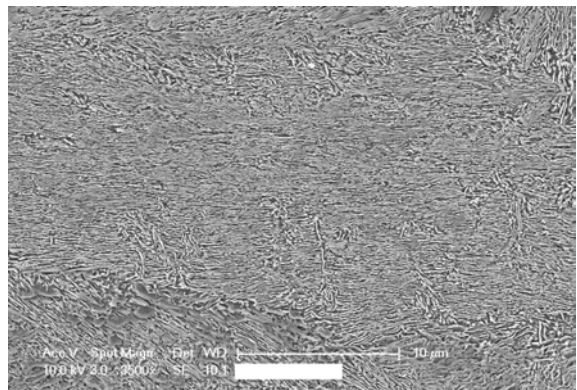
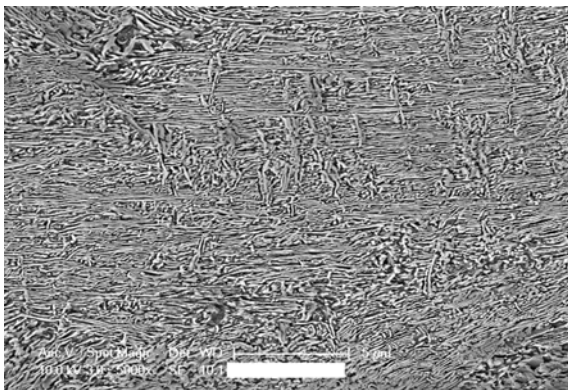
Thermomechanical experiment number 6



Thermomechanical experiment number 7



Thermomechanical experiment number 8

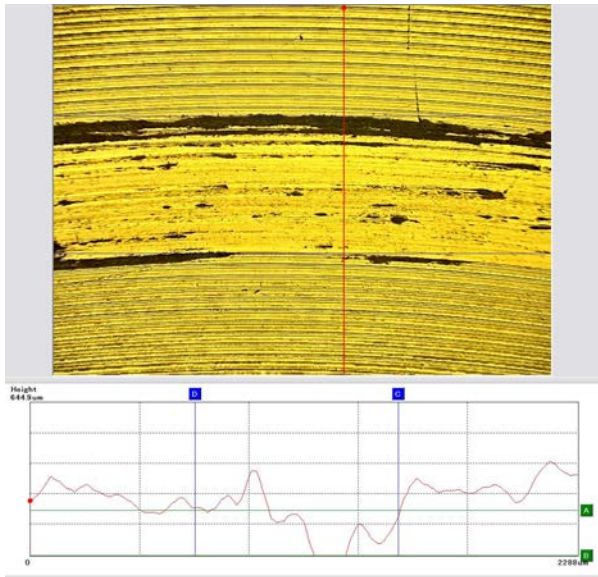


APPENDIX B

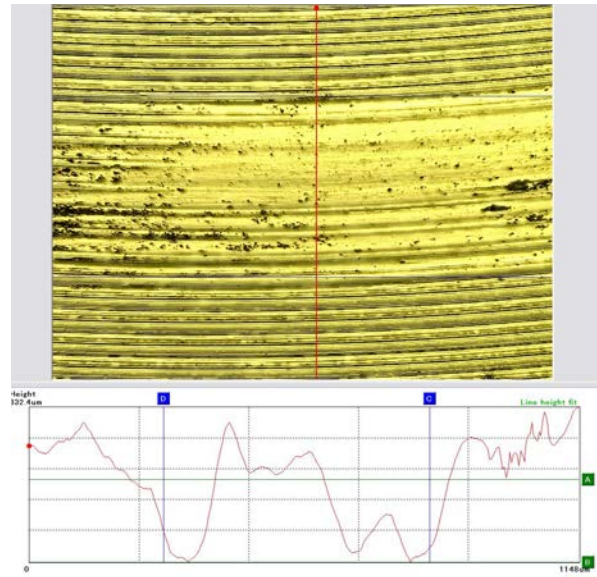
B.1 MICROGRAPHS OF THE GROOVE GENERATED AFTER 10,000 CYCLES IN DIFFERENT LOCATIONS FOR THE RAIL STEEL DEVELOPED

Rail steel 1

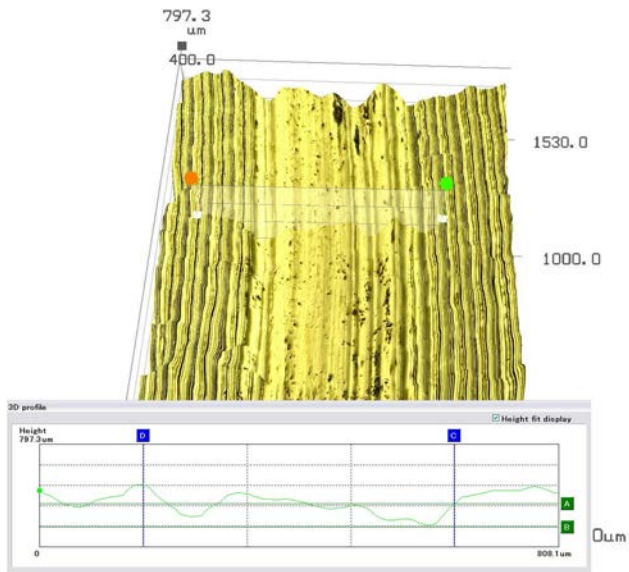
Location A



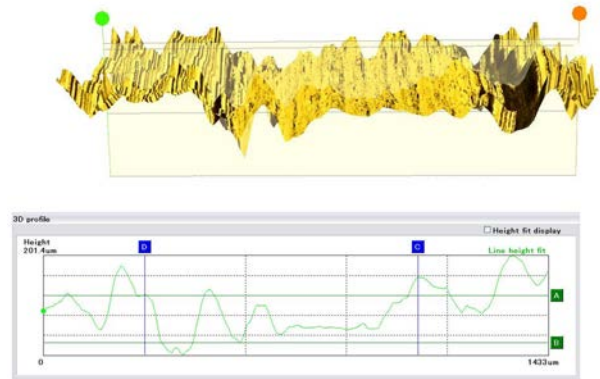
Location B



Location C

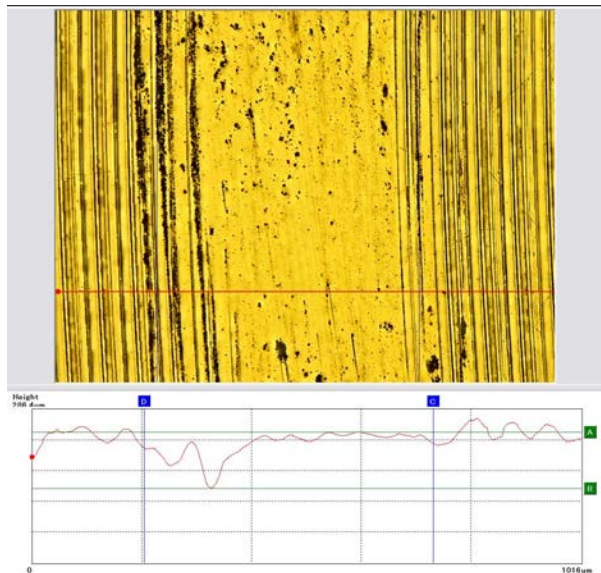


Location D

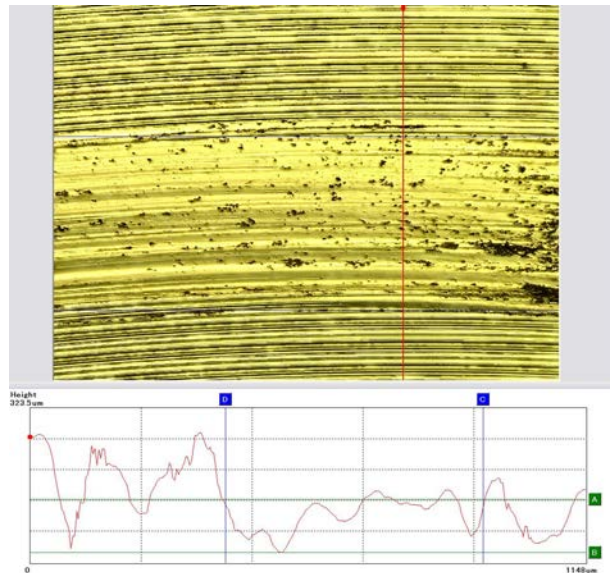


Rail steel 2

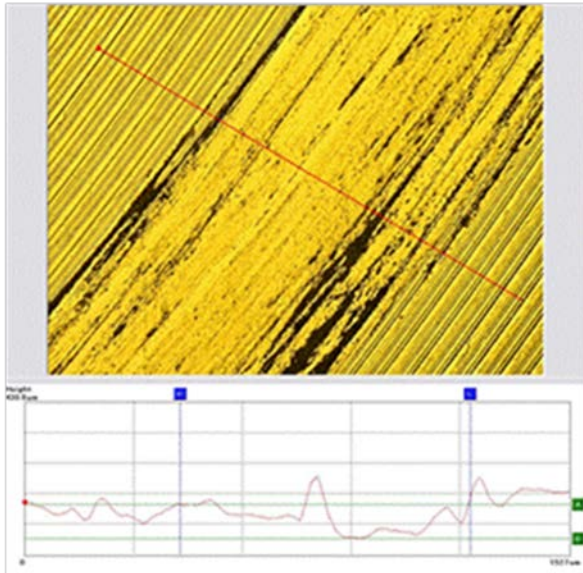
Location A



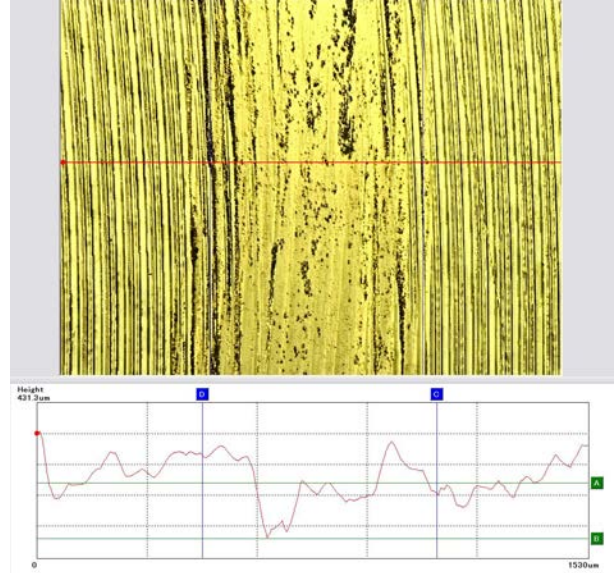
Location B



Location C

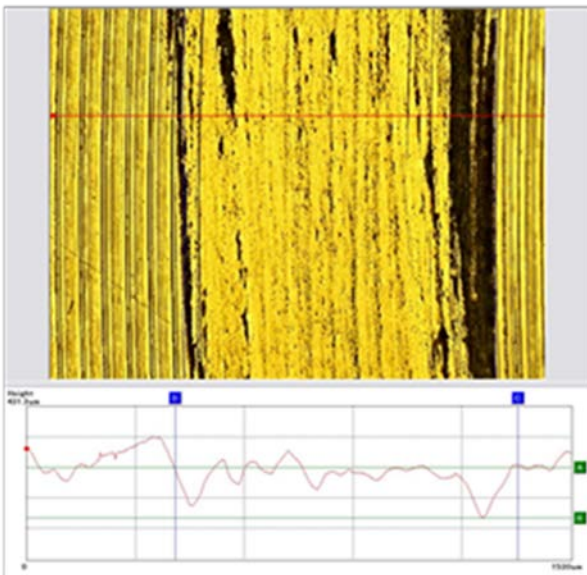


Location D

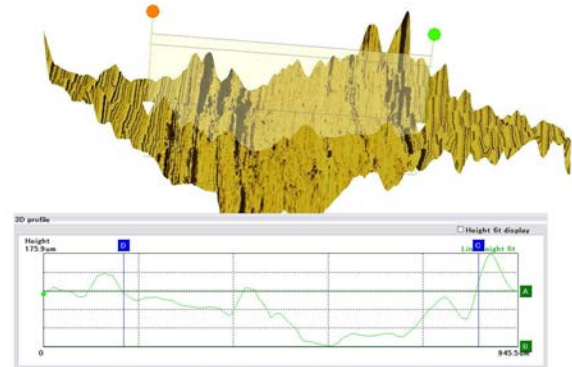


Rail steel 3

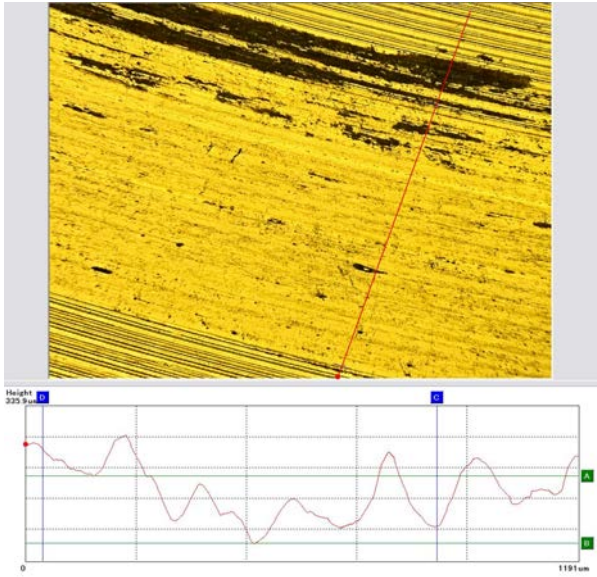
Location A



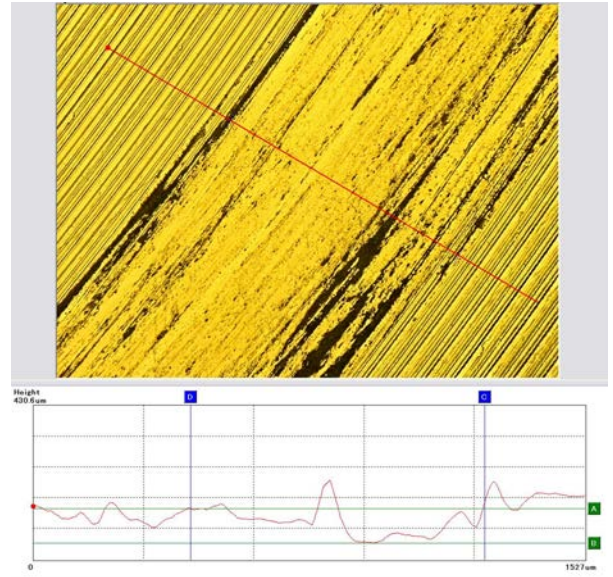
Location B



Location C



Location D



BIBLIOGRAPHY

- [1] Association of American Railroads (1999) Rail Road Facts, 1999 Edn, Washington D.C.
- [2] K. Sawley and J. Kristan (2003) Development of bainitic rail steels with potential resistance to rolling contact fatigue. National Research Council, Centre for Surface Transportation Technology, Ottawa, Ontario, K1V5S2, Canada
- [3] W.G.M.F. Gomes, L.H. Almeida, L.C.F.C. Gomes, and I.L. May, Materials Characterization, vol. 39, 1997, pp.1-14.
- [4] J.H.Martens, and D.P. Wirick, Proceedings of international Symposium on Rail Steels for 21st Century, Iron and Steel Society,.Warrandale, Pa., 1995, p 1-3.
- [5] Ya. Rausin, M. Noskov, E. Shur, Design strength of steels operating at cyclic load, Phys. Metall. Heat Treat. Met. 9, 1969, pp. 20 Russia
- [6] E. Shur, et al., Some problems of contact fatigue strength of steels, Phys. Metall. Heat Treat. Met. 8 1978, pp. 37-43, Russia
- [7] R. Ordonez, C. Isaac Garcia, Semih Kalay and Anthony J. DeArdo, Development of High Performance Steels for Rail Applications, ASME 2010 Joint Rail Conference, 2010.
- [8] R.K. Steele Rail Quality and Maintenance for Modern Railway Operation , International Conference, Delft 1992, Kluwer Academic Publishers, Dordrecht, Netherlands, 1993, p 77-97
- [9] H.K.D.H Bhadeshia (2002), Steel for Rails. Encyclopedia of Material Science and Technology .
- [10] Heshmat A. Aglan (2006), “Fatigue Damage Tolerances of Bainitic and Pearlitic Rail Steels”, International Journal of Damage Mechanics, Vol 15 Octobre 2006.
- [11]. D.F.Cannon, E.O.Edel (2003) “Rail Defects: An overview, Fatigue & Fracture of Engineering Materials & Structures”, Vol 26, October 2003.
- [12] Yong-Jin Park and I.M. Bernstein (1978) Mechanism of Cleavage Fracture in Full Pearlitic 1080 Rail Steel, Rail Steels-Developments, Processing and Use, ASTM STP 664.

- [13] G.K. Bouse, I.M. Bernstein and D.H. Stone(1976), “Role of Alloying and Microstructure on the Strength and Toughness of Experimental”, Rail Steels. Symposium on Rail Steels. ASTM, Denver, Colorado, November 17-18 1976.
- [14] Eric M. Taleff, et al., “Pearlite in Ultrahigh Carbon Steels: Heat Treatments and Mechanical Properties” Metall Mater Trans A, 27A (1) (January 1996), pp. 111-118.
- [15] G. Krauss, “The Microstructure and Fracture of a Carburized Steel”, Metall. Trans. A, 1978, vol. 9A, p. 1527.
- [16] Masaharu Ueda, Koichi Uchino (2000) Development of hypereutectoid steel Rails for Heavy Jul Railways. 6Th International Heavy Haul Conference.
- [17] H.Ridley, Met Trans., vol 16A, 1984, pp. 1019-1036.
- [18] H.Ridley, in Proceeding of the International Conference on Phase Transformations in Ferrous Alloys, eds. A .R. Marder and J.I. Goldstein, TMS-AIME, Warrendale Pa, 1984, pp. 201-236.
- [19] K. Sawley and Scholl, M (1998) “The development of bainitic steels”, In Proceedings of the 39th MWSP Conference, ISS, Vol. 35, pp. 1007-1014.
- [20] H.K.D.H Bhadeshia (1992) Bainitic Steels, The Institute of Materials, London, England.
- [21] Yokoyama, H., Mitao, S., Yamamoto, S. and Fujikake, M. (2000) Effect of angle of attack on flanking behavior in pearlitic and bainitic steel rails. CM200. In: MC2000 Proceedings of the Fifth International Conference on Contact Mechanism and Wear of Rail/Wheel Systems, Tokyo. pp. 154-160.
- [22] Ghonem, H., Kalousek, J. and Stone, D. (1982) “Fracture and wear characteristics of Cr-Mo bainitic steel”, Specialty Steels and Hard Materials, Pergamon Press, Oxford.
- [23] Heller, W. and Schweitzer, R. (October 1980) “High Strength pearlitic steel does well in comparative tests against bainitic steels”, Railway Gazette International 855-857.
- [24] H. Ichinose, J. Takehara, and M. Ueda, “High strength rail produced by two stages flame heating and slack quenching”, 2nd International, Heavy Haul Railway Conference, Colorado Springs, Co., 1982, 178-186.
- [25] Clayton, P., Sawley, K. J., Bolton, P. J. and Pell, “Wear behavior of bainitic steel”, Wear vol 120, Issue 2, 1987, 199-220.
- [26] H. K. D. H. Bhadeshia, “Steels for Rails”, Encyclopedia of Materials Science and Technology, 2002, pp. 1-7, Elsevier Science.

- [27] H. A. Aglan, Z. Y. Liu, M. F. Hassan and M. Fateh, Mechanical and fracture behavior of bainitic rail steel, *Journal of Materials Processing Technology*, Vol., 151, 2004, pp 268-274.
- [28] J. Pacyna, “The Microstructure and Properties of the New Bainitic Rail Steels” *Journal of Achievements in Materials and Manufacturing Engineering*, vol 28, Issue 1, May 2008.
- [29] J.K. Chen, C.W. Spencer, M.E. Ekstrand, G. Chen, and W.T. Reynolds Jr, “Eutectoid decomposition in Ag-Ga”, *Metall Mater Trans.A*, vol 27, 1996, pp. 1683-1689.
- [30] A.M. Elwazri, P. Wanjara, S. Yue, “The effect of microstructural characteristics of pearlite on the mechanical properties of hypereutectoid steel”, *Materials Science and Engineering A* 404 (2005) 91–98.
- [31] M. Hillert, in “The Decomposition of Austenite by Diffusional Processes”, eds. V.F.Zackay and H.I. Aaronson, Interscience, New York, 1961, pp 197-237.
- [32] D.A. Porter and K.E. Easterling “Phase Transformations in Metals and Alloys”, 2nd edition.
- [33] E.M. Taleef, C.K. Syn, D.R. Lesuer, and O.D. Sherby, *Thermomechanical Processing and Mechanical Properties of Hyperuetectoid Steels and Cast Irons*, eds. D.R. Lesuer, C.K. Syn and O.D. Sherby, TMS, Warrendale, Pa., 1997 pp. 127-141.
- [34] J.D. Verhoeven and E.D. Gibson, “The Divorced Eutectoid Transformation in Steel”, *Met. Trans.*, vol. 29A, 1998, pp. 1181-1189.
- [35] D.L. Lee and C.G.Park, “Sequential branching by ledge migration for the sidewise growth of pearlite”, *Scripta Metall.*, vol 32, no. 6, 1995, pp. 907-912.
- [36] Zener C.,”Kinetics of Decomposition of Austenite”, *Trans AIME* 1946;167:550–595.
- [37] Hillert M. Jerkont Ann “The role of interfacial energy during solid state phase transformation, *Jerkont. Ann.* 141, 1957, 757–789.
- [38] Hillert M. “On the theories of growth during discontinuous precipitations”, *Met Trans* 1972;3:2729–2741.
- [39] J.R. Vilella, G.E. Guellich, and E.C. Bain, *Trans. ASM*, vol. 24, 1936, pp. 225-252.
- [40] M. Hillert, *Mechanism of Phase Transformation in Crystalline Solids*, Monograph no.33, Institute of Metals, Londo, 1968, pp. 231.
- [41] H.K. DH Bhadeshia, R.W.K. Honeycombe, “*Steels: Microstructure and Properties*” Second Ed.

- [42] J.M.Shapiro and J.S.Kirkaldy, "Theory of decomposition of eutectoids assuming local equilibrium and phase boundary diffusion", *Acta Metall.*, vol. 16, 1968, pp. 579-585.
- [43] B.E.Sundquist, "The edgewise growth of pearlite", *Acta Metall.*, vol.16, 1968 pp. 1413-1427.
- [44] M. Hillert, in *Proceedings of International Conference on Solid – Solid Phase Transformations*, eds. H.I. Aronson et al., TMS-AIME, Warrendale, Pa., 1982, pp. 789-806; J.A. Cahn and W.C. Hagel, *Acta Met.*, vol. 11, 1963, pp 561-574.
- [45] RN. Ridley, in *Proceedings of International Conference on Solid – Solid Phase Transformations*, eds. H.I. Aronson et al., TMS-AIME, Warrendale, Pa., 1982, pp. 807-817.
- [46] R.D. Doherty, in "Physical Metallurgy, 4th" ed., R.W. Cahn and P. Haasen, Elsevier Science BV, Amsterdam 1996, chap. 15, pp. 1363-1506.
- [47] W.A. Smith, "Structure and Properties of Engineering Alloys", 2nd ed., McGraw-Hill, 1993, P130.
- [48] Lin li, B.C.D. Cooman, P. Wallant, "Effect of Al and Si on Transformation Induce Plasticity of TRIP steels", *J. Mater. Sci. Technol.* Vol 20, No. 2, 2004.
- [49] R.W. Heckel and H.W. Paxton, "Rates of growth of cementite in hypereutectoid steels", *Trans. TMS-AIME*, 1960, vol. 218, pp. 799–806.
- [50] R.F. Mehl, C.S. Barret, and D.W. Smith, "Studies Upon the Widmanstaetten Structure, IV-The Iron-Carbon Alloys", *Trans. AIME*, vol. 105, 1933, p.215
- [51] R.F. Mehl, and W.C. Hagel, "The Austenite-Pearlite Reaction, Process In Metal Physics", vol. 6, Pergamon Press, Oxford, 1956, p. 1071.
- [52] W.A Johnson and R.F. Mehl, "Trans, Reaction kinetics in processes of nucleation and growth", *AIME*, vol. 135 1939, p. 416.
- [53] J.W. Cahn, W.C. Hagel in "The Decomposition of Austenite by Diffusional Processes", eds. V.F.Zackay and H.I. Aaronson, Interscience, New York, 1962, pp 131-192.
- [54] W. Tofaute and A. Buttinghais, *Arch. Eisenhüttenwe.*, vol. 12, 1938, p. 331.
- [55] *Heat Treating Guide*, ASM International, Materials Park, Ohio, 1995.
- [56] G. Krauss, "Steel-Heat Treatment and Processing Principles", ASM International, Materials Park, Ohio, 1989.
- [57] E. C. Bain and H.W. Paxton, "Alloying Elements in Steel", ASM, Metals Park, Ohio, 1966.

- [58] E. Lemaire, J. Copreaux, and F. Roch, *Scripta Metallurgica*, “Fibrous cementite precipitation: A transition structure between pearlite and upper bainite”, vol. 35, no. 1, 1996, pp. 83–89.
- [59] T. Gladman, I. D. McIvor, and F. B. Pickering, “Some Aspects of the Structure-Property Relationships in High-Carbon Ferrite-Pearlite Steels”, *JISI*, vol. 210, 1976, p. 916.
- [60] B.E. O’Donnelly, R.L. Reuben and T. N. Baker, “Quantitative Assessment Of Strengthening Parameters In Ferrite-Pearlite Steels” From Microstructural Measurements *Metals Technology*, vol. 11, pp. 45-51 (1984)
- [61] *Metals Handbook*, “Metallography and Microstructure, Ninth Edition vol. 9, pp. 178.
- [62] W.S. Owen, The Carbide Phase in Iron-Carbon Silicon Alloys. *Journal of the Iron and Steel Institute*. February 1951, pp. 117.
- [63] E.J. Fasika, “On the Cementite Structure” University of Pittsburgh, 1965.
- [64] Anil Kumar Sinha, “Physical Metallurgy Handbook”, 2003, 1.3.
- [65] J. Kim and O. D. Sherby, “Tensile Elongation Behavior of Fine-Grained Fe-C Alloys at Elevate Temperatures”, *Thermomechanical Processing and Mechanical Properties of Hypereutectoid Steels and Cast Irons* pp. 209-218.
- [66] R.W. Heckel and H.W. Paxton, “The morphology of proeutectoid cementite”, *Trans, ASM* 1961, vol. 53, pp. 539-554.
- [67] M.V. Kral and G. Spanos, Three Dimensional Morphology of Cementite Precipitates, *Scripta Materiala*, vol. 36 No. 8, pp. 875- 882, 1997.
- [68] J.D. Baird, and R.R. Preston Research Center, Relationship Between Processing, Structure and Properties in Low Carbon Steels, *Processing and Properties of Low Carbon Steels*, pp. 1-26.
- [69] W. C. Leslie and G. C. Rauch, “Precipitation of carbides in low-carbon Fe-Al-C alloys”, *Metallurgical and Materials Transaction A*, vol.9, No.3, pp.343-349.
- [70] P.G. Shewmon, “Transformations in Metals”, McGraw-Hill, New York, 1969.
- [71] M.-X Zhang and P.M Kelly Accurate Orientation Relationships Between Ferrite And Cementite In Pearlite, *Scripta Materiala*, vol. 37,1997, pp. 2009-2015.
- [72] A.M. Elwazri, P. Wanjara, and S. Yue, Effect of Prior-Austenite Grain Size and Transformation Temperature on Nodule Size of Microalloyed Hypereutectoid Steels, *Metallurgical And Materials Transactions A*, Vol 36a, Sep, pp 2005—2297.

- [73] J.M. Hyzak and I.M. Bernstein, "The Role of Microstructure on the Strength and Toughness of Fully Pearlitic Steels" *Metall. Trans. A*, 1976, vol 7A pp. 1217-1224.
- [74] T. Gladman, I. McIvor, "Structure-property relations in high-carbon ferrite-pearlite steels *Iron Steel Inst*", 210 (1972) 916- 930.
- [75] M. Gensamer, E.B. Pearsall, W.S.Pellini, and J.R. Low; "Tensile Properties of Steels" *Trans ASM*, 1942, vol. 30, pp. 983.
- [76] T. Takahashi and M. Nagumo, "Flow stress and work-hardening of pearlitic steel" *Trans. Jap. Inst. Metals*, 1970, vol. 11, pp.113.
- [77] G.K. Bouse, I.M. Bernstein and D.H. Stone(1976), Role of Alloying and Microstructure on the Strength and Toughness of Experimental, Rail Steels. Symposium on Rail Steels. ASTM, Denver, Colorado, November 17-18 1976.
- [78] Heshmat A. Aglan (2006), "Fatigue Damage Tolerances of Bainitic and Pearlitic Rail Steels", *International Journal of Damage Mechanics*, Vol 15 Octobre 2006.
- [79] Eric M. Taleff, Chol K. Syn (1995) Pearlite in Ultrahigh Carbon Steels: Heat Treatment and Mechanical Properties, *Metallurgical Materials Transaction A*.
- [80] Karlsson, B. & Linden G., "Plastic deformation of ferrite—pearlite structures in steel" (1975), *Materials Science and Engineering*, Vol. 17, (1975), pp. 209-219.
- [81] M. A. Daeubler, A. W. Thompson and I. M. Bernstein, "Influence of microstructure on fatigue behavior and surface fatigue crack growth of fully pearlitic steels, Volume 21, Number 3, 925-933, 1987.
- [82] A.M. Elwazri, P. Wanjara (2005), "The effect of microstructural characteristics of pearlite on the mechanical properties of hypereutectoid steel", *Material Science & Engineering A* 404 (2005) pp.91-98.
- [83] P. Clayton and D. Dank (1990), "Effect of Interlamellar Spacing on the Wear Resistance of Eutectoid Steels under Rolling/Sliding Conditions", *Wear*, Vol. 135, 1990, pp. 369-389.
- [84] E.L Brown and G. Krauss, unpublished research, Colorado School of Mines, 1982.
- [85] George Langford, "Deformation of Pearlite", *Metallurgical Transaction A*, vol. 8A, 1977, pp. 861
- [86] D.A Porter I.E. Easterling, and G.D.W. Smith; *Acta Metall.*, 1978, vol. 26, pp.1405-1422.

- [87] J.J. Lewandowski and A.W. Thompson, "Microstructural Effect on the Cleavage Fracture Stress on Fully Pearlitic Eutectoid Steel" *Advances in Fracture Research ICF6*, Vol. 2, (S.R. Valluri, D.M.R. Taplin, P. Rama Rao, J.F. Knott, R. Dubey, eds.), Pergamon Press, pp. 1515-1522.
- [88] J. D. Embury, R. M. Fisher, 'The Structure and Properties of Drawn Pearlite' *Acta Metallurgica* 14, 147-159 (1966).
- [89] Steif and S. Iyengar, "Effect of Inclusion Distribution on the Initiation of Defects, Inclusions and Their Influence on Material Behavior", *World Materials Congress 1988*, ASTM International, pp. 133-138.
- [90] A.R. Marder and B.L. Bramfitt, "The effect of morphology on the strength of pearlite on the strength of pearlite", *Metall. Trans. A*, 7A (1976), pp365-372
- [91] W. Heller, "In Rail Steels" , SPT 644, ASTM, Philadelphia, 1979
- [92] G.Gray III, A. Thompson and J. Williams, "Roughness Induced Crack Closure: An Explanation for Microstructurally Sensitive Fatigue Crack Growth", *Metall. Trans. A*, 14A (1983) pp.421-433
- [93] J.G. Sevillano, "On the Yield And Flow Stress of Lamellar Pearlite, *Proc Strength of Metals and Alloys*" Vol 2 (Aachen, Germany 1979) PP. 819-824.
- [94] J.J. Lewandowski and A. W. Thompson, "Microstructural Control of the Cleavage Fracture Stress in Fully Pearlitic Steels" *Metall. Trans A*, 17A (1986), pp. 1769-1786.
- [95] D.J. Alexander and I.M. Bernstein, "The cleavage plane of pearlite", *Metall. Trans. A*, 20A(1987), PP. 2321-2335.
- [96] Eric M. Taleff, J.J. Lewandowski and Bandam Pourlandia, "Microstructure-Property Relationships in Pearlitic Eutectoid and Hypereutectoid Carbon Steels", *JOM*, July 2002 pp. 25-29.
- [97] Y.J. Park and I.M. Bernstein, "Effective Grain Size for Cleavage Fracture in Pearlitic Eutectoid Steel", *Fracture 1977*, vol. 2 (Tarrytown, NY. Pergamon Press, 1977) pp. 33-40.
- [98] Y.J. Park and I.M. Bernstein, "The process of crack initiation and effective grain size for cleavage fracture in pearlitic eutectoid steel", *Metall. Trans. A*, 10A 1979, pp. 1653-1664
- [99] W. Dahl et al., *Stahl U. Eisen*, 1966, 86, 797.

- [100] George F. Carpenter, Roger K. Steele and Michael J. Markase, "Effect of inclusion content on the fatigue performance of rail steels" Rail Steels Symposium Proceeding. pp 49-56, 1992.
- [101] Ev.A. Shu, N. Ya Bychkova, S.M. Trushevsk, "Physical metallurgy aspects of rolling contact fatigue of rail steels", Wear, 258 (2005), pp.1168-1171.
- [102] V. Sagadze, "Reliability growth of cementite steel", Mashinostroenie 1975, 216
- [103] Nobuhisa Tabata, Shozaburo Nakano Yasuhiro Nakagawa, "Development of Thermomechanically Control-Processed High Carbon Chromium Steels for Ball Bearing without Annealing", Kawasaki Steel Giho, 23 (1991)2, 98-104.
- [104] K. Han, G.D.W. Smith and D.V. Edmonds, "Pearlite Phase Transformation in Si and V Steel", Metall. And Materials Transaction A, vol. 26A, 1995 pp 1617.
- [105] Y.E. Smith, C.A. Siebert, "Continuous Cooling Transformation Kinetics of Thermomechanically Worked Low-Carbon Austenite" Metall. Trans 2, (1971) 1711-1725
- [106] R.W.K. Honeycombe, D.J. Walker, "Effects of deformation on the decomposition of austenite: Part I—The ferrite reaction" Metal Science vol 12, 10 (1978) 445-452
- [107] J.J. Jonas, R.A. do Nascimento, "Fundamentals of Dual Phase Steels" (edited by R.A. Kot and B.L. Bramfitt), Metallurgical Society AIME, Warrendale, PA, (1981) 95-112.
- [108] J.J. Jonas, R.A. do Nascimento, I. Weiss, and A.B. Othello, "Effect of Deformation on the $\gamma \rightarrow \alpha$ Transformation in Two High Silicon Dual-Phase Steels", in Fundamentals of Dual Phase Steels, R.A. Kot and B.L. Bramfitt, Ed., TMS-AIME, 1981, pp 95–112.
- [109] E.V. Konopleva, V.M. Khlestov, and H.J. McQueen, "Hot Deformation Effects on Austenite Decomposition in Alloy Steels, Phase Transformations During Thermal/Mechanical Processing of Steel", E.B. Hawbolt and S. Yue, Ed., Met. Soc. CIM, 1995, p 243–258.
- [110] K. Han, T.D. Mottishaw, G.D.W. Smith, "Effects of Vanadium on Microstructure and Hardness of Hypereutectoid Pearlitic steels", Mat Scie, and Eng. A190 (1995) 207-214.
- [111] K.W. Burns and F.B. Pickering, JISI, 1964, vol. 202 pp. 889-906.
- [112] F.B. Pickering, "Iron and Steel", 1965, vol. 38, pp. 110-118.
- [113] A. R. Marder and B. L. Bramfitt; "The effect of morphology on the strength of pearlite" Metall. Trans. 7A (1976) 365-372.
- [114] M. Gensamer, E.B. Pearsall, and G.V. Smith, "The mechanical properties of the isothermal decomposition products of austenite" Trans. ASM, 1940, vol. 28 pp. 380-395
- [115] Y. Yamada, Trans. ISIJ, 1997, vol. 17, pp. 516-522.

- [116] J.H Gross and R.D. Stout; Weld Res. Supp., 1951, vol 30, pp. 481s-485s.
- [117] L.E. Miller and G.C. Smith; JISI , 1970 vol 208, pp. 998-1005.
- [118] A. Fernandez-Vicente et al., Fracture Behavior of Two Ultra high carbon steels” Deformation Proceedings and Properties of Hypereutectoid Steels and cast Irons, ed. E. M. Taleff, C.K. Syn. And Lewandowski, J.J., and Thompson, A.W. (1986), “Microstructural Effects on Ductility in Fully Pearlitic Steels”, Met. Trans. A, 17A, pp. 461-472.
- [119] Lewandowski, J.J., and Thompson, A.W. (1986). "Microstructural Effects on Ductility in Fully Pearlitic Steels", Met. Trans. A, 17A, pp. 461-472.
- [120] Lewandowski, J.J., and Thompson, A.W. (1987). "Modelling Cleavage Fracture in Fully Pearlitic Microstructures", Acta Met., 35, pp. 1453-1462.
- [121] T. Ando and G. Krauss, “The Effect of Phosphorus Content on Grain Boundary Cementite Formation in AISI 52100 Steel” Metall. Trans., vol 12A, July 1981, pp. 1283.
- [122] T.D.Mottishaw, G.D.W. Smith, “ Microalloyed Pearlitic Steel for the Wire Industry Mechanisms of Alloy Element Redistribution and Strengthening Processes in Chromium-Vanadium Eutectoid Steels” Department of Metallurgy and Science of Materials, Oxford University.